10-30-2020

Mechanism Determination of the Effects of Pancratistatin on Model Mitochondrial Membranes

Brett William Rickeard

University of Windsor

Recommended Citation

Rickeard, Brett William, "Mechanism Determination of the Effects of Pancratistatin on Model Mitochondrial Membranes" (2020). *Electronic Theses and Dissertations*. 8475.
https://scholar.uwindsor.ca/etd/8475

Mechanism Determination of the Effects of Pancratistatin on Model Mitochondrial Membranes

By

Brett W. Rickeard

A Thesis
Submitted to the Faculty of Graduate Studies
through the Department of Chemistry and Biochemistry
in Partial Fulfillment of the Requirements for
the Degree of Masters of Science
at the University of Windsor

Windsor, Ontario, Canada

2020

Mechanism Determination of the Effects of Pancratistatin on Model Mitochondrial Membranes

by

Brett W. Rickeard

APPROVED BY:

J. Dason
Department of Biomedical Sciences

S. Pandey
Department of Chemistry & Biochemistry

D. Marquardt, Advisor
Department of Chemistry & Biochemistry

August 25, 2020

Declaration of Originality

I hereby certify that I am the sole author of this thesis and that no part of this thesis has been published or submitted for publication.

I certify that, to the best of my knowledge, my thesis does not infringe upon anyone's copyright nor violate any proprietary rights and that any ideas, techniques, quotations, or any other material from the work of other people included in my thesis, published or otherwise, are fully acknowledged in accordance with the standard referencing practices. Furthermore, to the extent that I have included copyrighted material that surpasses the bounds of fair dealing within the meaning of the Canada Copyright Act, I certify that I have obtained a written permission from the copyright owner(s) to include such material(s) in my thesis and have included copies of such copyright clearances to my appendix.

I declare that this is a true copy of my thesis, including any final revisions, as approved by my thesis committee and the Graduate Studies office, and that this thesis has not been submitted for a higher degree to any other University or Institution.

Abstract

Apoptosis is programmed cell death that is essential for physiological development and tissue homeostasis. From a biochemical standpoint, this process can be exploited to target and eliminate specific cell types, such as cancer cells. Pancratistatin (PST) is an antiviral alkaloid metabolite that has demonstrated directed apoptotic action on various human cancer cell lines while having minimal/no toxic effect on normal cells. However, PST's mechanism of action remains uncertain. To better understand how PST induces its anti-cancer action various biophysical techniques were employed. Neutron spin-echo (NSE) spectroscopy was used to examine how PST impacted the bending fluctuations of large unilamellar vesicles (LUVs) bearing a lipid composition meant to mimic the inner mitochondrial membranes (IMM). The IMM mimic was composed of three lipids: 1-palmitoyl-2-oleoyl-sn-glycero-3-phosphocholine (POPC), 1-palmitoyl-2-oleoyl-sn-glycero-3-phosphoethanolamine (POPE), and tetraoleoyl cardiolipin (TOCL). Small-angle neutron and X-ray scattering (SANS and SAXS) were utilized to determine how PST influences membranes structure. Molecular dynamics (MD) simulations were used to compliment the data gathered from the scattering experiments, while also examining lipid chain order, PST localization and the PST-lipid relationships. The results show that PST has a condensing effect the IMM mimic. This thesis elaborates on the possible implications of this finding with regard to the nature of PST's interaction with the IMM mimic and proposes a hypothesis for the anti-cancer mechanism of PST.

Acknowledgements

First and foremost, I'd like to thank my research supervisor Dr. Drew Marquardt. Under his guidance I was able to learn in a positive and supportive environment. Dr. Marquardt provided me with unique opportunities and experiences that I will never forget. I'm grateful to have learned from someone as helpful, passionate and dedicated as Dr. Marquardt.

Thank you to my committee members, Dr. Siyaram Pandey and Dr. Jeffrey Dason, for the feedback and advice during the course of my graduate research.

I must also thank Dr. Markus Miettinen for sharing his knowledge of molecular dynamics simulations and for helping me adjust to life in Berlin. I'd also like to thank Dr. Milka Doktorova for her help with computational calculations.

I would like to thank the current and former members of the LABR group for all their help and support. Thank you to Mitchell DiPasquale and Michael H. L. Nguyen, your help was greatly appreciated and I will never forget our adventures in Australia, Indonesia, Vietnam, Singapore, and Thailand.

Thank you to all my friends in the Department of Chemistry and Biochemistry. You're comradeship and encouragement made graduate school more enjoyable. To Justin Roberto, thank you for all the enjoyable late-night conversations.

I'd like to extend my thanks to all my friends who have helped over the duration of my graduate studies. To Nik Veigli and Jordan Hooker, thank you for all the rounds of golf and wing nights, your friendship and support is greatly appreciated. To Maxemilian Nascimento, thank you for your advice and friendship.

Special thank you to my girlfriend Vanessa Longo for her incredible support and for always believing in me. You helped guide me through many stressful situations and never hesitated to help me.

Finally, I'd like to thank my parents and Brady for all their love and support. Your confidence in me is reassuring and greatly appreciated.

Table of Contents

List of Figures

List of Tables

List of Abbreviations

ATP Adenosine Triphosphate

CHARMM Chemistry at Harvard Macromolecular Mechanics

CL Cardiolipin

DLS Dynamic Light Scattering

DMSO Dimethyl Sulfoxide

DMSO-d6 Dimethyl Sulfoxide-D6

ED Electron Density

ETC Electron Transport Chain

GUV Giant Unilamellar Vesicle

IMM Inner Mitochondrial Membrane

LUV Large Unilamellar Vesicle

MD Molecular Dynamics

MLV Multilamellar Vesicle

NCNR National Institute of Standards and Technology Center for Neutron Research

NSE Neutron Spin-Echo

NSLD Neutron Scattering Length Density

PC phosphatidylcholine

PE phosphatidylethanolamine

POPC 1-Palmitoyl-2-oleoyl-sn-glycero-3-phosphocholine

POPE 1-Palmitoyl-2-oleoyl-sn-glycero-3-phosphoethanolamine

PST Pancratistatin

RDF Radial Distribution Function

ROS Reactive Oxygen Species

SANS Small-Angle Neutron Scattering

SAS Small-Angle Scattering

SAXS Small-Angle X-ray Scattering

SDP Scattering Density Profile

SL Scattering Length

SUV Small Unilamellar Vesicle

TOCL Tetraoleoyl Cardiolipin

VMD Visual Molecular Dynamics

Chapter 1

Introduction

1.1 Model Membranes

1.1.1 Purpose, Utility and Limitations

Biological membranes are extremely complex components of cells. They are composed of two lipid leaflets that house a variety of a macromolecules, where the composition of the membrane and its associated macromolecules is based on cell type. The main function of a biomembrane is to provide a selectively permeable barrier, defining cells or organelles within cells. Many biochemical processes depend on the structural diversity and physical properties of biomembranes, such as: cell volume maintenance [1, 2], cellular signalling [3–5], energy production [6–8], toxin defence [9], macromolecule transportation [10, 11], pH regulation [12] and protein function [13–16].

The relevance of biomembranes has motivated the development of simpler model systems that are tailored to represent the size, shape and composition of the desired biological membrane. Model membranes enable experimenters to pinpoint the role of certain macromolecules in membrane associated interactions by isolating different aspects of membrane functionality, providing an insight into the bigger picture. Extracting similar information from a biomembrane would be problematic due to their crowded nature. Model membranes have been used to study the structural properties of lipids [17–19], membrane heterogeneity [20–23] and interactions between lipids and drugs or other molecules [24–28].

Model membranes have proven utility, but it is important to acknowledge their limitations. They lack the overall intricacy of a biomembrane, as they are typically composed of only 1-3 lipids and another biological or synthetic molecule [29]. Consequently, the reduced structure of model membrane can be seen as restriction regarding its biological mimicry [30].

1.1.2 Classification and Nomenclature

Model membranes can be constructed in using a variety of methods, however for the purposes of this thesis free-floating phospholipid vesicles will be the focus. Free floating vesicles are hollow spheres composed of a lipid bilayer or multiple bilayers in aqueous solution with a buffer filled lumen. Vesicles with a single bilayer are referred to as unilamellar vesicles, while vesicles with multiple bilayers is a multilamellar vesicles (MLV)s, as shown in Figure 1.1.

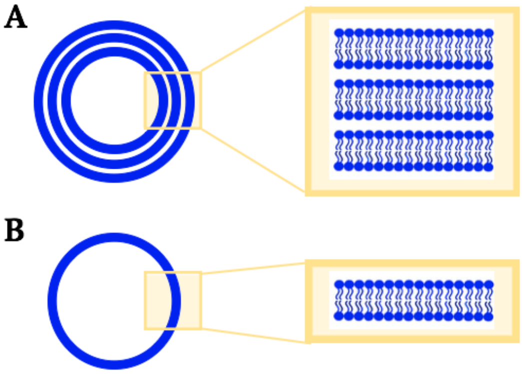

Figure 1.1: The morphological difference between MLVs (A) and unilamellar vesicles (B).

In terms of size, vesicles are classified based on their diameter in nanometers. MLVs tend to be quite large due to their multiple layers, this results in a diameter of 500 nm or greater [31]. Unilamellar vesicles can fall within three main size groups: small unilamellar vesicles (SUVs), large unilamellar vesicles (LUVs) and giant unilamellar vesicles (GUVs). The difference between these vesicle size classes can be seen in Table 1.1 [32].

Vesicle Type	Diameter Range (nm)
SUV	20 - 50
LUV	50 - 500
GUV	$\geq$ 500

Table 1.1: Table outlining the diameters of SUVs, LUVs and GUVs.

Based on size alone GUVs are the most accurate resemblance of eukaryotic cells, which have a diameters of 10,000-30,000 nm [33]. However, GUVs are more susceptible to shrinking or even bursting when interacting with an external molecule [34]. LUVs are small relative to biological cells, but they are quite stable and lack the influence of membrane curvature seen in SUVs [18]. Hence, LUVs deliver a size frame that is a stable and suitable model membrane.

1.2 Mitochondria

The mitochondria is an organelle found in most eukaryotic organisms and is responsible for energy generation and metabolism regulation. They are semi autonomous and have a unique double membrane bound structure. For the purpose of this thesis the inner mitochondrial membrane (IMM) will be the focus considering the drug of interest targets the IMM [35–37].

1.2.1 The Inner Mitochondrial Membrane

The IMM also creates a boundary, isolating the more viscous mitochondrial matrix from the more cytosolic intermembrane space. The IMM also houses the electron transport chain (ETC) which produces the majority of the cell's chemical energy, adenosine triphostphate (ATP). The IMM has a extensive network of folds known as cristae. The cristae greatly increase the surface area of the IMM such that more working space is available for ATP production [38]. A wide variety of lipids form the IMM in eukaryotes, with phosphatidylcholine (PC) being the most abundant, followed by phosphatidylethanolamine (PE) and cardiolipin [39–42]. Cardiolipin's distinctive features and functions will be discussed further in section 1.2.2.

Reactive oxygen species (ROS) are produced by the ETC of the IMM. Electron leakage in the ETC induces the partial reduction of oxygen species to form ROS like superoxide and hydrogen peroxide [43, 44]. ROS are important signalling molecules involved in the regulation of inflammation during stress [45]. Conversely, high levels of ROS can be harmful to the cell as they can cause damage to genetic material [46] and trigger apoptosis and autophagy pathways [45].

Permeability is a key feature of the IMM. Water, carbon dioxide and oxygen can easily cross the IMM, while small ions like protons require specialized ion transporters or channels to cross the barrier [47, 48]. This selective permeability leads to a difference in membrane potential, an essential driving force for ATP synthesis. However, if the IMM potential is disrupted it can lead to a decrease in mitochondria performance, or even cell death via the triggering of apoptotic proteins by cytochrome c release from the IMM [49–52].

1.2.2 Cardiolipin

Cardiolipin (CL) is a class of phospholipids found almost exclusively in the IMM of eukaryotes [53]. Many pathological issues can arise from CL shortage or degradation, including Barth syndrome, neurodegenerative diseases, heart failure and Tangier disease [54–56]. CL is a structurally irregular lipid (see Figure 1.2 in that is has two linked phosphate headgroups, both of which are connected to two hydrocarbon chains via a glycerol backbone [57].

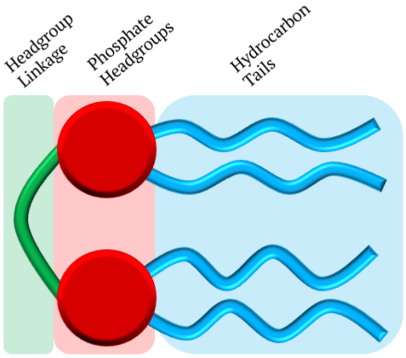

Figure 1.2: A cartoon representation of the basic structure of CL.

Although the behaviour of CL has been understudied, some deductions have been made. CL has the capability to carry two negative charges on its phosphate moieties depending on local pH [58]. These negative charges can bind to cationic species on proteins or other molecules. Recent literature has shown that CL's negative charges play a key role in the stabilization of key lysine residues on ATP synthase, permitting consistent functionality [7]. Similarily, CL has been shown to influence the active site of complex I, making it more accessible to the substrate [16]. CL also aids the complexes of the ETC in an indirect manner. The negative charges permit CL to act as a proton reservoir around the ETC complexes, ensuring that minimal pH charge occurs during proton pump operation [59]. Furthermore, CL is involved in apoptosis, as CL anchors cytochrome c to the IMM and upon disruption of this electrostatic interaction cytochrome c can be released, bringing about an apoptotic cascade [60, 61].

From a biophysical standpoint, CL has a compact headgroup that limits the movement of its phosphate groups while having a large hydrophobic character due to its four hydrocarbon tails. The stark contrast between the small polar headgroup and hydrophobic hydrocarbons gives CL a high degree of negative curvature. As a result CL tends to form inverted non-lamellar lipid phases [62] and can be found in areas with high membrane curvature, such as the cristae [63]. CL's localization at areas of high curvature have lead to finding regarding CL platforms or rafts [64, 65]. These CL rich regions are associated with improving protein functionality by providing a practical platform [3, 20, 63]. CL has a low propensity for hydrogen bonding, as only the hydroxyl group of the glycerol in the headgroup is capable of hydrogen bonding. In combination with the limited mobility of the headgroup, the limited hydrogen bonding ability of CL leads to very little intermolecular hydrogen bonding between CL headgroups [66]. This lack of internal interaction is dissimilar to that most lipids. Thus CL has a lack a self induced shielding, making its negative phosphate groups more accessible to water, ions, drugs and membrane bound proteins [66, 67].

1.2.3 Cancer and the Mitochondria

In healthy people cells grow and divide at a normal rate to satisfy the requirements of the body. Cells will be replaced as they grow old or suffer an injury, resulting in impaired functionality. When cancer develops the process stated above changes in a negative manner. Cancer is caused by multiple changes in gene expression, leading to the dysregulation of standard cell programming for cell proliferation and differentiation [68]. This causes abnormal cell growth that can invade surrounding tissue and spread to other regions of the body. These elements of cancer impede tissue and organ functionality, leading to death if left untreated. Cancer development is attributed to numerous factors including genetic susceptibility, lifestyle choices and interactions with carcinogenic substances [69].

Cancer is one of the most common and deadly diseases in the world today, despite the meticulous efforts towards cancer research. The World Health Organization reports that cancer is responsible for roughly 1 in 6 deaths and is the second leading cause of mortality globally [70]. In Canada cancer is a leading cause of death, in 2016 it was responsible for 30% of all Canadian deaths [71]. Certain types of cancers are more prevalent than others, as the Canadian Cancer Society states that lung, breast, colorectal and prostate cancer account for 50% of newly diagnosed cancer cases [71].

Several differences exist between cancer mitochondria and healthy mitochondria. Firstly, transformed cells have a higher rate a proliferation and more metabolic demands as a consequence. This stress causes irregular lipid remodelling in the mitochondrial membranes, leading to complications with mitochondrial fusion and fission, as well as impairing the ETC [72]. Secondly, cancer cells rely heavily on glycolysis in the presence of oxygen, accordingly termed aerobic glycolysis, for the generation of ATP [73, 74]. The shift to aerobic glycolysis favours cancer cells in that proliferation and energy generation can occur under varying oxygen conditions [75]. The dependence on glycolysis yields a more acidic cytosol due to large amounts of pyruvate and lactate, promoting membrane hyper polarization while simultaneously disrupting the ETC and increasing ROS abundance [76, 77]. In contrast, many studies have shown that the mitochondria remain functional in numerous cancers [78–86]. Cancer cells may indeed depend on both oxidative phosphorylation and aerobic respiration to cater to the demanding energetic needs of cancer cells [87–89]. Some cancer cell lean laboriously on oxidative phosphorylation to produce ATP due to preference or metabolic necessity [90–92]. Moreover, cancer cells exhibit higher concentrations of Bcl-2 proteins. These proteins help protect cancer mitochondria by making them less vulnerable to mitochondria membrane permeabilization [93]. These unique features of cancer cell mitochondria have presented attributes that can be exploited for the purpose of selectively targeting cancer cells. Compounds that seek to target cancer mitochondria are termed mitocans and they aim to disrupt the ETC, inhibit Bcl-2 proteins, increase mitochondrial membrane permeability, increase ROS concentration and target the compromised mitochondrial assembly [94, 95].

1.3 Pancratistatin

Plants of the Amaryllidaceae family have been used to treat numerous diseases throughout history [96]. The *Hymenocallis littoralis*, better known as the spider lily, is a member the Amaryllidaceae plant family. Fueled by possible health implications, the biochemical compounds found in *Hymenocallis littoralis* were extracted, leading to the discovery of pancratistatin (PST) by Pettit et al. in 1984 [97, 98]. The chemical structure of PST can be seen in 1.3.

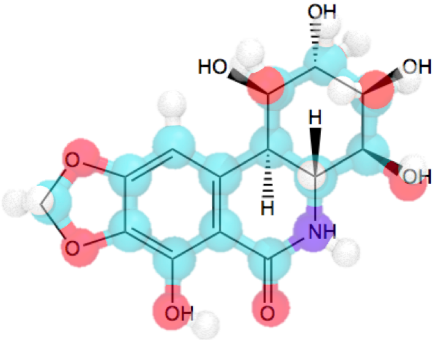

FIGURE 1.3: The chemical structure of PST.

1.3.1 Anti-Cancer Activity

Current cancer research has strived to find compounds, such as mitocans, that can upset biochemical processes in cancer cells while having little to no toxic impact on adjacent healthy cells. PST is a mitocan that has demonstrates this attractive ability, as previous studies have shown its selectivity between cancerous and healthy cells [35–37, 99–102]. PST's anti-cancer capabilities are evident in a number of human cancer types including leukemia [101], colorectal cancer [102], prostate cancer [37], breast cancer [36], human neuroblastoma [35], lymphoma [99] and melanoma [100]. Cancer mitochondria are the target of PST; it causes an early increase ROS concentration, loss of mitochondrial membrane potential, decrease in ATP output, and initiation of apoptotic agents [35–37, 99–102]. Although PST has proven ability as a mitocan, the mechanism at which this ability stems from remains elusive [99].

1.4 Objectives

The present study looks to advance and expand on the previous research of PST and its operational mechanism with respect to the IMM. Little to no investigation into the impact of PST on membrane biophysics has been undertaken. The objectives of this thesis include:

1. Study the influence of PST on model IMM dynamics.

2. Examine how PST changes structural parameters of the model IMM.

3. Deduce if a relationship exists between the different lipid species in the model IMM and PST and the possible implications of this connection.

Chapter 2

Experimental Techniques

2.1 Small-Angle Scattering

Small-angle scattering (SAS) is a scattering technique used to extract structural properties of a sample based on how it deflects incoming radiation. The wavelength of the incident radiation (typically 1-12 Å depending on radiation type) is much smaller than the sample itself (>50 nm for most lipid vesicles), resulting in a small deflection angle and giving the technique its name [103]. SAS is an elastic scattering technique, meaning their is no energy transfer during interactions between the sample and the radiation. Thus, information regarding the structure, size, shape, and orientation of bilayers and lipids within bilayers can be extracted at a high resolution without the influence of energy fluctuations [103–106]. SAS provides some distinct advantages with regards to analyzing biological samples. It provides structural information about fractionally or completely disordered systems, it can study supramolecular structures in physiologically relevant environments and it is non-destructive [103]. Other techniques typically require probes to exact similar information, perturbing the membrane in the process [107].

SAS techniques operate by shining monochromatic radiation onto a sample, which consequently scatters at an angle onto a two-dimensional detector. The one-dimensional radial average of the scattered radiation is then taken, which determines the amount of particles present at at given distance away from a reference particle. The radial average can be manipulated to generate a form factor; a numerical representation of the size, shape and arrangement of the particles in a sample. A visual representation of how the radial average translates to the form factor can be seen in Figure 2.1 by way of the colour gradient shown on the detector and the corresponding form factor.

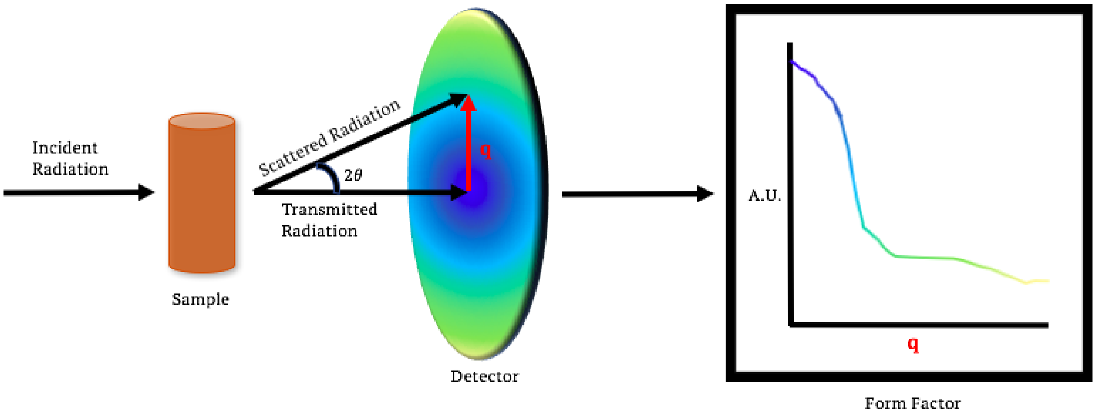

FIGURE 2.1: Schematic of how SAS works, highlighting how the radial average translates to a form factor.

The scattering vector, q, can be used to interpret the form factor. The q values are determined by scattering angle (2θ) as shown by the following equation:

$$q = \frac{4\pi sin\theta}{\lambda} \tag{2.1.1}$$

In equation 2.1.1, 2θ represents the angle between the incident radiation and the scattered radiation, while λ represents the wavelength of the radiation. The scattering vector is the resolution or yardstick by which the sample is being viewed [103]. Therefore, as the magnitude of q changes, different sized structural features can be analyzed. The value of q is inversely related to size in real space. In vesicles, low q is used to interpret interactions between vesicles or vesicles and a foreign substance, intermediate q looks at membrane features such as bilayer thickness and high q examines lipid properties and interactions like area per lipid [108]. Figure 2.2 shows how various q values on a scattering curve relate to different areas in a vesicle containing sample.

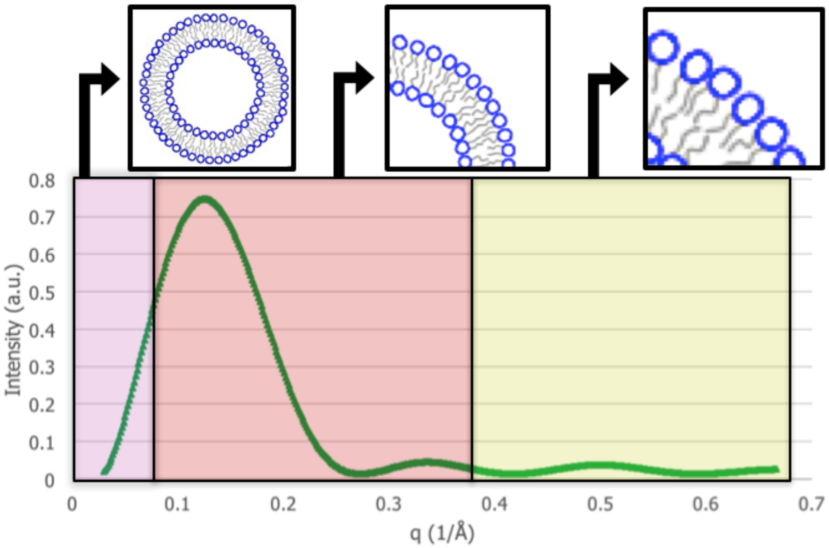

FIGURE 2.2: An illustration of how the scattering vector translates to different sized vesicle features.

2.1.1 Neutron Versus X-rays

The two major types of SAS are small-angle neutron (SANS) and x-ray (SAXS) scattering. The major difference between these two techniques is that SANS uses neutrons as incident radiation while SAXS uses x-rays. This distinction is what makes the two techniques unique but complimentary. For SANS the incoming neutrons scatter off the nuclei of the sample, whereas the electron cloud is the scattering medium for SAXS. For SAXS their is a defined trend regarding how different elements interact with x-rays, as the more electron density (ED) an element possesses the stronger it will scatter x-rays. The strength at which an element scatters radiation can be quantified by the scattering length (SL). This quality can be thought of as the refractive index of the element with respect to scattering. The interaction between incident neutrons and matter is very complex, resulting in no trend between neutron SL and the periodic table [105]. Even isotopes of the same element exude large differences in neutron SL. Nuclei scatter incident neutrons in two ways, coherently and incoherently. An isotope that scatters coherently scatters in a predictable manner, yielding structural information about adjacent nuclei and itself. Contrastingly, isotopes that scatter in an incoherent manner are unpredictable and provide little to no useful information [105]. This is an issue for biological samples as H^1 nuclei scatter incoherently and compromise some of the structural information that could be extracted from the sample. To combat this deuterium, a strong coherent scatterer, is used to limit the amount of protons in the sample and improve the quality of SANS experiments. The numerical trend difference between ED and neutron scattering length density (NSLD) is presented in Table 2.1 [103].

Atom	H^1	H^2	C	N	O
Atomic Mass	1	2	12	14	16
Number of Electrons	1	1	6	7	8
NSLD, 10^{-12}cm	-0.374	0.667	0.665	0.940	0.580

Table 2.1: Table showing the difference in trends of electron ED and neutron SL for nuclei commonly found in biology.

SANS and SAXS provide information regarding different structural elements of a lipid bilayer. Considering x-rays interact with the electron density of a sample, SAXS can be used to better locate electron rich portions of a bilayer. For membranes composed of phospholipids this is particularly important, as phosphorus is electron rich and its location relative to the membrane can be pinpointed. This enables parameters such as distance between electron density maxima to be calculated [17, 104, 109]. On the other hand, SANS can help highlight areas of the membrane with a high degree of coherent scattering. Areas with high deuterium, carbon and/or nitrogen content scatter in a coherent manner, thus SANS is useful locating features like the glycerol backbone and choline headgroups [17, 110–112].

To gain complete picture regarding the framework of a lipid membrane a scattering density profile (SDP) should be constructed. Fundamentally a SDP is the real space distribution of EDs or neutron SLs of a system. A SDP displays how the EDs and neutron SLs fluctuate with respect to position about the bilayer. An example of this is shown in Figure 2.3, where the EDs and neutron SLs are plotted with respect to z, the distance from bilayer center. The SDP plot allows certain portions of the lipid to be identified. For example, on the ED side of the plot the head group region with the electron rich phosphate group can be identified by the increase in ED around 1.5-2 nm from bilayer center.

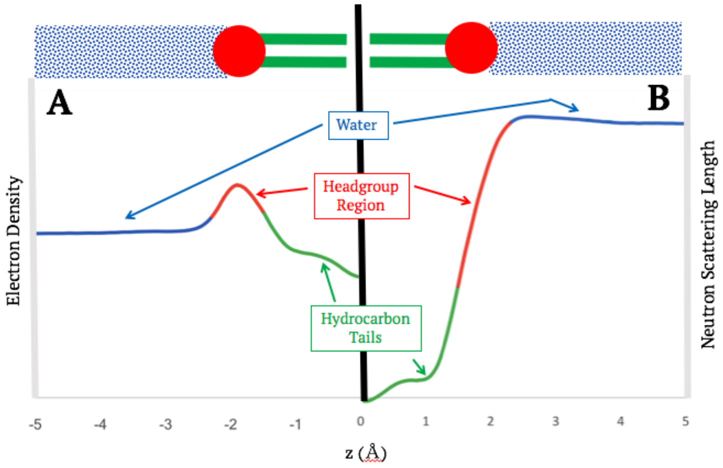

Figure 2.3: A graphical comparison betweenn ED (A) and neutron SL (B) and how they correlate to different areas of a lipid bilayer.

SANS and SAXS have been used in the past to better understand drug-membrane interactions. These techniques can examine the impact a drug has on various biophysical membrane parameters, such as membrane permeability and bilayer thickness, which have cell health implications [26, 27, 109, 113]. Based on the established ability for SANS and SAXS to effectively examine drug-membrane interactions, a similar experimental strategy was employed during this research to better comprehend PST and its relationship with the IMM.

2.2 Neutron Spin-Echo

Neutron spin-echo (NSE) is a neutron scattering technique that examines membrane dynamics. It is a quasielastic technique that measures time differences that occur due to neutron-sample interactions and through analysis this time difference can be translated to an energetic property. In order to find variance in time the spin and magnetic moment of the neutrons is utilized [114]. The NSE technique uses polarized neutrons, meaning all the neutrons that enter the instrument are filtered so only neutrons of the single, desired neutron spin orientation enter the instrument. The polarized neutrons then move through the magnetic fields withing the NSE and eventually the detector. The key to NSE's functionality is Larmor precession, which occurs polarized neutrons move through a magnetic field. Larmor precession occurs when neutron spin is perpendicular to a magnetic field, causing the spinning neutron to rotate around the magnetic field as shown in Figure 2.4 [114]. The use of Larmor precession is the basis of NSE as it provides each neutron with an internal clock, allowing changes in initial and final neutron velocity to be monitored and compared [114]. The change in neutron speed as it progresses through the NSE instrument can eventually be related to an energetic value related to the sample.

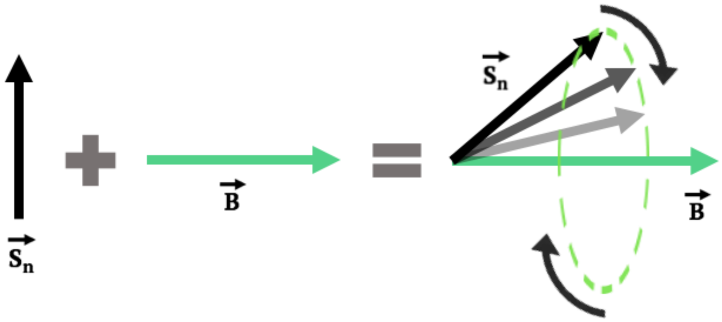

FIGURE 2.4: An image showing how Larmor precession occurs to a neutron spin $\overrightarrow{S}_{\mathrm{n}}$ in magnetic field $\overrightarrow{B}$.

The basic layout of a NSE instrument can be found in Figure 2.5. The rudimentary concept is as follows [114]: The incident neutron velocity is selected for by the neutron velocity selector (NVS). A single neutron spin state is selected via the neutron polarizer (P). The 90° flipper (F) turns the polarized neutrons so their spins are perpendicular to the magnetic field (in Figure 2.5 the magnetic field is running horizontally from left to right). The neutrons then enter the first precession coil (PC-1), undertaking in Larmor precession. After exiting the coil the neutrons collide with the sample (S), altering their speed and spin direction. Following sample interaction, the neutrons are inverted by a 180° flipper (F-2) and move through the second precession coil (PC-2), once again practicing Larmor precession. The action of the neutrons moving though the second precession coil can be though of as the neutrons unwinding their original Larmor precession in the first precession coil, bringing the neutron's spin back towards its original orientation. The neutrons pass through the second 90° flipper (F) to stop their precession. Finally they strike the detector (D) at a a slightly different neutron spin angle then they entered the instrument at. This angle change is directly related to the velocity change that occurs during the neutron's interaction with the sample and results in a decrease in measured intensity at the detector [114]. No angle or velocity change would be seen in the case of elastic scattering. It is also important to note that the NSE instrument collects information over a time period rather than at a single moment. These different time durations are known as Fourier times.

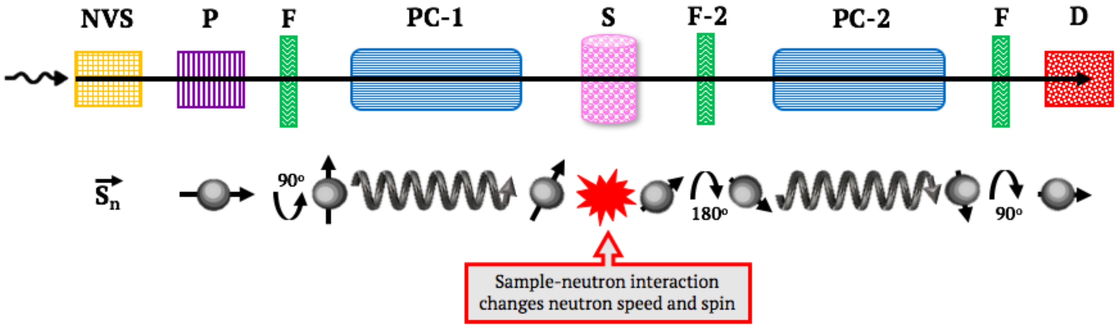

Figure 2.5: A schematic of a NSE instrument that consists of a neutron velocity selector (NVS), a neutron polarizer (P) two 90° flippers (F), magnetic precession fields (PC-1 and PC-2) found before and following the sample (S), a 180° flipper (F-2) and a neutron detector (D). Also shows how neutron spin direction $\overrightarrow{S}_{\mathrm{n}}$ fluctuates with respect to instrument position for a quasielastic scattering case.

NSE can be used to effectively study membrane dynamics. An example of dynamic membrane process that can be measured using NSE is cumulative bending and thickness fluctuations (Figure 2.6), which bring about small changes to membrane shape [114].

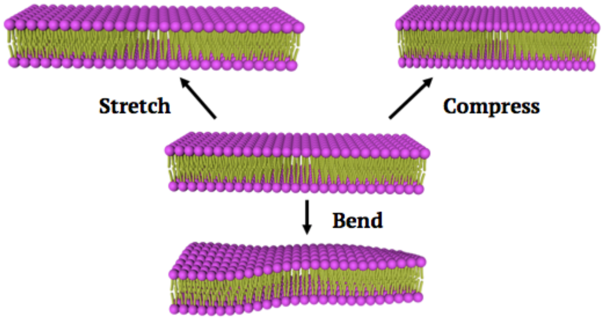

Figure 2.6: An image displaying some common undulations that occur in membranes.

These changes in membrane shape have profound biological consequences on the cell and its function. Membrane shape fluctuations play a role in protein insertion, structure maintenance and performance [13–15, 115], control of IMM functionality [116], vesicle transport and budding [117, 118] and cell motility [119, 120]. Cancer cells have been shown to have softer membranes then their healthy counterparts, which may have an impact on cancer cell movement [121, 122]. In addition to biological events, membrane dynamics has an important in understanding how drug-membrane interactions impact these biological events. NSE has been previously used to study such interactions, finding that changes in membrane rigidity occur due to the interaction and can be linked to certain physiological proceedings [24, 123, 124]. Thus, NSE is a fitting technique to study how PST influences the membrane dynamics of a model IMM.

2.3 Molecular Dynamics

Molecular dynamics (MD) is a computer simulation method used to study how both atoms and molecules move and interact with one another. These simulations are run at a defined temperature over a limited period of time, allowing the system to evolve over that time span. In MD the movement of atoms and the nature of their interactions is determined by solving Newton's equations of motion. To solve Newton's equations the energetic qualities of atoms within a system must be provided by a force field. A force field is a mathematical description of the behaviour of atoms or molecules, quantifying energies associated with intramolecular and intermolecular forces. An example of a force field are the Chemistry at Harvard Macromolecular Mechanics (CHARMM) force fields that are aimed at biomolecular simulations [125, 126] and are the force fields used in the MD work for this thesis. The CHARMM force fields are an example of all-atom force fields, meaning explicit parameters are provided for every atom in a system. Using this type of force field in MD can capture a high level of physical and chemical detail, but have a large computational cost.

MD has been used in many aspects of biomembrane research. This is due to accessibility and efficiency, as many different membrane compositions can be created with relative ease and a great deal of valuable information can be acquired [127–131]. MD has been used to research the structural properties of membranes [132–136], membrane dynamics [137–139], lipid domains [140], membrane-protein interactions [7, 16, 141], ion-membrane interactions [142] and drug-membrane interactions [143]. Furthermore, MD studies have been coupled with SANS,SAXS and NSE experiments to achieve a more comprehensive understanding of the system of interest [17, 19, 111, 144–146]. Importantly, this concept has been previously applied to better grasp the mechanism of bilayer-drug interactions [27, 113]. With regards to this thesis, scattering techniques in tandem with MD simulations is a powerful combination, providing useful and complimentary details regarding how PST interacts with the model IMM.

Chapter 3

Materials and Methods

3.1 Materials

3.2 Reagents

Chloroform	Sigma-Aldrich, Oakville, ON
Deuterium Oxide	Cambridge Isotope Laboratories, Inc., Montreal, QC
Dimethyl Sulfoxide-D6 (DMSO-d6)	Cambridge Isotope Laboratories, Inc., Montreal, QC
Dimethyl Sulfoxide (DMSO)	Sigma-Aldrich, Oakville, ON
1-Palmitoyl-2-oleoyl-sn-glycero-3-phosphocholine (POPC)	Avanti Polar Lipids, Inc., Alabaster, AL, USA
1-Palmitoyl-2-oleoyl-sn-glycero-3-phosphoethanolamine (POPE)	Avanti Polar Lipids, Inc., Alabaster, AL, USA
Pancratistatin (PST)	Toronto Research Chemicals, North York, ON
Tetraoleoyl cardiolipin (TOCL)	Avanti Polar Lipids, Inc., Alabaster, AL, USA

3.3 Methods

3.3.1 Experimental

Vesicle Preparation and Characterization

Lipid films were created by transferring the desired volume of lipid in chloroform stock solution to separate glass scintillation vials using a glass syringe (Hamilton USA, Reno, NV). Chloroform was removed from the lipid solutions under gentle house vacuum and the resulting lipid films were dried for a minimum of 12 hours under vacuum at 30 °C. The vesicle films were then hydrated to the desired concentration with either D_2O or H_2O depending on the experiment. The MLVs were then subjected to 5 freeze/thaw cycles at -80 °C and 50 °C, with vortexing occurring after each thawing step. The vesicles samples were modified into LUVs by passing the samples through a hand-held mini-extruder equipped with 100 nm polycarbonate filters (Avanti Polar Lipids, Alabaster, AL) 31 times. LUV size distribution was confirmed via dynamic light scattering (DLS) on a Malvern ZetaSizer Nano ZS (Malvern Panalytical, Ltd., Malvern, UK). DLS is a technique that measures Brownian motion and relates this to the size of a particle in solution. The diameters of the vesicles used in various experiments can be found in Appendix A.

Three lipid species were used to create controls and the IMM mimic: tetraoleoyl cardiolipin (TOCL), 1-Palmitoyl-2-oleoyl-sn-glycero-3-phosphocholine (POPC), and 1-palmitoyl-2-oleoyl-sn-glycero-3-phosphoethanolamine (POPE). Their chemical structures can be seen below in Figure 3.1.

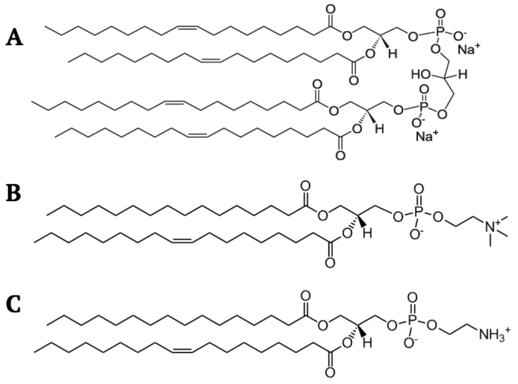

Figure 3.1: The chemical structure of TOCL (A), POPC (B), and POPE (C).

These three lipid species were selected based on their relative abundance in the IMM of eukaryotes. Lipids with a phosphocholine headgroup are the most common, followed by lipids with a phosphoethanolamine headgroup and then cardiolipin species [42]. Hydrocarbon chains in the IMM are longer in nature and possess some degree of unsaturation. Hence, POPC and POPE were selected as their hydrocarbon tails have both these qualities. For cardiolipin, TOCL was selected as unsaturated 18-carbon chains account for the vast majority of cardiolipin tails in the IMM [147, 148].

The lipids mentioned above were used to construct various vesicle compositions. The focal composition was meant to mimic the IMM, while others served as controls to observe if TOCL behaved differently when accompanied by only POPC or POPE. Table 3.1 shows the mole percent of each lipid in each vesicle compositions.

Composition Name	TOCL	POPC	POPE	Analysis Methods
IMM Mimic	25	50	25	SANS, SAXS, NSE, and MD
TOCL/POPC Control	50	50	0	SANS, SAXS, NSE, and MD
TOCL/POPE Control	50	0	50	SANS, SAXS, NSE, and MD
TOCL Control	100	0	0	SANS, SAXS, and MD

TABLE 3.1: Table showing the relative mole percent of TOCL, POPC, and POPE in the dissimilar vesicle compositions. Also shows the analysis techniques used on each composition.

PST Preparation and Addition

PST has very limited solubility in water [149]. Thus, PST was dissolved using dimethyl sulfoxide-d6 (DMSO-d6) for all neutron experiments or dimethyl sulfoxide (DMSO) for all other experiments. PST was massed out using a Sartorius Entris 64-1S Analytical Balance (Goettingen, Germany). A concentration of 9.5 mg/mL was achieved by adding DMSO or DMSO-d6 to the PST powder. This concentration was used so that upon addition to the vesicle-water solution the mole percent of DMSO or DMSO-d6 was less than 1 mole percent, greatly lowing the influence of DMSO or DMSO-d6 on the structural properties of the lipid bilayer [150]. In order to fully dissolve the PST, the mixture was sonicated at 50 °C for 1 hour using a Fisherbrand CPXH 8800 Ultrasonic Water Bath (Fisher Scientific Ltd., Ottawa, ON). To ensure no PST aggregates formed, the aggregation index was extracted using DLS. No aggregates were observed in the DMSO or DMSO-d6 solutions.

PST was directly added to extruded vesicles at a temperature of 37 °C at least 12 hours prior to any experimental analysis. This measure was taken so the time period in which data was collected aligned with the active time period of PST based on biological assays [37, 99]. PST was added at three mole percents: 1%, 1.5% (concentration used in biological studies) and 2%. These concentrations are based on the approximate PST-lipid ratio *in vivo*. DLS was used to ensure no PST aggregates formed upon introduction to the vesicles or over the duration of a 24 hour experiment. At a temperature of 37 °C, time points of 0, 2, 6, 12, and 24 hours were tested. No aggregates were observed at any time point for the DMSO or DMSO-d6 solutions. Below Table 3.2 summarizes the different analysis methods used to analyze various combinations of vesicles compositions and PST concentrations. SANS, SAXS, and NSE measurements were also performed on IMM mimic vesicles in the presence of 1 volume percent DMSO or DMSO-d6 to examine if any solvent effects existed.

Vesicle Composition	Mole% PST	Analysis Methods
IMM Mimic	1	SANS, SAXS, NSE, and MD
IMM Mimic	1.5	SANS, SAXS, NSE, and MD
IMM Mimic	2	SANS, SAXS, NSE, and MD
TOCL/POPC Control	1	SANS, SAXS, NSE, and MD
TOCL/POPC Control	2	SAXS and MD
TOCL/POPE Control	1	SANS, SAXS, NSE, and MD
TOCL/POPE Control	2	SAXS, NSE, and MD

Table 3.2: Table showing the techniques used to analyze IMM, TOCL/POPC control, and the TOCL/POPE control with repect to PST mole percent.

SANS Measurements

SANS measurements were conducted on the NGB 30 m SANS instrument located at the National Institute of Standards and Technology Center for Neutron Research (NCNR, Gaithersburg, MD)[151]. Neutrons with a wavelength of 6 Å were used, as well as two sample-to-detector distances (1.33 m and 4 m), to access a scattering vector range of approximately 0.01 $Å^{-1} < q < 0.5$ $Å^{-1}$. LUVs at a concentration of 10 $^{mg}/_{mL}$ in D_2O were loaded into 1 mm path-length quartz banjo cells (Hellma USA, Plainsview, NY) and mounted in a Peltier temperature- controlled cell holder with ≈ 1°C accuracy. The scattered beam was counted on a 2D ^{3}He detector and subsequently radially-averaged, stitched, and corrected for background scattering from D_2O (SANS measurements showed no major differences in scattering between pure D_2O and D_2O with 1 vol% DMSO-d6, shown in Figure A.12) using Igor Pro and the appropriate macros provided by NCNR [152]. As a result, 1D scattering curves of total intensity against the scattering vector (I *vs.* q) were produced. The SANS data was analyzed used vesicle viewer software [153]. All measurements were collected at 37 °C.

SAXS Measurements

SAXS experiments were carried using the 12-ID-B beamline at the Advanced Photon Source (Argonne National Laboratory, Lemont, IL). An average photon energy of 13.3 keV was used and data was collected using 2M Pilatus detector (Dectris Ltd., Philadelphia, PA) set at a sample-distance of 2.0106 m. X-rays with a wavelength of 0.9322 Å were used. The resulting form factors in the scattering vector range of 0.03 $Å^{-1} < q < 0.9$ $Å^{-1}$ were background corrected using the established on-site reduction workflow and analyzed using vesicle viewer software [153]. All measurements were collected at 37 °C. LUVs at a concentration of 15 $^{mg}/_{mL}$ in H_2O were loaded into temperature controlled capillary cells. These cells oscillated ∼100 μL of sample to avoid ionization damage.

Neutron Spin-Echo Spectroscopy

Data was collected on the NG-A NSE spectrometer at the NCNR [154]. Neutron wavelengths of 8 Å and 11 Å were used to obtain a momentum transfer range of 0.045 $Å^{-1} < q < 0.1$ $Å^{-1}$. Fourier times of up to 100 ns were employed, allowing bilayer motions on length scales of ≈0.1 nm to 10 nm and time scales of 0.1 ns to 100 ns. LUVs at a concentration of 10 $^{mg}/_{mL}$ in D_2O were loaded into cells with a 4 mm path length for the NSE measurements. All samples were measured at 37 °C. Samples were allowed to temperature equilibrate for 30 minutes prior to evaluation, the temperature was maintained within ≈0.5 °C. The resulting

NSE data was reduced using the Data Analysis and Visualization Environment (DAVE) software package [155].

3.3.2 Computational

Atomistic MD simulations were performed using the GROMACS 2018.3 package [156] and the CHARMM36 force field [126]. The CHARMM PST force field was generously provided by Markus Miettinen from the Max Planck Institute for Colloids and Interfaces. The PST molecules were placed on one side of the membrane to be consistent with physical tests as PST was added externally during those experiments. Prior to the production runs for the PST containing membranes, multiple small simulation runs (20 ns each) were executed to bring the PST molecules closer to the membrane. All membrane compositions were generated using the CHARMM-GUI input generator [131]. The composition of all the vesicle systems used in simulations and total simulation time can be seen in Table 3.3.

Composition	Simulation Time (ns)	Number of Molecules					
		TOCL	POPC	POPE	H_2O	Na^+	PST
IMM Mimic	570	30	60	30	9000	60	0
IMM Mimic w/ 1% PST	560	30	60	30	8987	60	1
IMM Mimic w/ 1.5% PST	570	30	60	30	8971	60	2
IMM Mimic w/ 2% PST	550	30	60	30	8955	60	3
TOCL/POPC Control	540	60	60	0	12000	120	0
TOCL/POPC w/ 1% PST	530	60	60	0	11984	120	1
TOCL/POPC w/ 2% PST	550	60	60	0	11955	120	3
TOCL/POPE Control	530	60	0	60	12000	120	0
TOCL/POPE w/ 1% PST	560	60	0	60	11982	120	1
TOCL/POPE w/ 2% PST	560	60	0	60	11957	120	3
TOCL Control	560	90	0	0	13500	180	0

Table 3.3: Table showing simulation time and the amount of lipid species, water, sodium, and PST present in each vesicle compositions used for MD simulations.

Energy minimization and equilibration steps were performed according to the CHARMM-

GUI guidelines. The energy minimization began with steepest-descent minimization for 5000 steps followed by ensemble equilibration for 50 ps with a timestep of 1 fs, followed by isothermal-isobaric ensemble equilibration for 325 ps at a timestep of 2 fs, with semi-isotropic pressure coupling accomplished using the Berendsen barostat [157]. Equilibration was monitored by observing the system's area per lipid.

Unconstrained MD simulations were run for over 500 ns for each composition using a timestep of 2 fs. All simulations were kept at 37 °C using velocity-rescaling temperature coupling [158]. Pressure coupling was applied using the Parrinello-Rahman barostat [159]. A zero surface tension ensemble was created by setting a reference pressure of 1 bar for both the bilayer plane and the normal to the bilayer. Bilayer compressibility was set to 0.000045 bar^{-1}. Van der Waals interactions were cut off at 1.2 nm, and the interactions were modified using the force-switch method between 1.0 and 1.2 nm. Long-range electrostatics were determined using the particle mesh Ewald (PME) method, with a cutoff of 1.2 nm. The final 500 ns of the unrestrained MD simulations was used for data analysis. A combination of in-house scripts, GROMACS tools, and the Visual Molecular Dynamics (VMD) 1.9 program [160] were used to analyze the simulations. All errors were estimated using cumulative averaging.

Chapter 4

Results

4.1 Bilayer Structure

SANS and SAXS are proven techniques capable of resolving bilayer structure [161, 162]. To $q$uantify structural data from SAS the raw form factor must be modeled. The model used was a modified SDP model where SANS and SAXS data can be jointly analyzed, as shown in Figure 4.1 pertaining to data from the IMM mimic LUVs. The SDP model was previously eluded to in Section 2.1.1. SDP models are generated from the volume probabilities of membrane components (Figure 4.1E), which describes the likelihood of finding a specific membrane components at some distance from the bilayer center. The volume probability of each component is scaled to the electron $q$uantity and neutron SL of that components to generate ED (Figure 4.1C) and NSLD (Figure 4.1D) profiles [19]. The Fourier transform of the resulting ED and NSLD profile yields a form factor that can be compared to the raw form factor to accurately model and refine the data [19, 146, 163]. The optimized models for the SANS and SAXS data from the IMM mimic can be seen in Figure 4.1A-B. For all other compositions analyzed using SANS and/or SAXS, their form factors and corresponding fits can be found in Appendix A.

The SDP model used in the SANS and SAXS analysis parses the lipid membranes into 3 different components. The hydrocarbon chains were divided into two groups: the terminal methyl (CH_3, pink Gaussian in Figure 4.1C-E) and the rest of the hydrocarbon chain

(CH_2 CH, green Gaussian in Figure 4.1C-E). The headgroup region is the final grouping, it contains all remaining components of the lipid outside of the hydrocarbon chains (red Gaussian in Figure 4.1C-E). Water distribution (blue lines in Figure 4.1C-E) and combined SDP (grey lines in Figure 4.1C-E) are also described in the SDP model. The combined SDP calculated from MD simulations of the IMM mimic (purple lines in Figure 4.1C-E) are provided for a visual comparison between MD and SAS.

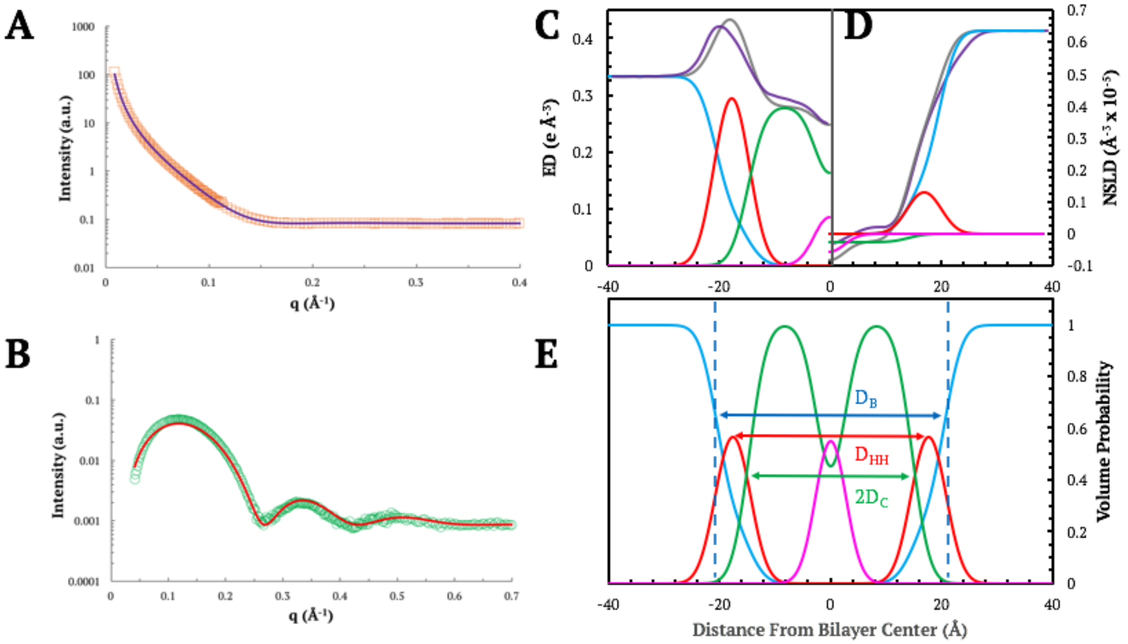

Figure 4.1: SANS (A) and SAXS (B) form factors with their corresponding SDP model fits (solid lines) for the IMM mimic LUVs. The SDP models of the IMM mimic LUVs are displayed in the upper-right panel, where the ED (C) is on the left half and the NSLD (D) is on the right half. The volume probability distribution is displayed in the bottom right panel (E), where the total probability is equal to 1 at each point along the bilayer normal.

A multitude of structural bilayer characteristics can be found using the SDP analysis model. Area per lipid (A_L) is an important parameter that can be extracted from analyzing SAS data. A_L is defined as the membrane surface area occupied by a lipid. Three types of membrane thicknesses were derived from the SAS data: Luzzati bilayer thickness (D_B), headgroup-to-headgroup distance (D_{HH}), and hydrocarbon thickness ($2D_C$). D_B is also known as the Gibbs dividing surface and can be described as the point along the bilayer normal at which the probability of finding a water and not finding a water is equal [164]. D_{HH} is described as the distance between electron density maxima, i.e. the distance between the electron-rich phosphorus atoms. $2D_C$ is defined as the distance between the *sn*-2 glycerol carbons as this is the starting point of the acyl chains. A graphical representation of D_B, D_{HH}, and $2D_C$ can be found in 4.1E and their values from SDP analysis can be found in Table 4.1. Crucially, A_L, D_B, D_{HH}, and $2D_C$ have proven to be an important parameters when looking at drug-membrane interactions [24, 26, 27, 109, 124].

Computationally, the structural parameters where calculated using GROMACS tools. Firstly, A_L was found by simply dividing the surface area covered by the bilayer in the XY-plane by the number of lipids in the XY-plane (see Figure 4.2).

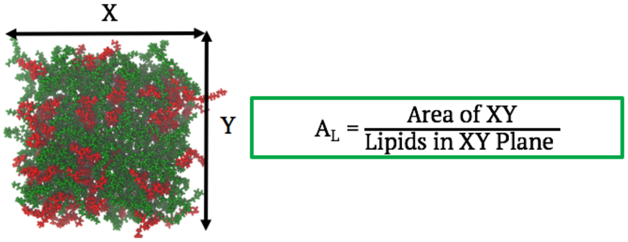

FIGURE 4.2: A bird's eye view of a lipid bilayer to show how A_L is extracted from MD simulations.

In order to find D_B the density profile of water in the simulations was found using gmx density. The point where the area underneath and above the water density curve is equal corresponds to D_B, as shown by the green shaded sections in Figure 4.3.

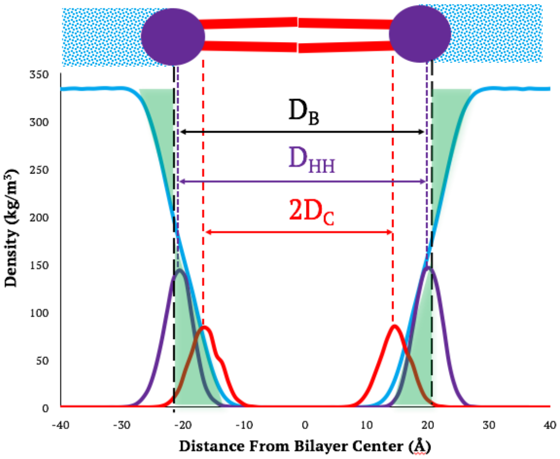

FIGURE 4.3: A visualization of how the densities of different bilayer components correlates to various types of membrane thicknesses, as shown using data from the IMM mimic simulation run. The density of water is represented by the blue line and corresponds to D_B (distance between dashed black lines), the density of phosphorus is represented by the purple line and corresponds to D_{HH} (distance between dashed purple lines), and the density of *sn*-2 is represented by the red line and corresponds to $2D_C$ (distance between dashed red lines).

By definition, this is the point where the probability of finding a water molecule and not finding a water molecule is equal. Finding D_{HH} and $2D_C$ requires a density profile to be made for the phosphorus atoms and the *sn*-2 carbon atoms respectively, as shown in Figure 4.3. Finding the distance between the maximum values of the density plot on each side of the bilayer will generate D_{HH} and $2D_C$. The values of A_L, D_B, D_{HH}, and $2D_C$ generated from MD simulations can be found in Table 4.1.

Vesicle Composition	A_L (Å^2)	D_B (Å)	D_{HH} (Å)	$2D_C$ (Å)
IMM Mimic (SAS)	80.9 ±0.2	40.6 ±0.5	41 ±0.5	31.3 ±0.4
IMM Mimic w/ 1% PST (SAS)	79.8 ±0.3	40.9 ±0.5	41.1 ±0.3	31.2 ±0.2
IMM Mimic w/ 1.5% PST (SAS)	79.4 ±0.4	41.3 ±0.2	41.6 ±0.4	31.9 ±0.3
IMM Mimic w/ 2% PST (SAS)	78.2 ±0.3	41.7 ±0.3	42.1 ±0.3	32.6 ±0.2
IMM Mimic w/ DMSO-d6 (SAS)	80.3 ±0.2	40.7 ±0.5	41.1 ±0.7	31.6 ±0.4
IMM Mimic (MD)	79.3 ±0.1	41 ±0.1	41.5 ±0.1	31.9 ±0.05
IMM Mimic w/ 1% PST (MD)	79.1 ±0.1	41.6 ±0.1	41.6 ±0.1	32.1 ±0.1
IMM Mimic w/ 1.5% PST (MD)	78.8 ±0.05	41.9 ±0.1	42.3 ±0.1	32.2 ±0.1
IMM Mimic w/ 2% PST (MD)	78.4 ±0.1	42.8 ±0.1	42.8 ±0.3	32.7 ±0.1
TOCL/POPC Control (SAS)	97.9 ±0.4	38 ±0.3	40.1 ±0.5	29.8 ±0.2
TOCL/POPC w/ 1% PST (SAS)	96.7 ±0.3	38.3 ±0.5	40.2 ±0.4	30.1 ±0.3
TOCL/POPC w/ 2% PST (SAS)	96.5 ±0.2	38.9 ±0.6	40.7 ±0.4	30.7 ±0.2
TOCL/POPC Control (MD)	97.6 ±0.05	37.1 ±0.05	39.9 ±0.1	29.2 ±0.1
TOCL/POPC w/ 1% PST (MD)	97.3 ±0.1	37.7 ±0.2	40.2 ±0.1	29.4 ±0.1
TOCL/POPC w/ 2% PST (MD)	97.2 ±0.1	37.7 ±0.05	40.3 ±0.1	29.7 ±0.1
TOCL/POPE Control (SAS)	95.9 ±0.1	35.9 ±0.2	39.4 ±0.4	29.7 ±0.3
TOCL/POPE w/ 1% PST (SAS)	95.6 ±0.2	36.3 ±0.4	39.6 ±0.3	30 ±0.3
TOCL/POPE w/ 2% PST (SAS)	94.7 ±0.4	36.5 ±0.1	40.0 ±0.3	30.2 ±0.2
TOCL/POPE Control (MD)	94.7 ±0.1	36.7 ±0.1	40 ±0.1	30.2 ±0.1
TOCL/POPE w/ 1% PST (MD)	94.3 ±0.1	36.9 ±0.1	40.4 ±0.1	30.7 ±0.1
TOCL/POPE w/ 2% PST (MD)	94.4 ±0.05	37.1 ±0.1	40.3 ±0.1	30.6 ±0.05
TOCL Control (SAS)	130.2 ±0.3	36.8 ±0.6	39.4 ±0.4	29.2 ±0.3
TOCL Control (MD)	132.2 ±0.1	36.6 ±0.1	39.1 ±0.2	29.1 ±0.1

Table 4.1: Structural parameters of various compositions generated from SDP model analysis and unrestrained MD simulations.

The A_L and thickness values from the SAS experiments and MD simulations are similar, as outlined in Table 4.1. This is also shown in Figure 4.1C-E, as the SDP models generated from SAS and MD are alike. This result displays the validity of the MD simulations. Furthermore, the A_L and thickness results agree with studies previously performed on pure TOCL bilayers [17, 136]. As for the other compositions, very little structural data has been reported in literature. A MD study recently reported D_{HH} values from compositions similar to the IMM mimic, the POPC/TOCL control and the POPE/TOCL control; the D_{HH} values agreed well with values reported in this thesis [134]. The A_L for the mixed compositions fall between the A_L values of TOCL and the A_L values of pure POPC [165] and/or POPE [23] bilayers. Two trends can be seen in Table 4.1: a decrease in A_L and an increase in membrane thickness. Aside from TOCL/POPE w/ 2% PST, every composition follows the PST dependant tendencies. These trends are visually represented in Figure 4.4, where structural data pertaining to the IMM mimic is plotted. Based on these findings, PST influences membrane structure properties. Possible explanations for these changes in A_L and membrane thickness will be discussed in Chapter 5.

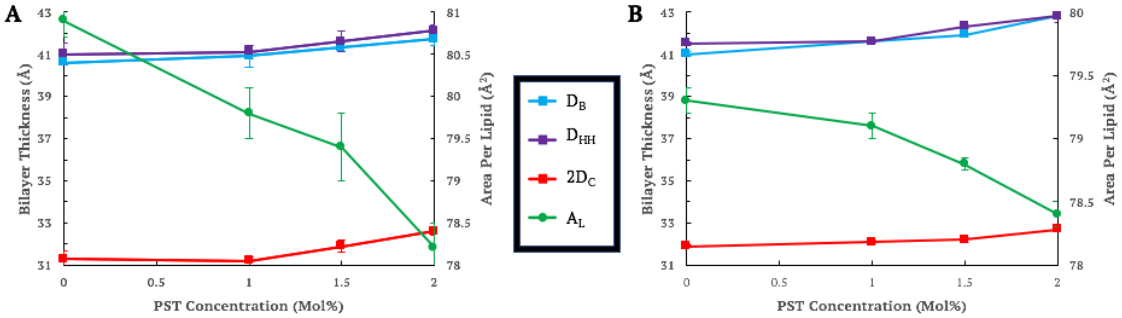

FIGURE 4.4: Graphs comparing structural data extracted from SAS (A) and MD simulations (B) of the IMM mimic with 0, 1, 1.5, and 2 mol% PST. Four parameters are shown: A_L, D_B, D_{HH}, and $2D_C$.

4.2 Membrane Rigidity

NSE measurements were performed to determine membrane bending rigidity with respect to PST concentration. The compositions mentioned in Tables 3.1 and 3.2 were used in the NSE experiments. NSE data were plotted using normalized intermediate scattering functions, $^{I(Q,t)}/_{I(Q,0)}$, which extract information regarding membrane undulations. Using the IMM mimic results as an example, when Fourier time is plotted against the intermediate scattering function it follows a stretched exponential (see Figure 4.5A) as predicted by Zilman and Granek for bilayer bending fluctuations where the bilayer is treated as a thin elastic sheet [114, 166] and defined as,

$$\frac{I(Q,t)}{I(Q,0)} \simeq e^{-DQ^2t} e^{-(\Gamma_{ZG}t)^{2/3}}. \tag{4.2.1}$$

In Equation 4.2.1, Q is the scattering vector, t is the Fourier time and D is the Stokes-Einstein diffusion coefficient ($D = {}^{k_BT}/_{6\pi\eta R}$) and is dependant on the hydrodynamic radius of the vesicle, R, solvent viscosity, η, absolute temperature, T, and k_B as the Boltzmann constant. As outlined by Hoffman et al. [167], D is a correction factor applied to account for contributions from vesicle diffusion. The hydrodynamic radii of the vesicles and their D values can be found in Table 4.2.

Vesicle Composition	Radius (nm)	D (${}^{\text{Å}^2}/_{\text{ns}}$)
IMM Mimic	69 ±4.6	0.394
IMM Mimic w/ 1% PST	69.2 ±4.1	0.393
IMM Mimic w/ 1.5% PST	68.4 ±4	0.397
IMM Mimic w/ 2% PST	69.3 ±4.7	0.392
IMM Mimic w/ DMSO-d6	68.5 ±5.1	0.396
TOCL/POPC Control	68.2 ±4.4	0.398
TOCL/POPC w/ 1% PST	69 ±4.9	0.394
TOCL/POPE Control	60.1 ±3.2	0.452
TOCL/POPE w/ 1% PST	59.7 ±3.1	0.455
TOCL/POPE w/ 2% PST	61.2 ±4.1	0.442

Table 4.2: Vesicle radii and corresponding Stokes-Einstein diffusion coefficients for the NSE samples.

Exponential fits with Equation 4.2.1 are displayed as solid lines in Figure 4.5A. From these fits the decay rates, Γ_{ZG}, were obtained. The decay rates follow the predicted linear dependency when plotted against Q^3 (see Figure 4.5B), where the slope is inversely related to the effective membrane bending modulus, $\widetilde{\kappa}$ [166]. Watson and Brown extended on the work of Zilman and Granek by accounting for the notable thickness and internal dissipation of a bilayer, which cannot be accurately described as a thin elastic sheet [168, 169]. They demonstrated that $\widetilde{\kappa}$ measured by NSE is related to the intrinsic bending modulus, κ, through

$$\widetilde{\kappa} = \kappa + 2d^2\kappa_m \tag{4.2.2}$$

where d describes the height of the neutral surface from the bilayers midplane (hypothesized to be 0.5) [114, 170] and κ_{m} is the monolayer compressibility modulus.

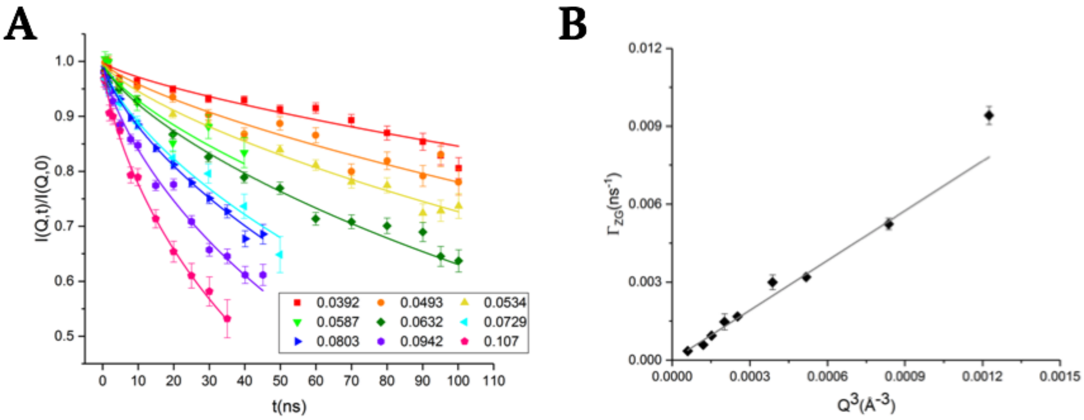

FIGURE 4.5: The normalize intermediate scattering function $I(Q,t)/I(Q,0)$ measured by NSE (A) and the linear dependence of the relaxation rate (Γ_{ZG}) with respect to Q^3 (B) for the IMM mimic. Error bars represent one standard deviation.

The Zilman-Granek and Watson-Brown theories were be used in conjunction to extract κ from the plot of Γ_{ZG} versus Q^3 (Figure 4.5B) by [170]

$$\frac{\Gamma_{ZG}}{Q^3} = 0.0069\sqrt{\frac{k_b T}{\kappa}}\frac{k_b T}{\eta}. \tag{4.2.3}$$

Equation 4.2.3 shows the inverse relationship between Γ_{ZG} and κ: a stiffer membrane will have a larger κ and a faster decay rate when compared to a softer membrane, which will have a smaller κ and a slower decay rate [114]. The κ results for the NSE experiments are shown in Table 4.3. The $I(Q,t)/I(Q,0)$ curves and Γ_{ZG} versus Q^3 plots for all samples aside from the IMM mimic can be found in Appendix B.

The bending rigidity of the MD simulations was determined using a computational methodology created by Doktorova and colleagues [138]. This technique analyses fluctuations in the lipid membranes and has generated values similar to those found using NSE on unsaturated lipid systems [138]. Using a distance cutoff of 14 Å to restrict the calculation to adjacent lipids, κ was analyzed by determining how neighbouring lipids interact with one another and how these interactions effect membrane undulations. The κ from the MD simulations can be seen in Table 4.3.

Composition	$\kappa(k_B T)$	
	NSE	MD
IMM Mimic	28 ±0.9	33.4 ±0.7
IMM Mimic w/ 1% PST	31.4 ±1	36.4 ±0.6
IMM Mimic w/ 1.5% PST	34.9 ±0.97	37.6 ±0.6
IMM Mimic w/ 2% PST	44.1 ±1.9	39.8 ±0.6
IMM Mimic w/ DMSO-d6	30.8 ±0.8	—
TOCL/POPC Control	30.8 ±0.6	31.2 ±0.6
TOCL/POPC w/ 1% PST	39.8 ±1.7	34.3 ±0.6
TOCL/POPC w/ 2% PST	—	36.3 ±0.6
TOCL/POPE Control	26.9 ±1	30.1 ±0.7
TOCL/POPE w/ 1% PST	29.9 ±0.8	32.8 ±0.5
TOCL/POPE w/ 2% PST	37.7 ±1.9	33.9 ±0.6
TOCL Control	—	30.5 ±0.8

Table 4.3: Bending modulus κ of various compositions found using NSE and/or MD simulations.

Aside from the TOCL control, the bending moduli for all other compositions have yet to be reported in literature. Thus, direct comparison with previous studies regarding κ is not possible. However, certain conclusions can be drawn. When compared to previous work on pure POPC and POPE bilayers, membrane order is increased by the presence of TOCL [23, 171, 172]. Additionally, CL has been shown to increase κ in PC membranes [173]. An increase in membrane order will make the bilayer more compact, leading to a larger κ value. Ordered domains within CL containing membranes have been shown in numerous studies, including studies on mixtures that include the main lipid constituents of the IMM [174], as well as bilayers composed of PE/CL [175–178]. Domains have not been reported in PC/CL membranes, but it is hypothesized that a superlattice structures exist [133, 179]. Our results follow this trend in that κ and the relative amount of CL are correlated. Additionally, the solvent effects of DMSO-d6 appear to be minimal. The inclusion of PST has a notably larger impact on κ than DMSO-d6 alone. This points to PST as the major influence on membrane stiffness, but the possibility of DMSO-d6 still acting as a chaperon for PST cannot be entirely dismissed.

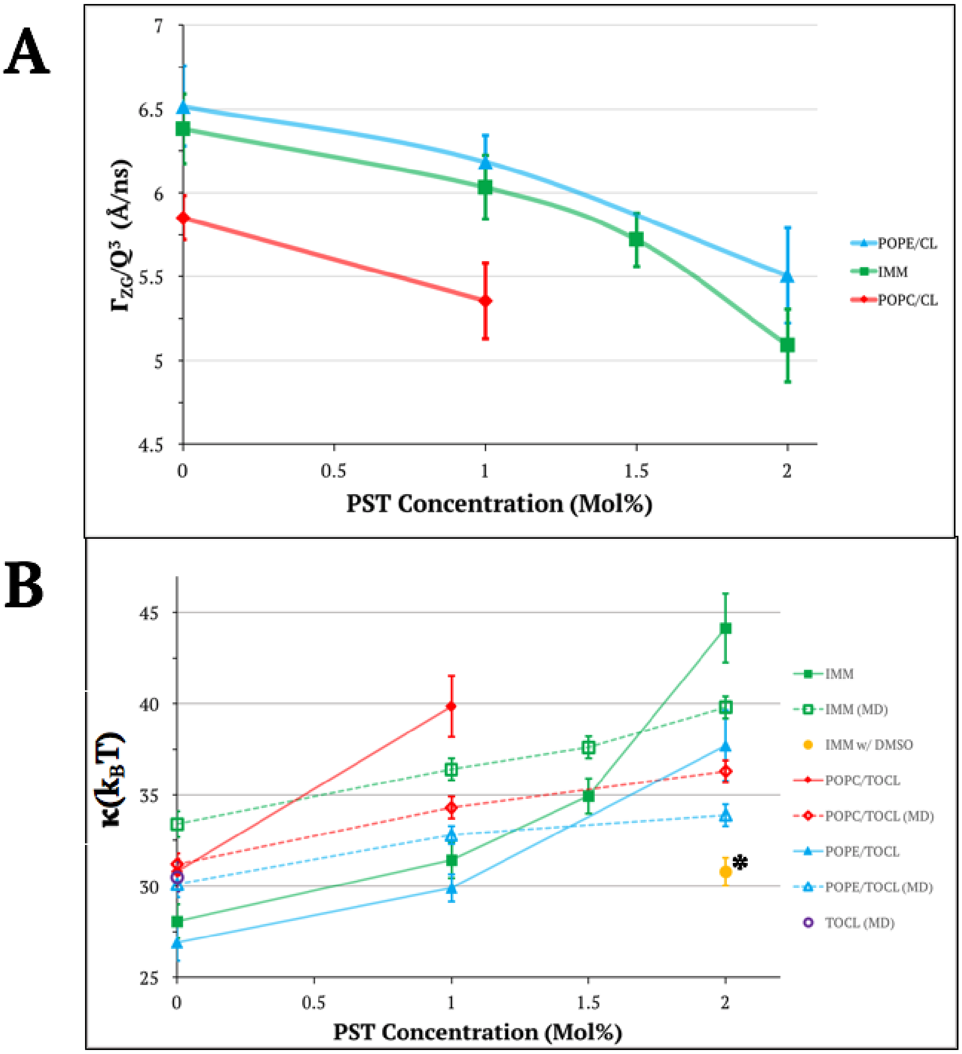

FIGURE 4.6: Decay rate Γ_{ZG} normalized by Q^3 for all Q for the IMM mimic, POPC/TOCL and POPE/TOCL samples with respect to PST concentration (A). Bending moduli (κ) for all samples with increasing amounts of PST measured by NSE and MD simulations (B). Note that the IMM mimic with DMSO-d6 (* in plot B) does not contain PST, but contains the volume of DMSO-d6 necessary to deliver 2 mol% PST.

The effect of PST is apparent when examining the decay rates and κ values. As previously eluded to, the decay rate and κ are inversely related. This is shown in Figure 4.6. In Figure 4.6A a decrease in Γ_{ZG}/Q^3 directly corresponds to an increase in κ as shown in 4.6B. Evidently, PST is stiffening the membrane and increasing κ for all compositions tested. This is true for both the NSE and MD experiments. It is also worth noting that PST makes the lipid bilayer more rigid regardless of composition.

4.3 Hydrocarbon Chain Order

The acyl chain order parameter (S_{CH}) was calculated from MD simulations to examine the impact of PST on membrane fluidity. S_{CH} provides information regarding the flexibility of the hydrocarbon chains, which has proven useful for understanding membrane phase behaviour [133, 180] and membrane interactions with drugs and other biomolecules [27, 181, 182]. S_{CH} is calculated by

$$S_{CH} = \frac{3}{2}\langle \cos^2 \theta \rangle - \frac{1}{2}, \tag{4.3.1}$$

where θ is the angle between the C-H bond vector and the bilayer normal. This equation describes the orientation of the C-H bonds in the acyl chains with respect to the bilayer normal averaged for all chains of a particular lipid over the sampling duration [183]. The magnitude of S_{CH} is directly related to acyl chain order, meaning a more ordered hydrocarbon chain will have a higher S_{CH} and vice versa.

The S_{CH} values were calculated for the *sn*-1 and *sn*-2 chains for all lipid species in each composition. The *sn*-1 and *sn*-2 chain length and degree of saturation varied with composition. TOCL only contains oleoyl chains (18:1), while POPC and POPE have a palmitoyl chain (16:0) in the *sn*-1 position and an oleoyl chain in the *sn*-2 position. It should be noted that the S_{CH} values reported for the *sn*-1 and *sn*-2 chains of TOCL are the averages of the findings from the two *sn*-1 and two *sn*-2 chains. The difference in saturation is visible in the S_{CH} plots in Figure 4.7, as double bonds are well known to encourage disorder. Figure 4.7 also displays PST's influence on the IMM mimic. A comparison of S_{CH} values between the 0, 1, 1.5, and 2 mol% PST for both the *sn*-1 and *sn*-2 chains of each lipid in the IMM mimic composition can be observed in 4.7. Furthermore, similar plots can be found in Appendix C for all other compositions.

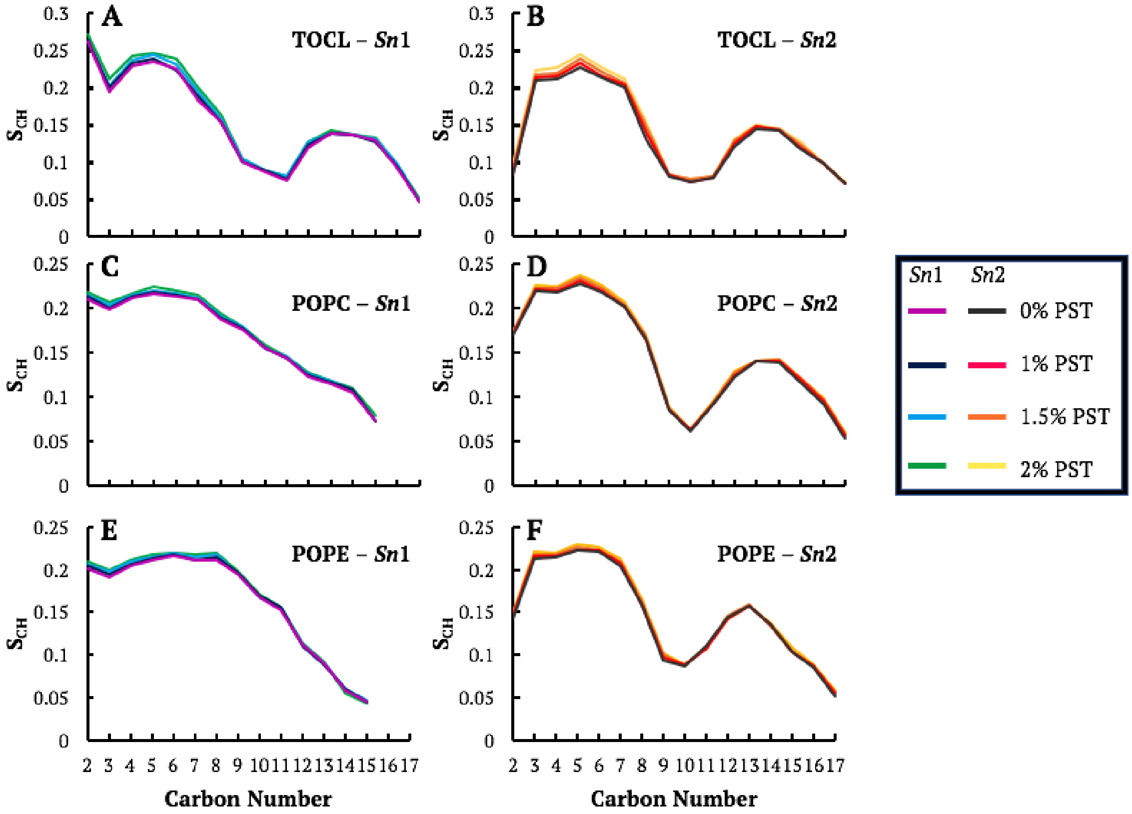

FIGURE 4.7: Acyl chain order parameters extracted from MD simulations of the IMM mimic with 0, 1, 1.5, and 2 mol% PST. Order parameters (S_{CH}) throughout the length of the *sn*-1 (A, C, and E) and *sn*-2 (B, D, and F) acyl chains are shown for the lipids that compose the IMM mimic: TOCL (A and B), POPC (C and D), and POPE (E and F).

Firstly, the trend in S_{CH} values found for all compositions is similar to those previously reported in literature [133, 135, 136, 184–186]. The S_{CH} results indicate that carbons closer to the glycerol backbone are more susceptible to ordering by PST, as shown by the increase in S_{CH} from 0 to 2 mol% PST. This is most evident in the TOCL S_{CH} values between C2-C8 for both the *sn*-1 and *sn*-2 chains. PST enforces the same trends mentioned above on the POPC/TOCL and POPE/TOCL controls (see Appendix C. Moreover, this trend appears to be more obvious for the POPC/TOCL and POPE/TOCL controls, possibly caused by the higher concentration of TOCL present in those compositions. The increase in acyl chain order provides an explanation to the climbing κ values shown in Section 4.2, as a more ordered membrane would be stiffer. PST appears to have little to no impact on the chain order as the proximity to bilayer center decreases. This points to PST interacting with the headgroup region of the lipid, which corroborates with the thickness and A_L changes described Section 4.1.

4.4 PST Localization

The location of PST relative to the lipid bilayer was found for various MD simulations. Finding where drugs sit in relation to the membrane is key to understanding how they influence membrane properties, and consequently biological events [24, 26–28, 109, 124, 187]. To find where PST localizes the density of PST was averaged over final 500 ns of each simulation containing PST. It should be noted that PST density is plotted against the distance from bilayer center, but only for the half of the membrane where the PST molecules were placed to be consistent with experimental procedure. An example of a PST density profile is shown in Figure 4.8, where the density of PST is plotted against distance from bilayer center. The PST density profiles from the IMM bilayers is shown in Figure 4.8, while the PST density profiles for all other compositions can be found in Appendix D.

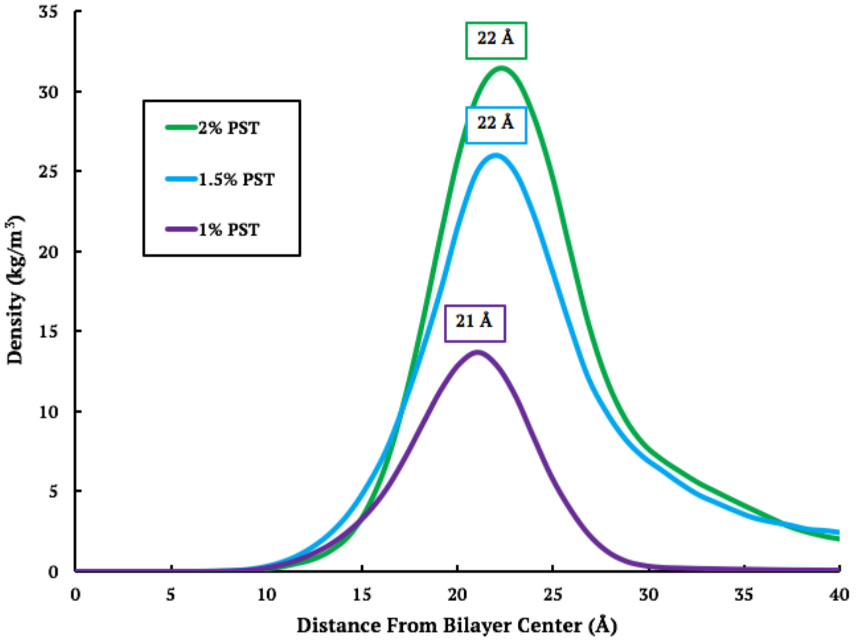

Figure 4.8: PST density profiles extracted from MD runs of the IMM mimic bilayers in the presence of 1, 1.5, and 2 mol% PST. The numbers inserted at the maximum amplitude of each curve correspond to the distance from bilayer center at which the maximum value occurs.

Based on the PST density profiles, it can be concluded that PST is concentrated on the surface of the membrane. The maximum PST density for all simulations are between 21-23 Å, falling only slightly outside the $\mathrm{D_B}$ and D_{HH} values reported in Table 4.1 if they were cut in half. This demonstrates that PST localizes at the membrane surface regardless of composition. This results clearly shows that PST has a stronger affinity to the membrane than the surrounding water, which is logical due to PST's lack of solubility in water [149]. Also, visual examination of the simulations showed that PST did not cross the membrane. The position of PST relative to the membrane supports results found in Section 4.2, which will be discussed in Chapter 5.

4.5 PST's Lipid Preference

The lipid favouritism of PST was investigated to using MD simulations. Recent studies have shown that some molecular therapeutics associate more with specific lipid species [28, 187], which could impact biological processes where that lipid species plays a valuable role. To determine if PST has a lipid bias the radial distribution function (RDF), *g(r)*, between PST and each lipid species in a membrane was computed for all PST containing simulations. The RDF describes the how the density of a defined portion of matter changes as a function of distance from a point. During MD simulations, PST was inserted into the solvent in a random manner. Therefore, if PST closely associates with a particular lipid species, that lipid species is likely significant to PST's functionality and interacts with PST in a more favourable manner than the other lipids.

In order to calculate the RDF two molecules or points within two molecules must be specified. In the case of this thesis, the center of mass of both PST and the headgroup of the chosen lipid species was used. The lipid headgroup was defined as the functional groups attached to the *sn*-3 carbon of the glycerol chain. For TOCL, this included the glycerol bridge connecting the two phosphate groups. After defining the two groups of interest, the RDF was calculated over the duration of each simulation, resulting in a plot of g(r) versus distance. These graphs show the density of a specific lipid headgroup changes over certain distance from a PST molecule. RDF plots can be found in Figure 4.9A-C for all PST containing simulations on the IMM mimic composition. The RDFs for the POPC/TOCL and POPE/TOCL controls with 1 and 2 mol% PST can be found in Appendix E.

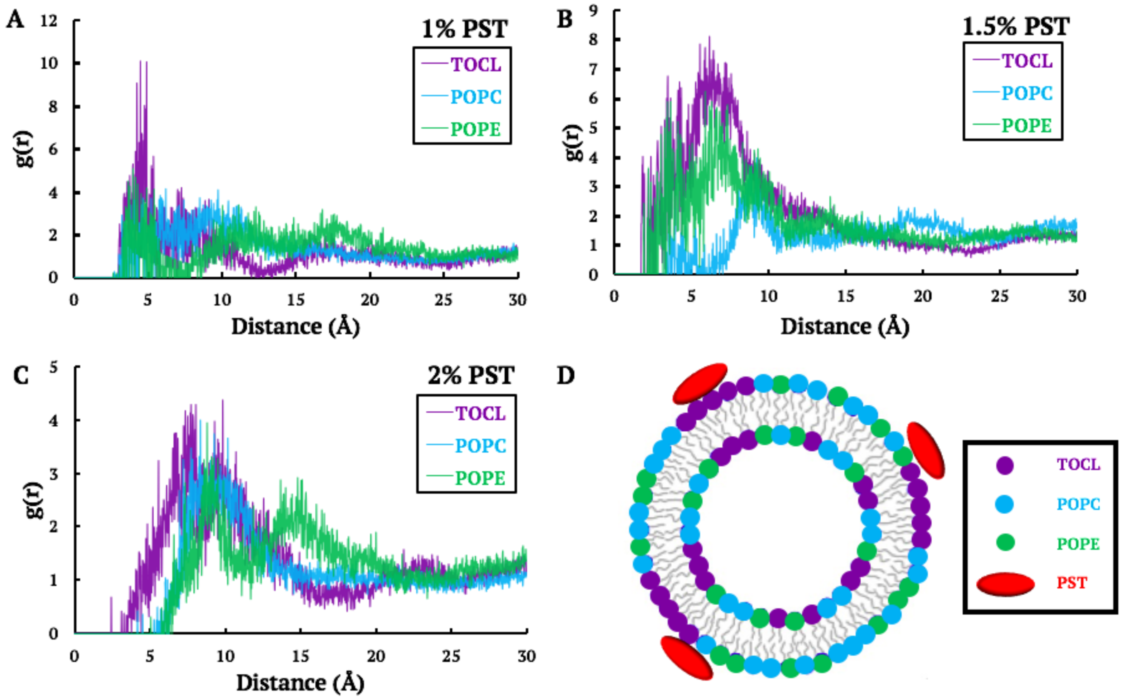

Figure 4.9: RDF graphs for MD simulations corresponding to the IMM mimic with 1 (A), 1.5 (B), and 2 (C) mol% PST. The bottom-right panel (D) shows a cartoon of PST more closely associating itself with TOCL rather than other present lipid species.

The results from the RDFs show that PST has a clear inclination to associate with TOCL over POPC or POPE. In Figure 4.9A-C it is clear that the number of TOCL head-groups is greater than the other lipids when in close proximity to PST. This finding is especially notable considering TOCL only accounts for 25 mol% of the IMM mimic. Therefore, TOCL must have a momentous interaction with PST in order to draw PST away from the only lipid species occupying the remaining 75 mol% of the IMM mimic. Figure 4.9D provides a cartoon depiction on how PST tends to localize near area of high TOCL concentration. Essentially, PST sits near the surface of the membrane that is occupied by a high number of TOCL lipids. This suggests that TOCL rafts or domains are forming either prior to interacting with PST or as a result of the PST-TOCL dynamic.

To further investigate the possibility of TOCL domains existing before or as a result of PST addition, the RDFs between lipid species in the IMM mimic simulations was assessed. These RDF plots are shown in Figure 4.10, where a higher *g(r)* value at a smaller distance indicates that the chosen lipid species are closer to each other in the membrane. Figure 4.10 show the RDF plots for POPC and POPE in relation to TOCL, as well as the RDF for TOCL with other TOCL molecules, at each PST concentration. Based on 4.10, TOCL lies closest to other TOCL lipids, regardless of PST concentration. Considering TOCL only accounts for 25 mol% of the membrane, its evident that TOCL molecules have an inclination towards other TOCL molecules. This indicates that TOCL may form an ordered domain before PST is added and not as a result of PST's introduction. Considering PST has a high affinity for TOCL, its possible that TOCL domains could be a target for PST. This idea and its biological repercussions will be further discussed in Chapter 5.

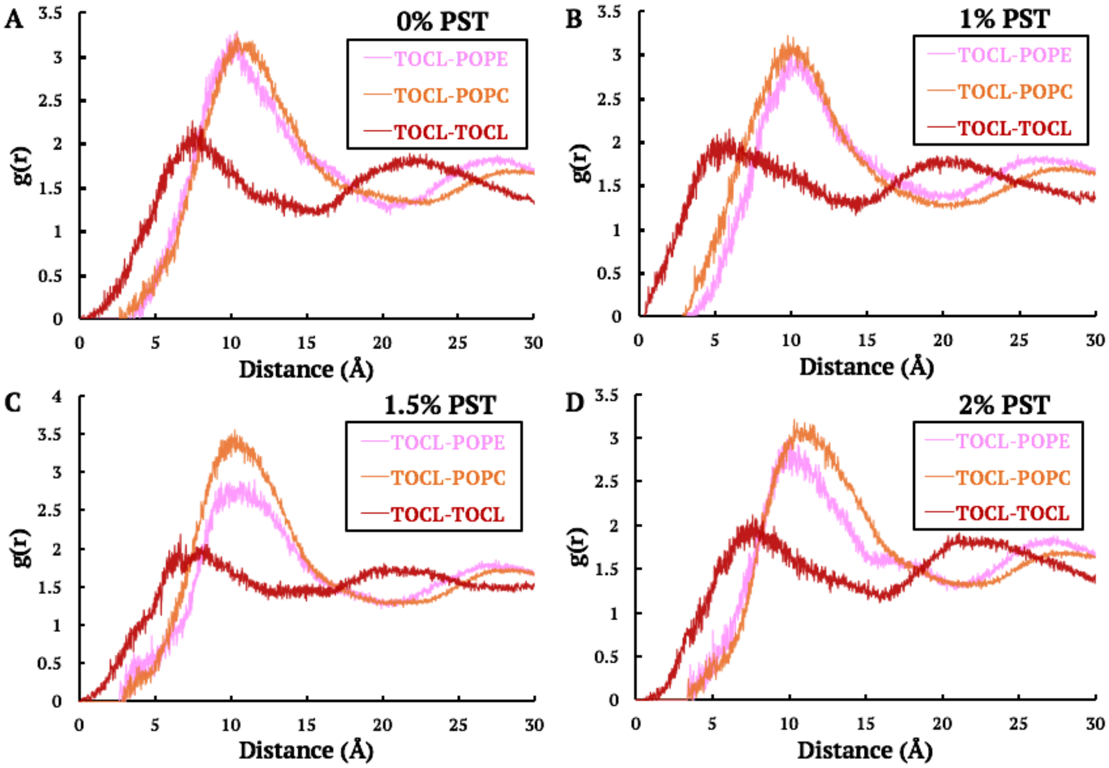

Figure 4.10: RDF graphs for MD simulations corresponding to the IMM mimic with 0 (A), 1 (B), 1.5 (C), and 2 (D) mol% PST. These plots examine the distance between the different lipid species as more PST is added to the system.

The association of PST with TOCL is more evident in the POPC/TOCL (Figure E.1) and POPC/TOCL (Figure E.2) controls. This is likely due to the higher concentration of TOCL, as TOCL would cover a larger surface area and be more readily available to interact with PST. However, the affinity between PST and TOCL is still evident as it clearly interacts more than with POPC or POPE at an equal concentration. When comparing the RDFs of POPC and POPE its noticeable that POPE has a stronger inclination towards PST than POPC (see Figures 4.9A-C, E.1, and E.2. This is a noteworthy finding considering the IMM mimic only contains 25 mol% POPE.

It should also be noted that the hydrogen bonding of each lipid species with PST was examined to determine if hydrogen bonding was the reason behind PST's affinity to TOCL. It was determined that PST showed very little hydrogen bonding with lipid headgroups. Furthermore, the small amount of hydrogen bonding that did occur was evenly distributed between the different headgroups, where the number of hydrogen bonds per lipid with PST ranged between 0.02-0.04. This points out that hydrogen bonding is unlikely responsible for PST's attracting to TOCL.

Chapter 5

Discussion

5.1 PST's Impact on Membrane Stiffness and Structure

Anti-cancer drugs have previously shown condensing effects on lipid bilayers [188–190]. These studies pointed to a drug-headgroup interaction as the source of the condensing effect. A similar outcome is seen when PST interacts with lipid bilayers, where rigidity increases, A_L decreases, and bilayer thickness increases, all of which are signs of a more ordered membrane. A possible explanation for these effects is that PST sits directly on top of the lipid headgroups. When unaccompanied by PST, the membrane is free to bend without restriction. When PST is present it acts as a physical obstruction that interferes with membrane undulations (see Figure 5.1), consequently causing an increase in κ.

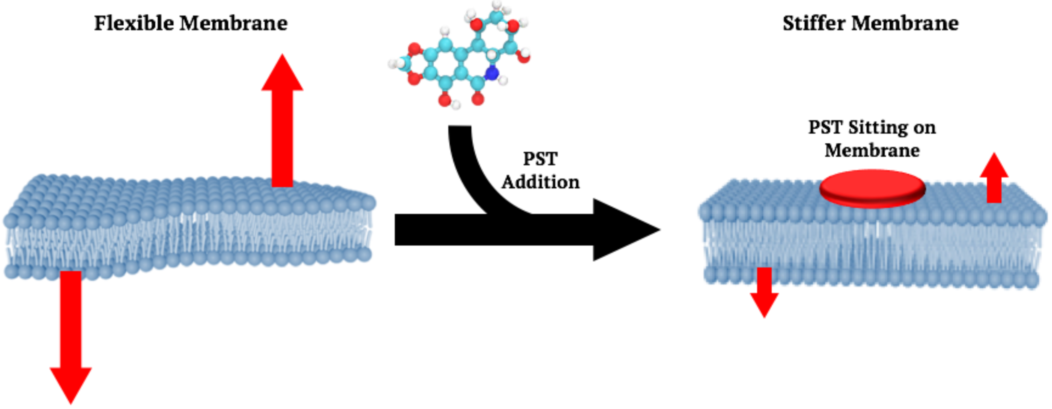

FIGURE 5.1: Illustration of how PST sits on the surface of the lipid bilayer, dampening membrane bending fluctuations by condensing the membrane.

The observed dampening effect can be explained by PST acting as a anchoring point on the bilayer sheet. The PST anchors dampen longer wavelength modes of the bilayer bending resulting in an overall stiffening of the bilayer. This explanation is supported by the distribution of PST from MD A possible implication of PST stiffening the IMM in cancerous mitochondria will be explored in Section 5.4.

Like cholesterol, PST is a molecule that condenses fluid membranes by creating more ordered phases [172, 180, 191]. Although both PST and cholesterol are order inducing agents, that is where their similarities end. Cholesterol inserts into a fluid membrane, where through hydrogen-bonding with phospholipids it causes bilayer condensation [172]. In contrast, results reported in this thesis show that PST does not enter the membrane, instead impacting membrane dynamics via surface interactions. Interestingly, PST appears to increase κ more than cholesterol at a smaller mol% [172]. However, PST appears to be lipid selective, while cholesterol effects a much broader range of lipids, displaying both ordering and disordering effects [180].

The variation in κ between the compositions examined with NSE and MD can be explained by considering that POPC and POPE may interact with CL in different ways. PC/CL membranes have not demonstrated the ability to form domains, but the idea that they form ordered superlattices has been proposed [179]. PE/CL membranes on the other hand are heavily linked with CL domain formation [175–178]. Although domains and superlattices are ordered, both are transient and dispersed randomly across the membrane, making them difficult to detect. It's possible that a POPC/TOCL superlattice may account for the higher κ values when compared to the POPE/TOCL domains, simply due to superlattices forming more often. This is feasible considering the formation of a superlattice is energetically favourable [179].

As previously stated, the structural parameters found from SAS and MD show that PST is condensing the membrane. As a membrane is condensed its thickness increases due to tighter lipid packing, which consequently results in a decrease in A_L. The structural parameters varied with PST concentration in a linear fashion. A similar trend was recently reported regarding the condensation of POPC membranes by carotenoids [192]. Considering no plateau was reached regarding the effect of PST on membrane structure, its possible that a higher dose of PST could further change membrane properties. However, it should be stated that the quantities of PST examined here have shown efficacy [36, 37, 101, 102].

5.2 Bilayer Organization

Using both experimental and computational methods, lateral heterogeneity has been reported in membranes containing CL, PE and PC lipids [64, 174–179]. In these studies CL forms the ordered domain, while the other lipids are found in a less ordered state. These CL rafts are important for the function of membrane associated proteins, including portion of the ETC [3, 20]. The exact driving force of CL segregation is not entirely understood, as some recent literature has pointed that CL does not form domains, but simply localizes in area of high curvature due to its considerable negative curvature [193]. Regardless, both conjectures point to CL segregation in some manner. Results reported in this thesis suggest that TOCL localization may exist in the tested membrane compositions and are effected by PST. Firstly, the results from the RDF calculations (Figure 4.10) indicate that TOCLs lie closer to each other than POPC and POPE, and this does not change when PST is present. This supports that TOCL-heavy areas may form in the presence of POPC and POPE, but this is far from conclusive. This result is not direct evidence of domain formation, as techniques such as fluorescence microscopy and contrast-matched SANS, are required to confirm the presence of lipid rafts [194–196]. However, it is still notable that the membrane simulations of the IMM mimic show that TOCL lipids have a degree of lateral organization that is maintained throughout the addition of PST and not caused by the addition of PST. Furthermore, it points out that domain disruption is an unlikely method of action for PST.

5.3 Membrane Order and PST's Affinity to Cardiolipin

Interestingly, PST induces membrane order. This occurs consistently as PST concentration increases for all compositions, and is shown by the increase in chain order, increase in κ, and changes in structural parameters. More specifically, PST increases the order of TOCL carbons close to the headgroup. Based on this finding, PST targets areas of the membrane where TOCL is abundant and condenses the membrane by interacting with the headgroups of TOCL. Although the condensing effect of PST is evident, the nature of its interaction with TOCL remains unclear.

Based on the analysis of the MD simulation, hydrogen bonding is not the cause of the PST-TOCL relationship. The unique shape of CL lipids provides a possible explanation for the affinity between PST and TOCL. As discussed in Chapter 1, CL lacks the shielding characteristics of other lipids, leaving the negative charge of their headgroup open to the aqueous environment and available for electrostatic interactions [66, 67]. Previous work has noted that CL's bonding tendencies are not fully understood, but evidence shows that CL binds to proteins in a non-selective and ionic fashion, while peripheral protein seek out CL over other phospholipids [197–199]. Considering CL binds to proteins in a non-specific fashion, its possible PST binds to CL in a similar manner. TOCL's exposed headgroup may provides a binding opportunity to PST, explaining PST's affinity to TOCL.

5.4 Possible Apoptotic Consequences

Due to the high proliferation rate and energetic needs of cancer cells, many cancers turn to oxidative phosphorylation and aerobic respiration in tandem to meet energy requirements [87–92]. This presents the ETC as a target for anti-cancer drug therapies, as the various protein complexes can be targeted to disrupt the chain [77, 87]. One way PST could target the ETC is by changing the fluidity of the IMM and by limiting the capabilities of CL. Literature has shown that CL is strongly linked with cytochrome c oxidase (complex IV), where it helps transfer protons and maintain protein functionality [59, 141, 200–202]. The binding of PST to the headgroup of CL would limit its proton trapping ability, while simultaneously stiffening the membrane. A stiffer membrane would limit the structural flexibility of CL, likely limiting its interactions with cytochrome c oxidase as it would not be able to fulfill its role of providing structural support to the enzyme [199, 200]. This could greatly lower the efficiency of cytochrome c oxidase, possibly compromising the ETC. A similar conclusion could be drawn regarding NADH:ubiquinone oxidoreductase (complex I), where CL is responsible for regulating the membrane domains of the enzyme [16]. In a similar fashion as described above, the association of PST with CL could change the way CL interacts with the membrane domains of NADH:ubiquinone oxidoreductase, weakening enzyme dynamics by weaking CL modulation. Taken together, the conceivable impact of

PST on the complexes of the ETC could greatly lower the efficiency of said enzymes and bring oxidative phosphorylation in cancer cells to a halt.

Intriguingly, PST could accelerate a well established apoptotic sequence that occurs in the mitochondria. Also, literature shows a link between cytochrome c and apoptosis, where the release of cytochrome c from the IMM begins an apoptotic cascade involving caspases that degrade cell components and ultimately cause cell death [3, 60, 199, 203, 204]. CL rich areas form a functional platform for cytochrome c, where CL changes the enzyme's usability and conformation [205–207]. A feasible mechanism of action for PST is shown in Figure 5.2, where PST would obstruct cytochrome c from accessing the CL dense portions of the membrane, forcing it to release from the IMM and consequently begin the caspase cascade. Deficiencies in CL have shown an increase in apoptosis due to cytochrome c release [204, 208], and PST could induce a similar effect by eliminating the functional capabilities of CL. Furthermore, previous works show that PST enhances caspase protein activity [37, 99]. Our results suggest that the apoptotic power of PST may occur due to its ability to interact with CL while simultaneously inhibiting cytochrome c interactions, leading to cancer cell apoptosis.

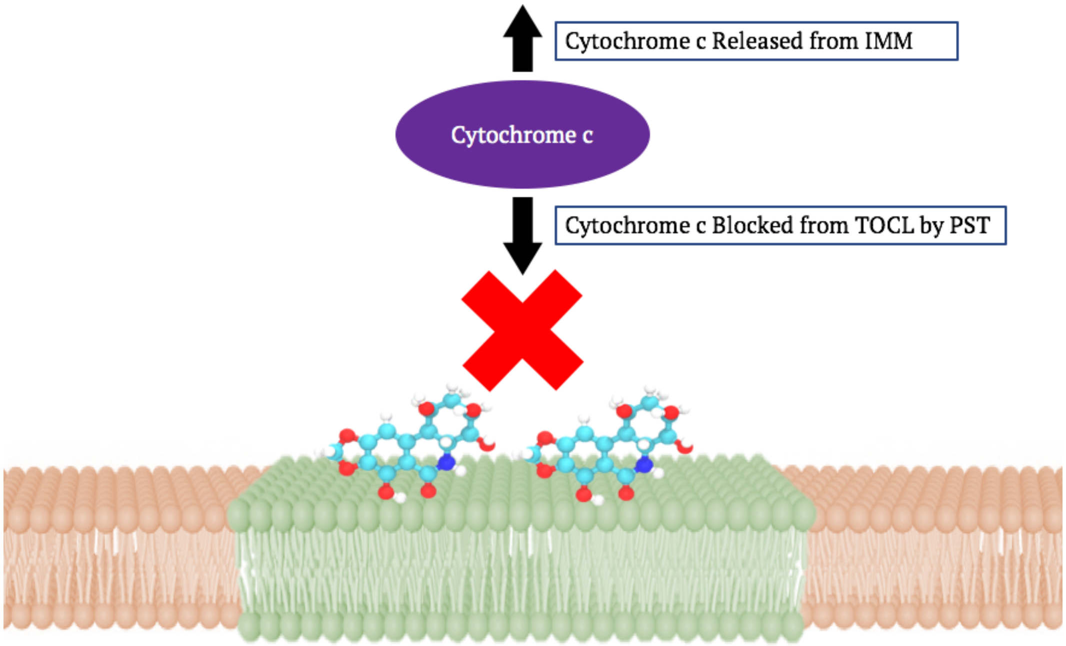

Figure 5.2: Image depicting a hypothesized method of action for PST against cancerous mitochondria. PST sits on the surface of the membrane where TOCL is highly concentrated (green lipids), as opposed to the less ordered portion of the membrane (orange lipids).

The proposed method of action for PST is similar to the mechanism for doxorubicin, a well studied anti-cancer agent. Doxorubicin induces apoptosis by releasing cytochrome c into the intermembrane space [209–212]. This sets a precedent in that the proposed mechanism for PST has been demonstrated in another anti-cancer molecule. One advantage PST has over doxorubicin is that its not cytotoxic to healthy cells [213]. In conclusion, the results suggest that PST may cause cell death in a similar manner to doxorubicin, but without the negative toxic effects.

Chapter 6

Conclusion

In an effort to better understand the anti-cancer mechanism of PST on a molecular level, various biophysical techniques were employed to determine how it interacts with membranes. Data was collected using SANS, SAXS, NSE, and MD simulations, all of which showed consistent results regarding PST's condensing effect on TOCL containing bilayers. Interestingly, PST was shown to have a stiffening effect on membrane dynamics at biologically relevant concentrations, which correlated well with the bilayer structural data. This increase in membrane rigidity could directly impact ETC complexes as it may compromise their structural stability. The results from the RDF calculations and lipid chain order show a clear affinity between PST and TOCL. In conclusion, the data presented in this thesis established a connection between PST and TOCL bearing model membranes, pointing to the possibility that the lipids of the IMM may be the target of PST. Furthermore, a proposed mechanism of action was presented that will inspires future studies into the effect of PST on CL membranes.

Appendices

Appendix A

Small-Angle Scattering Curves

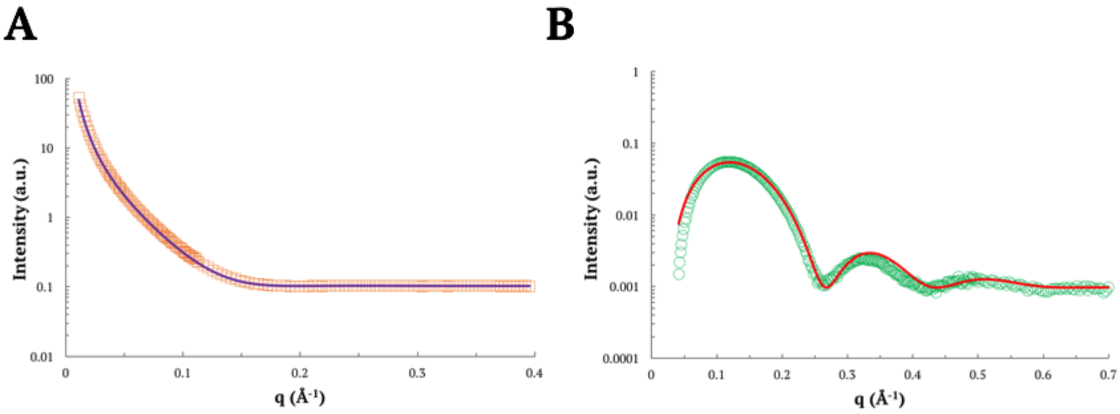

Figure A.1: SANS (A) and SAXS (B) data from TOCL LUVs (open symbols) and the corresponding fits (lines) to the SDP model.

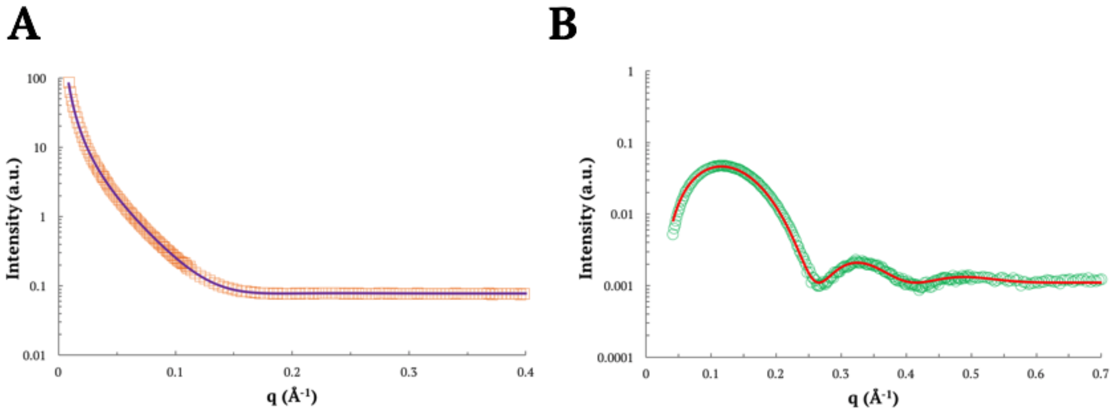

Figure A.2: SANS (A) and SAXS (B) data from IMM mimic LUVs in the presence of 1 mol% PST (open symbols) and the corresponding fits (lines) to the SDP model.

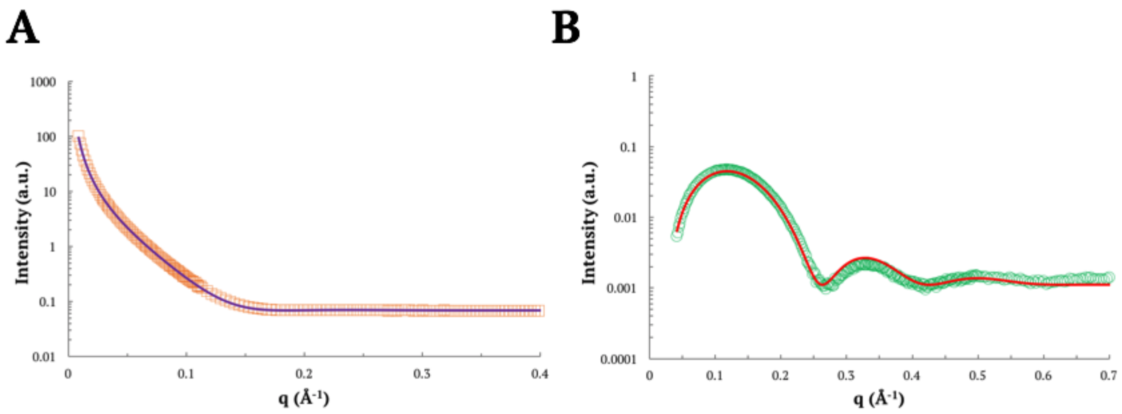

Figure A.3: SANS (A) and SAXS (B) data from IMM mimic LUVs in the presence of 1.5 mol% PST (open symbols) and the corresponding fits (lines) to the SDP model.

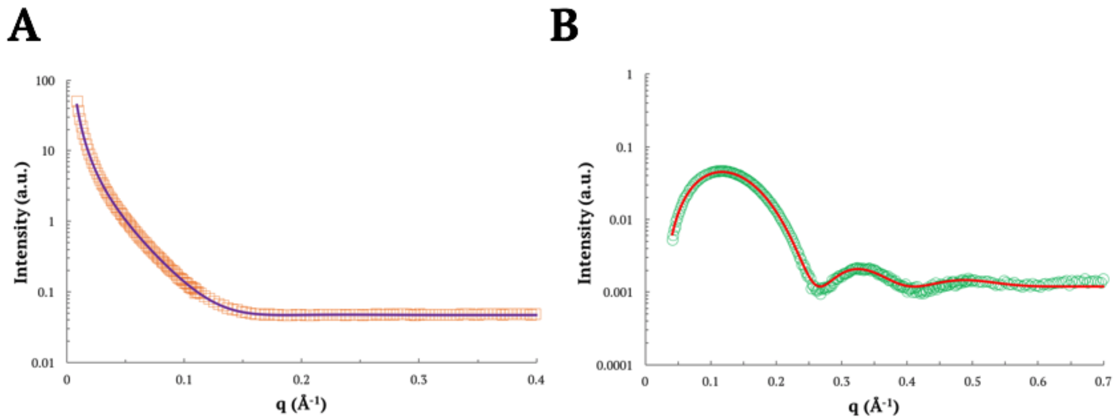

Figure A.4: SANS (A) and SAXS (B) data from IMM mimic LUVs in the presence of 2 mol% PST (open symbols) and the corresponding fits (lines) to the SDP model.

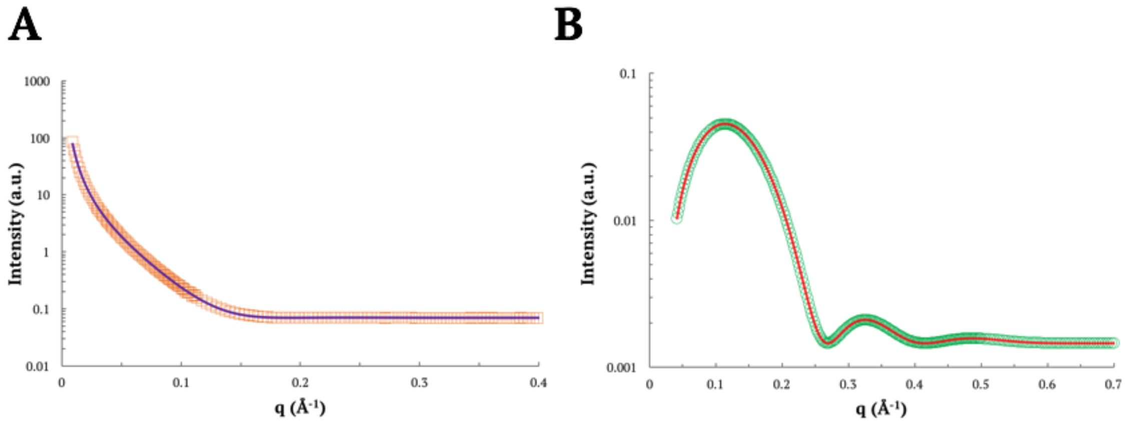

Figure A.5: SANS (A) and SAXS (B) data from IMM mimic LUVs in the presence of 1 vol% DMSO-d6 (open symbols) and the corresponding fits (lines) to the SDP model.

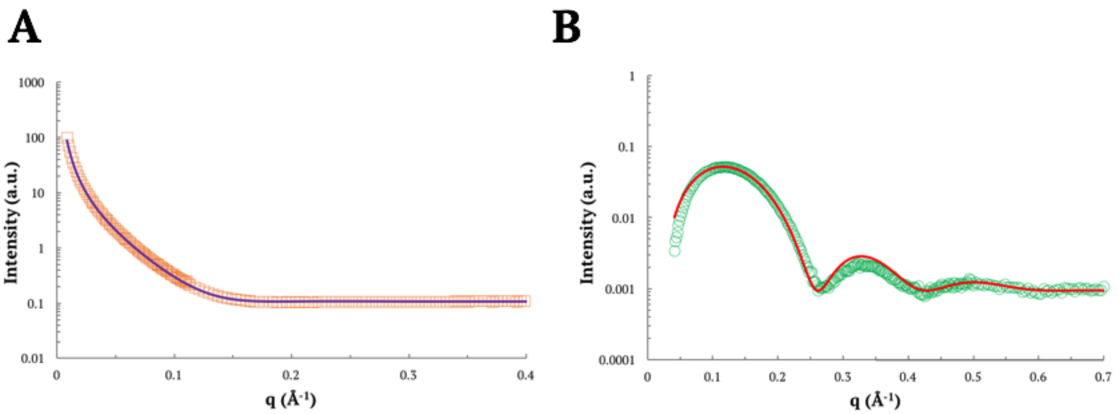

Figure A.6: SANS (A) and SAXS (B) data from POPC/TOCL control LUVs (open symbols) and the corresponding fits (lines) to the SDP model.

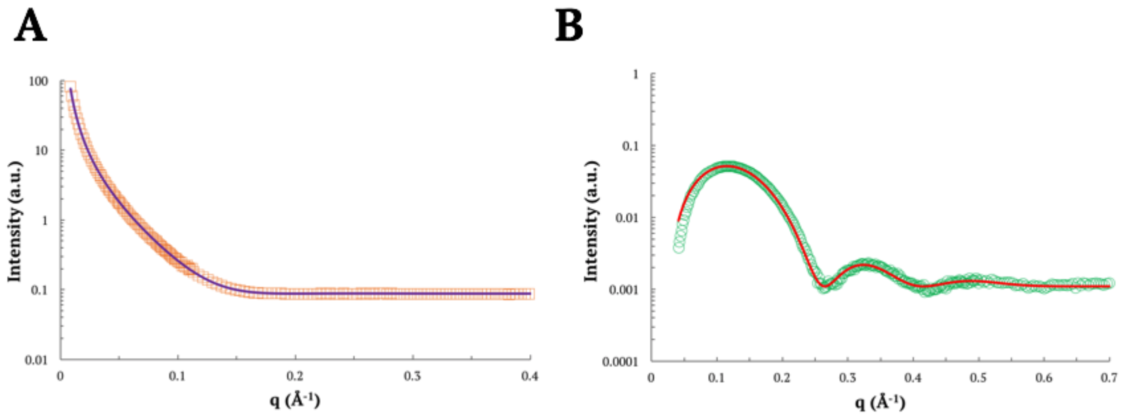

Figure A.7: SANS (A) and SAXS (B) data from POPC/TOCL control LUVs in the presence of 1 mol% PST (open symbols) and the corresponding fits (lines) to the SDP model.

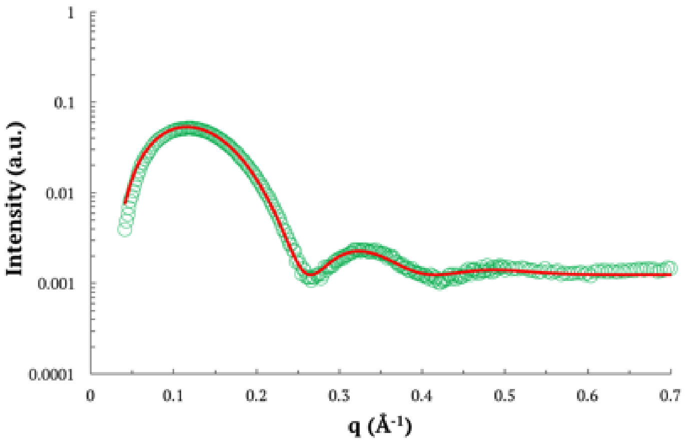

Figure A.8: SAXS data from POPC/TOCL control LUVs in the presence of 2 mol% PST (open symbols) and the corresponding fit (lines) to the SDP model.

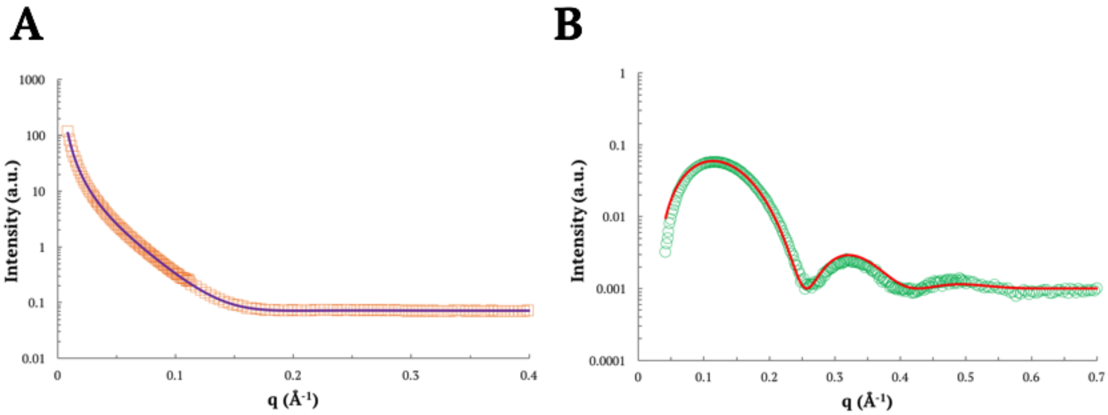

Figure A.9: SANS (A) and SAXS (B) data from POPE/TOCL control LUVs (open symbols) and the corresponding fits (lines) to the SDP model.

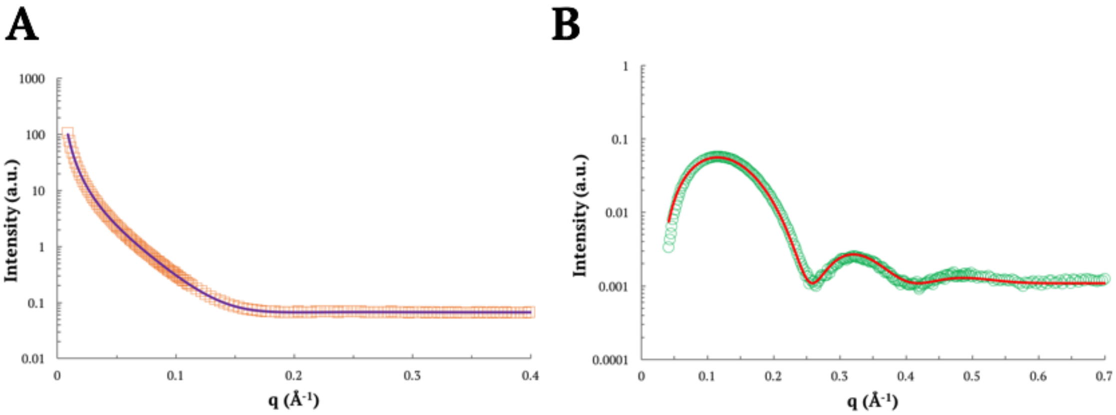

Figure A.10: SANS (A) and SAXS (B) data from POPE/TOCL control LUVs in the presence of 1 mol% PST (open symbols) and the corresponding fits (lines) to the SDP model.

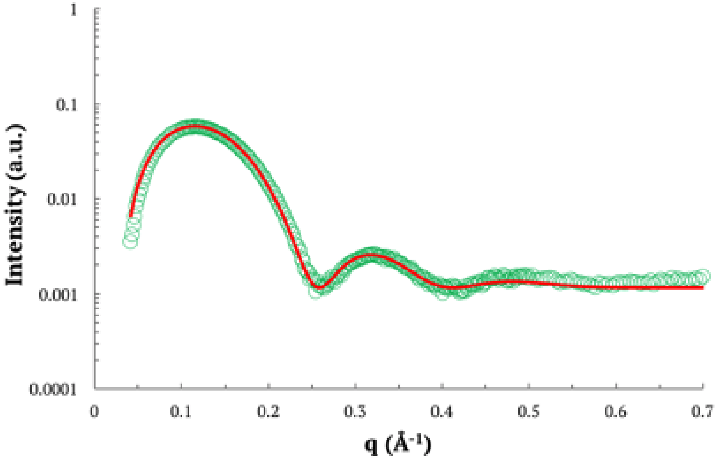

Figure A.11: SAXS data from POPE/TOCL control LUVs in the presence of 2 mol% PST (open symbols) and the corresponding fit (lines) to the SDP model.

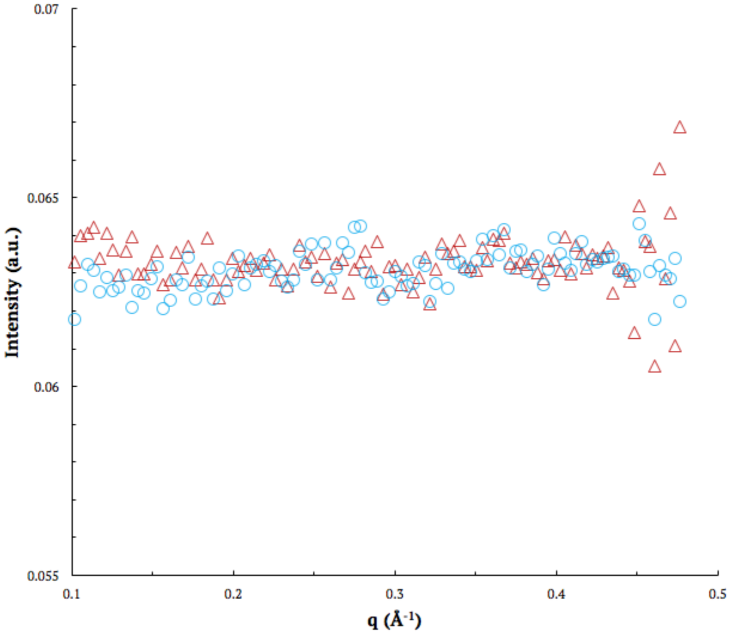

FIGURE A.12: Zoomed in view of SANS data from D_2O (blue circles) and from D_2O with 1 vol% DMSO-d6 (red triangles).

Appendix B

Intermediate Scattering Curves and Decay Rates

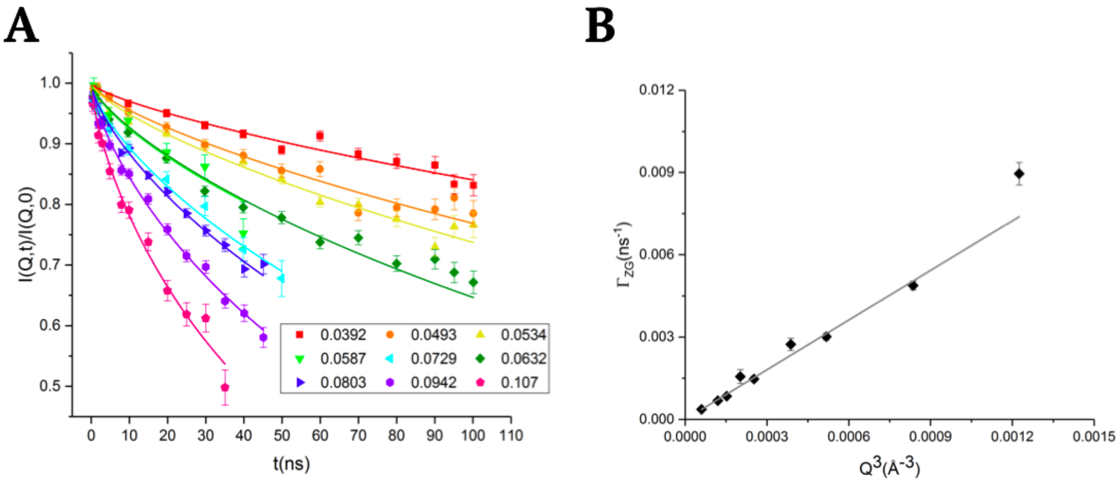

FIGURE B.1: The normalize intermediate scattering function $I(Q,t)/I(Q,0)$ measured by NSE (A) and the linear dependence of the relaxation rate (Γ_{ZG}) with respect to Q^3 (B) for the IMM mimic with 1 mol% PST. Error bars represent one standard deviation.

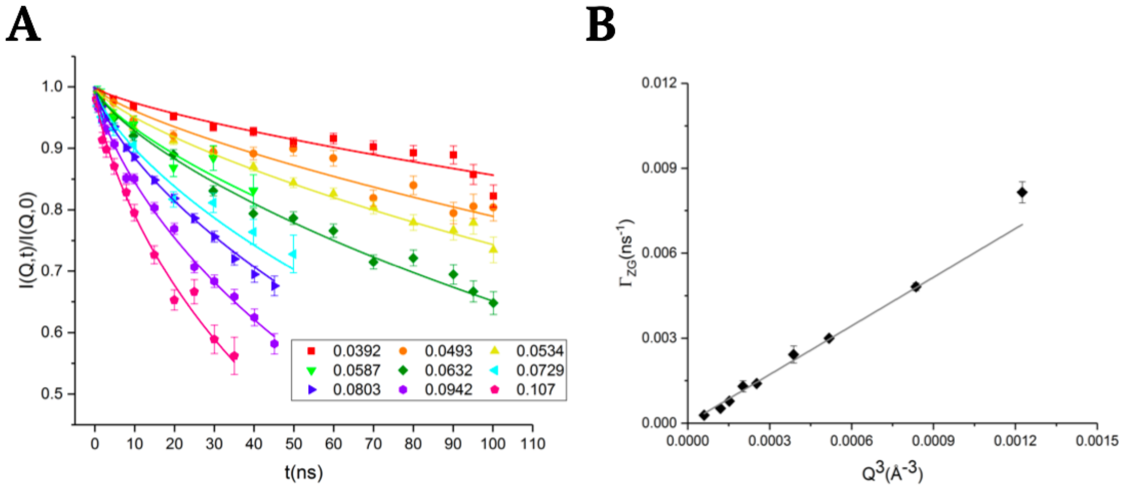

Figure B.2: The normalize intermediate scattering function $I(Q,t)/I(Q,0)$ measured by NSE (A) and the linear dependence of the relaxation rate (Γ_{ZG}) with respect to Q^3 (B) for the IMM mimic with 1.5 mol% PST. Error bars represent one standard deviation.

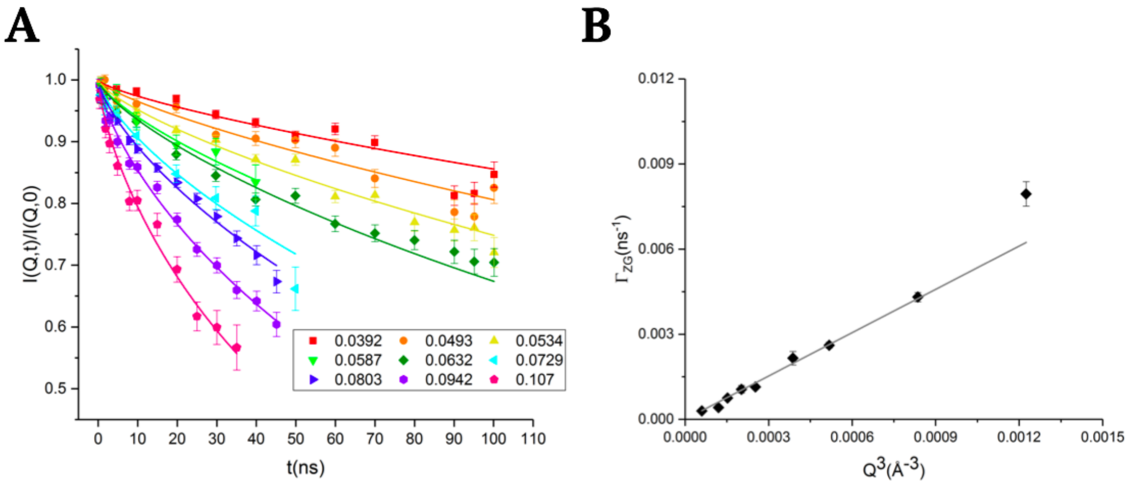

Figure B.3: The normalize intermediate scattering function $I(Q,t)/I(Q,0)$ measured by NSE (A) and the linear dependence of the relaxation rate (Γ_{ZG}) with respect to Q^3 (B) for the IMM mimic with 2 mol% PST. Error bars represent one standard deviation.

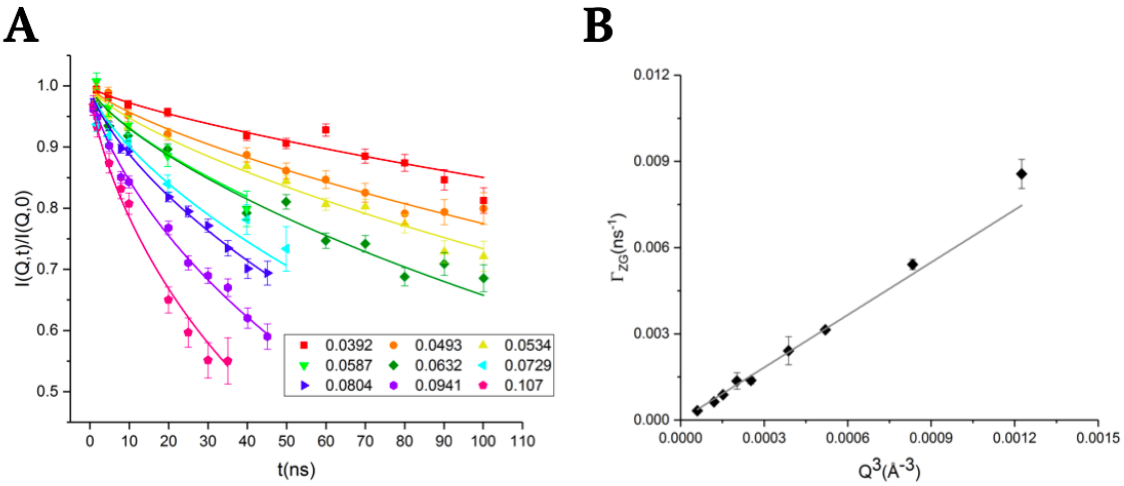

FIGURE B.4: The normalize intermediate scattering function $I(Q,t)/I(Q,0)$ measured by NSE (A) and the linear dependence of the relaxation rate (Γ_{ZG}) with respect to Q^3 (B) for the IMM mimic with 1 vol% DMSO-d6. Error bars represent one standard deviation.

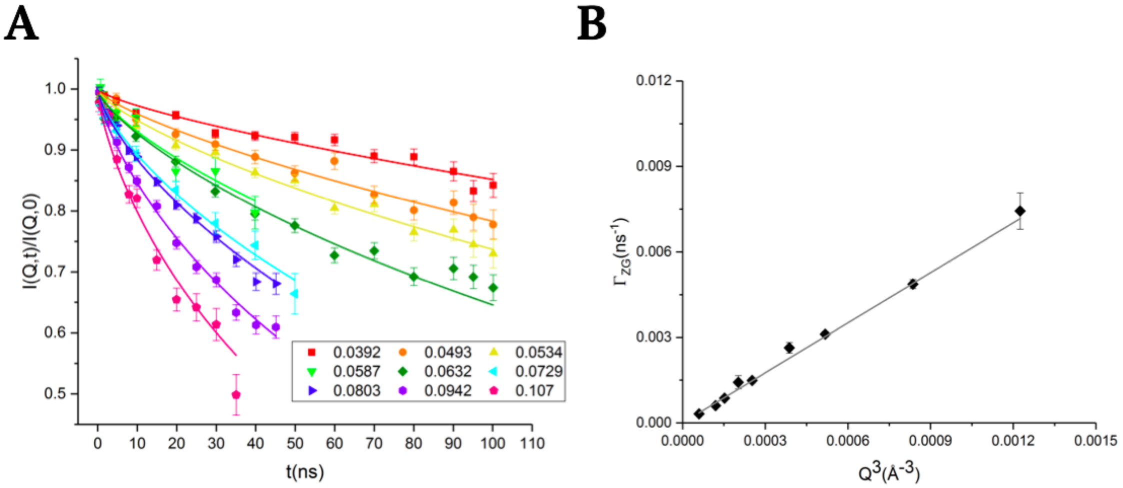

FIGURE B.5: The normalize intermediate scattering function $I(Q,t)/I(Q,0)$ measured by NSE (A) and the linear dependence of the relaxation rate (Γ_{ZG}) with respect to Q^3 (B) for the POPC/TOCL control. Error bars represent one standard deviation.

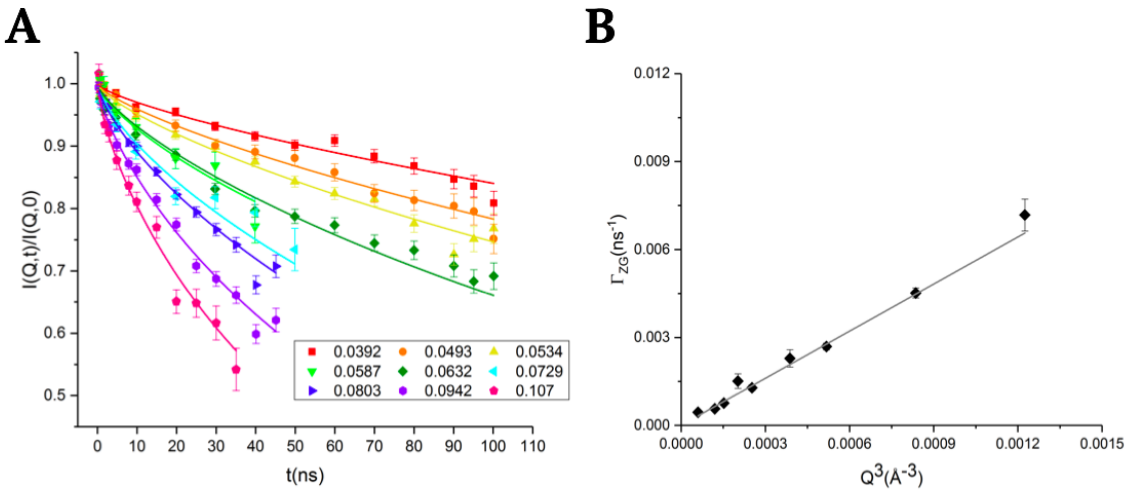

Figure B.6: The normalize intermediate scattering function $^{I(Q,t)}/_{I(Q,0)}$ measured by NSE (A) and the linear dependence of the relaxation rate (Γ_{ZG}) with respect to Q^3 (B) for the POPC/TOCL control with 1 mol% PST. Error bars represent one standard deviation.

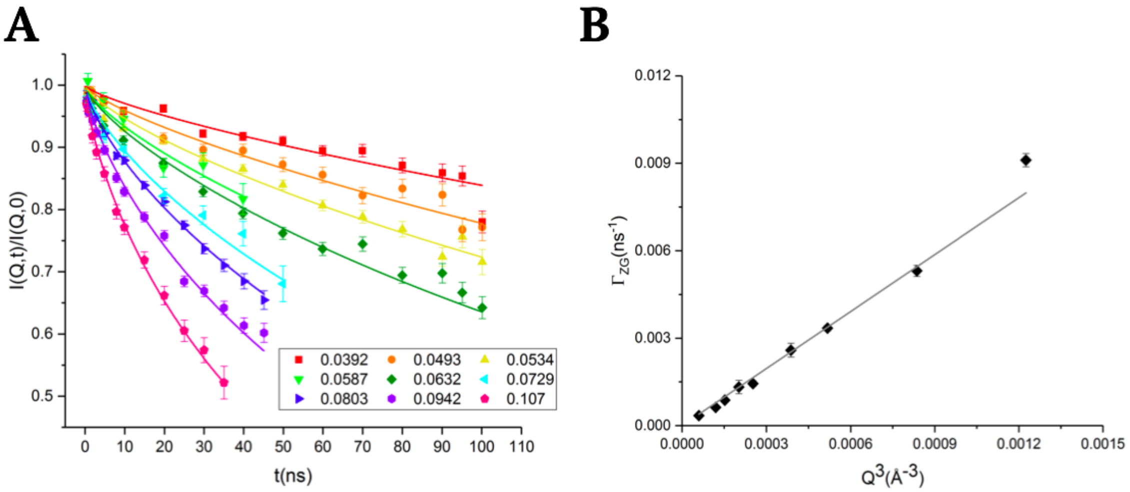

Figure B.7: The normalize intermediate scattering function $^{I(Q,t)}/_{I(Q,0)}$ measured by NSE (A) and the linear dependence of the relaxation rate (Γ_{ZG}) with respect to Q^3 (B) for the POPE/TOCL control. Error bars represent one standard deviation.

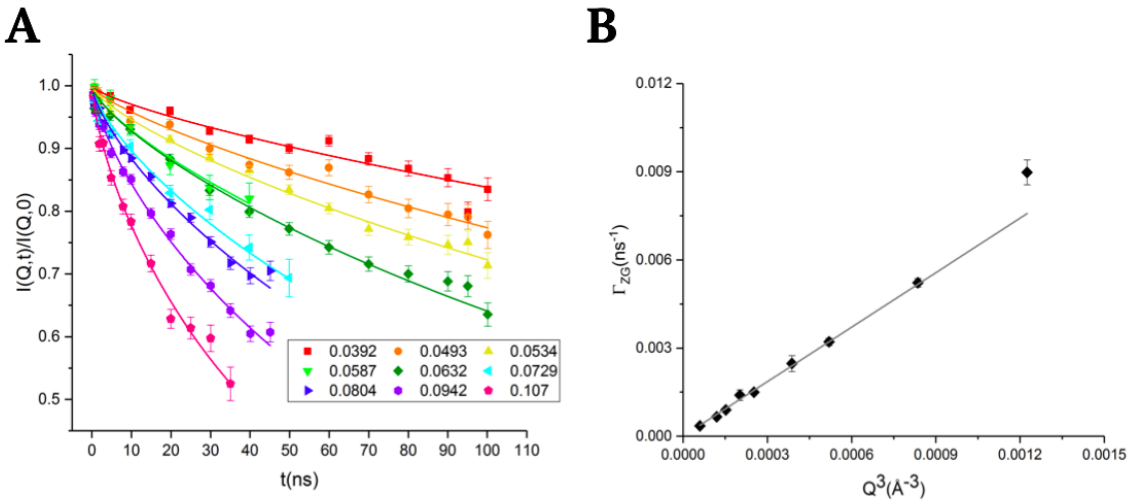

FIGURE B.8: The normalize intermediate scattering function $I(Q,t)/I(Q,0)$ measured by NSE (A) and the linear dependence of the relaxation rate (Γ_{ZG}) with respect to Q^3 (B) for the POPE/TOCL control with 1 mol% PST. Error bars represent one standard deviation.

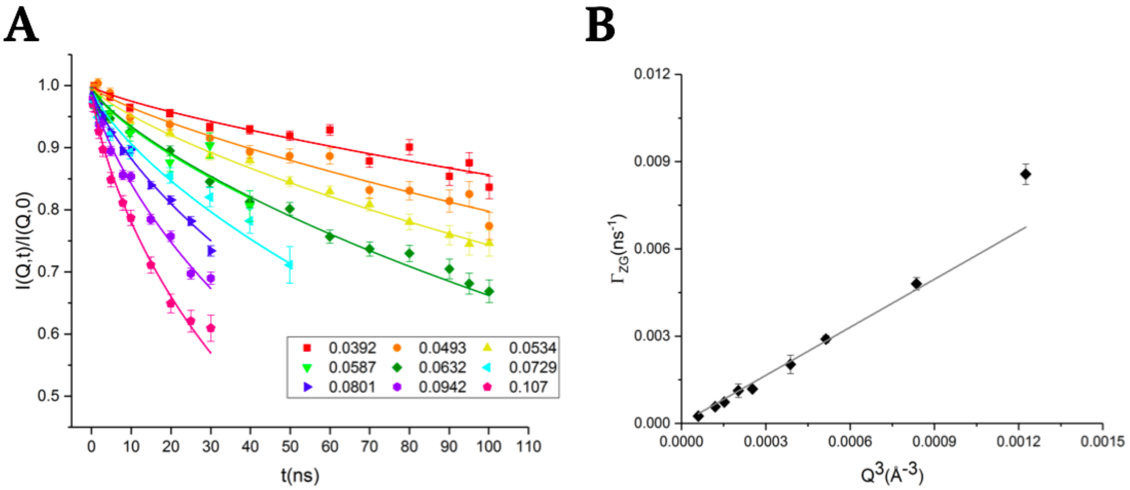

FIGURE B.9: The normalize intermediate scattering function $I(Q,t)/I(Q,0)$ measured by NSE (A) and the linear dependence of the relaxation rate (Γ_{ZG}) with respect to Q^3 (B) for the POPE/TOCL control with 2 mol% PST. Error bars represent one standard deviation.

Appendix C

Order Parameters

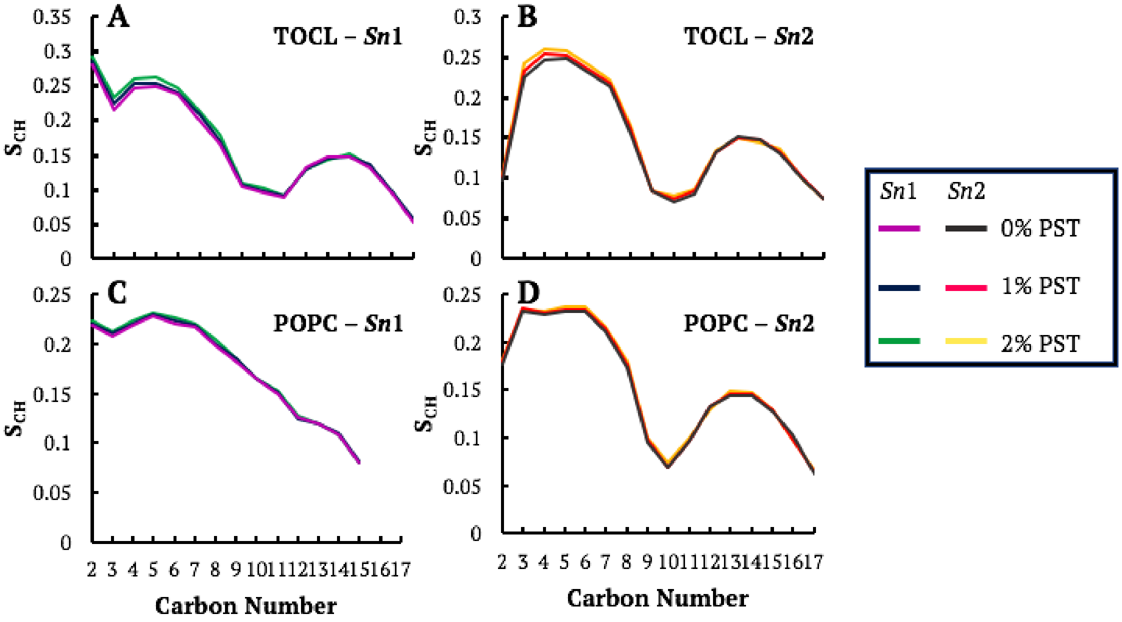

FIGURE C.1: Acyl chain order parameters extracted from MD simulations of the POPC/TOCL control with 0, 1, and 2 mol% PST. Order parameters (S_{CH}) throughout the length of the sn-1 (A and C) and sn-2 (B and D) acyl chains are shown for the lipids that compose the POPC/TOCL control: TOCL (A and B) and POPC (C and D).

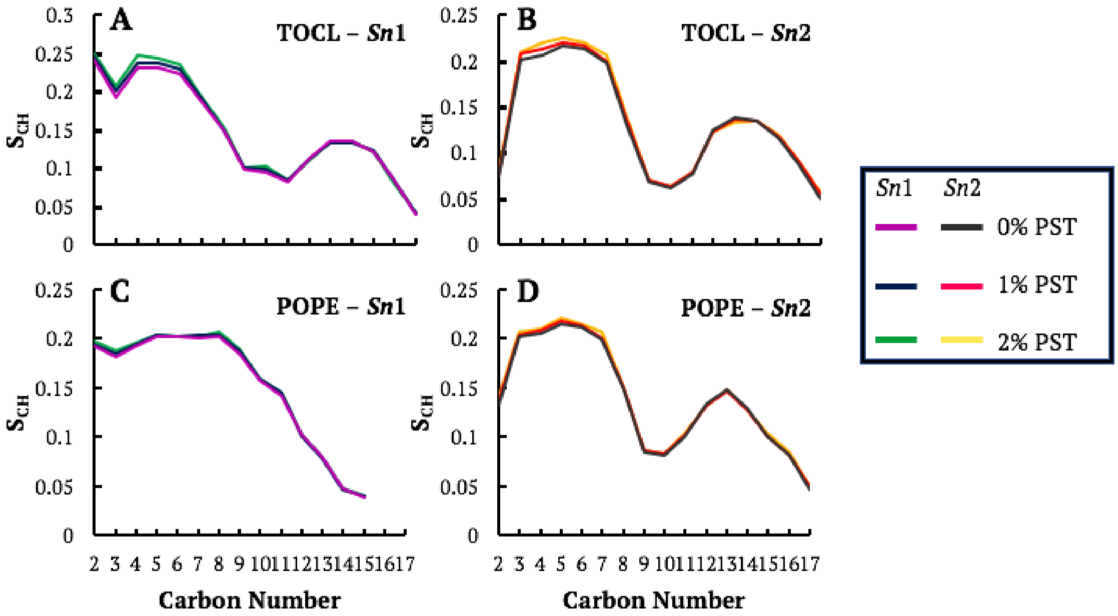

FIGURE C.2: Acyl chain order parameters extracted from MD simulations of the POPE/TOCL control with 0, 1, and 2 mol% PST. Order parameters (S_{CH}) throughout the length of the sn-1 (A and C) and sn-2 (B and D) acyl chains are shown for the lipids that compose the POPE/TOCL control: TOCL (A and B) and POPE (C and D).

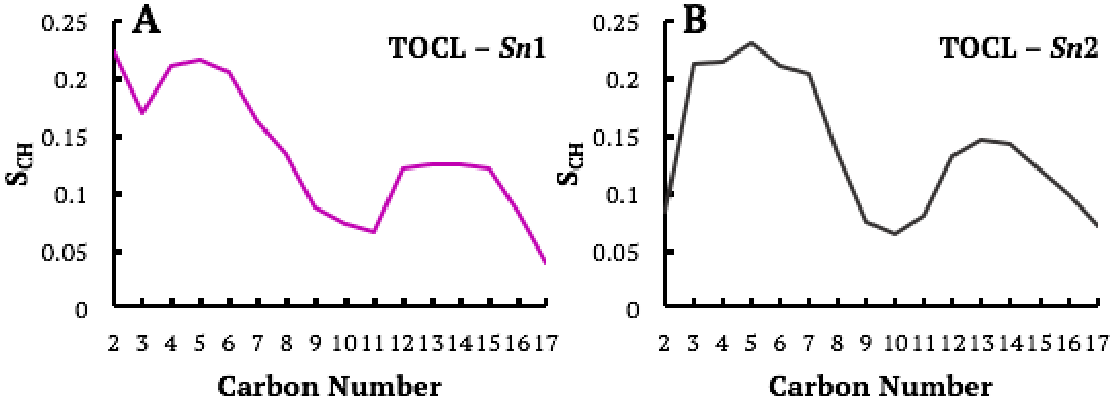

FIGURE C.3: Acyl chain order parameters extracted from MD simulations of the TOCL control. Order parameters (S_{CH}) throughout the length of the sn-1 (A) and sn-2 (B) acyl chains are shown.

Appendix D

PST Density Profiles

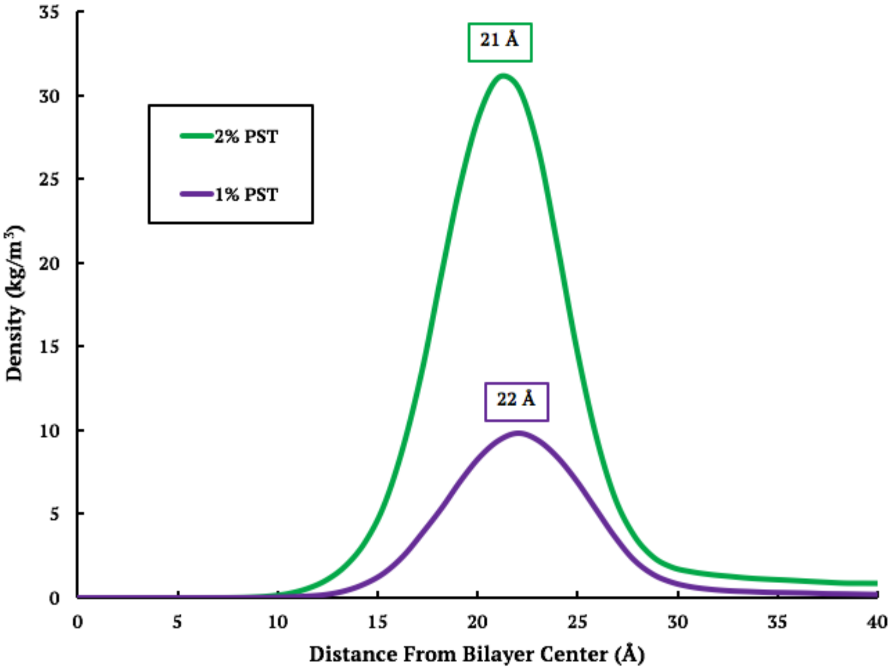

FIGURE D.1: PST density profiles extracted from MD runs of the POPC/TOCL bilayers in the presence of 1 and 2 mol% PST. The numbers inserted at the maximum amplitude of each curve correspond to the distance from bilayer center at which the maximum value occurs.

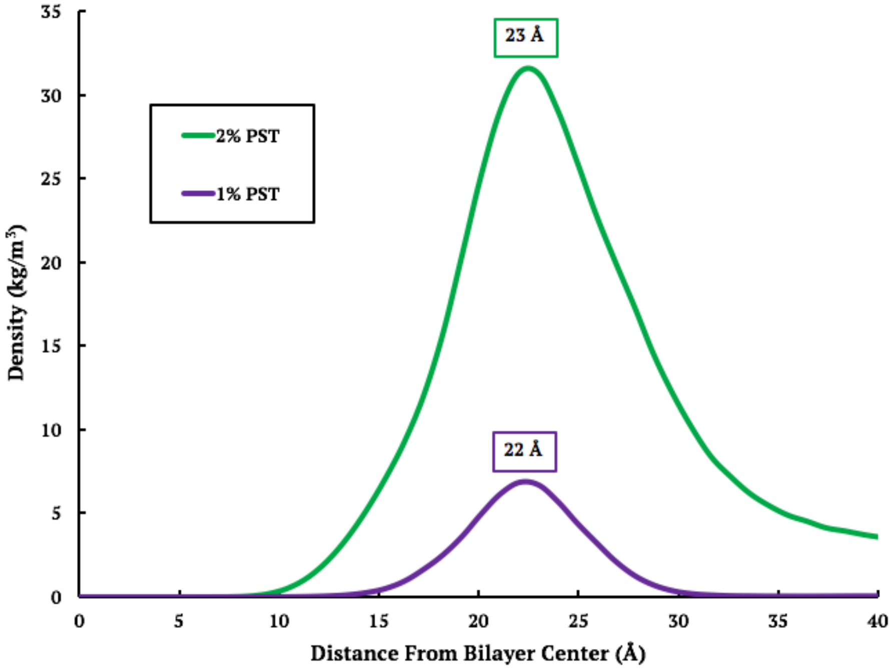

Figure D.2: PST density profiles extracted from MD runs of the POPE/TOCL bilayers in the presence of 1 and 2 mol% PST. The numbers inserted at the maximum amplitude of each curve correspond to the distance from bilayer center at which the maximum value occurs.

Appendix E

Radial Distribution Functions

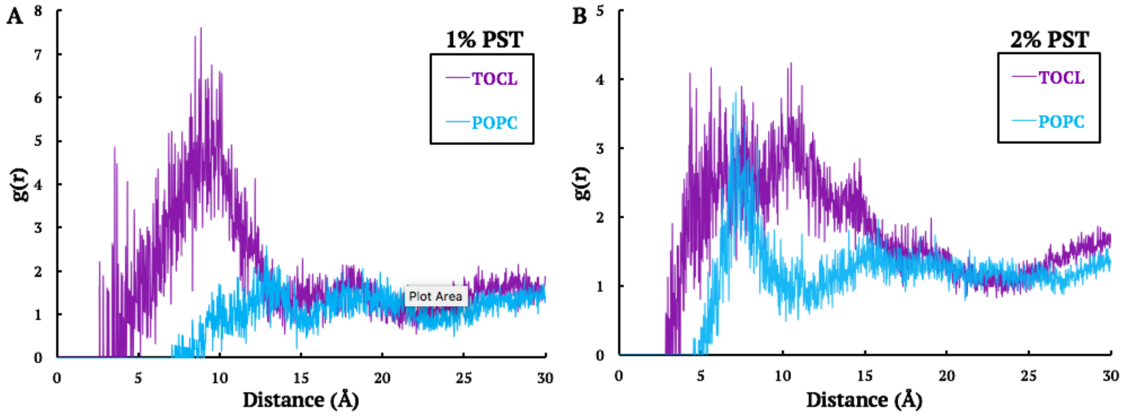

Figure E.1: RDF graphs for MD simulations corresponding to the POPC/TOCL control with 1 (A) and 2 (B) mol% PST.

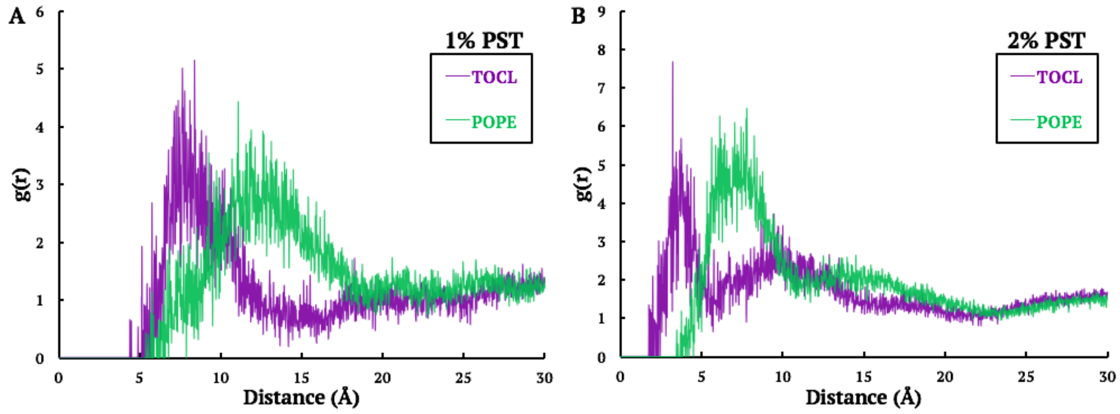

Figure E.2: RDF graphs for MD simulations corresponding to the POPE/TOCL control with 1 (A) and 2 (B) mol% PST.

Bibliography

[1] Allen Kaasik, Dzhamilja Safiulina, Alexander Zharkovsky, and Vladimir Veksler. Regulation of mitochondrial matrix volume. *American Journal of Physiology-Cell Physiology*, 292(1):C157–C163, January 2007. ISSN 0363-6143, 1522-1563. doi: 10.1152/ajpcell.00272.2006.

[2] C. Steenbergen, M. L. Hill, and R. B. Jennings. Volume regulation and plasma membrane injury in aerobic, anaerobic, and ischemic myocardium in vitro. Effects of osmotic cell swelling on plasma membrane integrity. *Circulation Research*, 57(6): 864–875, December 1985. ISSN 0009-7330, 1524-4571. doi: 10.1161/01.RES.57.6.864.

[3] Zachary T. Schug and Eyal Gottlieb. Cardiolipin acts as a mitochondrial signalling platform to launch apoptosis. *Biochimica et Biophysica Acta (BBA) - Biomembranes*, 1788(10):2022–2031, October 2009. ISSN 00052736. doi: 10.1016/j.bbamem.2009.05.004.

[4] Masakatsu Kawakami, Mariko Sekiguchi, Kazuki Sato, Shunji Kozaki, and Masami Takahashi. Erythropoietin Receptor-mediated Inhibition of Exocytotic Glutamate Release Confers Neuroprotection during Chemical Ischemia. *Journal of Biological Chemistry*, 276(42):39469–39475, October 2001. ISSN 0021-9258, 1083-351X. doi: 10.1074/jbc.M105832200.

[5] Elisa Barbieri, Pier Paolo Di Fiore, and Sara Sigismund. Endocytic control of signaling at the plasma membrane. *Current Opinion in Cell Biology*, 39:21–27, April 2016. ISSN 09550674. doi: 10.1016/j.ceb.2016.01.012.

[6] Norman F. Haard. Membrane Structure and Celular Death in Biological Tissue.

Journal of Food Science, 37(4):504–512, July 1972. ISSN 0022-1147, 1750-3841. doi: 10.1111/j.1365-2621.1972.tb02680.x.

[7] Anna L. Duncan, Alan J. Robinson, and John E. Walker. Cardiolipin binds selectively but transiently to conserved lysine residues in the rotor of metazoan ATP synthases. *Proceedings of the National Academy of Sciences*, 113(31):8687–8692, August 2016. ISSN 0027-8424, 1091-6490. doi: 10.1073/pnas.1608396113.

[8] Steven M. Claypool, Yavuz Oktay, Pinmanee Boontheung, Joseph A. Loo, and Carla M. Koehler. Cardiolipin defines the interactome of the major ADP/ATP carrier protein of the mitochondrial inner membrane. *Journal of Cell Biology*, 182(5): 937–950, September 2008. ISSN 1540-8140, 0021-9525. doi: 10.1083/jcb.200801152.

[9] Cláudia Brito, Didier Cabanes, Francisco Sarmento Mesquita, and Sandra Sousa. Mechanisms protecting host cells against bacterial pore-forming toxins. *Cellular and Molecular Life Sciences*, 76(7):1319–1339, April 2019. ISSN 1420-682X, 1420-9071. doi: 10.1007/s00018-018-2992-8.

[10] Ravi S. Shukla, Akshay Jain, Zhen Zhao, and Kun Cheng. Intracellular trafficking and exocytosis of a multi-component siRNA nanocomplex. *Nanomedicine: Nanotechnology, Biology and Medicine*, 12(5):1323–1334, July 2016. ISSN 15499634. doi: 10.1016/j.nano.2016.02.003.

[11] Jinxie Zhang, Xudong Zhang, Gan Liu, Danfeng Chang, Xin Liang, Xianbing Zhu, Wei Tao, and Lin Mei. Intracellular Trafficking Network of Protein Nanocapsules: Endocytosis, Exocytosis and Autophagy. *Theranostics*, 6(12):2099–2113, 2016. ISSN 1838-7640. doi: 10.7150/thno.16587.

[12] Jaime Santo-Domingo and Nicolas Demaurex. The renaissance of mitochondrial pH. *The Journal of General Physiology*, 139(6):415–423, June 2012. ISSN 1540-7748, 0022-1295. doi: 10.1085/jgp.201110767.

[13] Derek Marsh, Baladhandapani Shanmugavadivu, and Jörg H. Kleinschmidt. Membrane Elastic Fluctuations and the Insertion and Tilt of B-Barrel Proteins. *Biophysical Journal*, 91(1):227–232, July 2006. ISSN 00063495. doi: 10.1529/biophysj.105.079004.

[14] Olaf S. Andersen and Roger E. Koeppe. Bilayer Thickness and Membrane Protein Function: An Energetic Perspective. *Annual Review of Biophysics and Biomolecular Structure*, 36(1):107–130, June 2007. ISSN 1056-8700, 1545-4266.

[15] Rob Phillips, Tristan Ursell, Paul Wiggins, and Pierre Sens. Emerging roles for lipids in shaping membrane-protein function. *Nature*, 459(7245):379–385, May 2009. ISSN 0028-0836, 1476-4687. doi: 10.1038/nature08147.

[16] Alexander Jussupow, Andrea Di Luca, and Ville R. I. Kaila. How cardiolipin modulates the dynamics of respiratory complex I. *Science Advances*, 5(3):eaav1850, March 2019. ISSN 2375-2548. doi: 10.1126/sciadv.aav1850.

[17] Jianjun Pan, Xiaolin Cheng, Melissa Sharp, Chian-Sing Ho, Nawal Khadka, and John Katsaras. Structural and Mechanical Properties of Cardiolipin Lipid Bilayers Determined Using Neutron Spin Echo, Small Angle Neutron and X-ray Scattering, and Molecular Dynamics Simulations. page 26, 2015.

[18] A. Callan-Jones, B. Sorre, and P. Bassereau. Curvature-Driven Lipid Sorting in Biomembranes. *Cold Spring Harbor Perspectives in Biology*, 3(2):a004648–a004648, February 2011. ISSN 1943-0264. doi: 10.1101/cshperspect.a004648.

[19] Drew Marquardt, Frederick A. Heberle, Jianjun Pan, Xiaolin Cheng, Georg Pabst, Thad A. Harroun, Norbert Kučerka, and John Katsaras. The structures of polyunsaturated lipid bilayers by joint refinement of neutron and X-ray scattering data. *Chemistry and Physics of Lipids*, 229:104892, July 2020. ISSN 00093084.

[20] Michael Schlame and Mindong Ren. The role of cardiolipin in the structural organization of mitochondrial membranes. *Biochimica et Biophysica Acta (BBA) - Biomembranes*, 1788(10):2080–2083, October 2009. ISSN 00052736. doi: 10.1016/j.bbamem.2009.04.019.

[21] Stefan Semrau and Thomas Schmidt. Membrane heterogeneity – from lipid domains to curvature effects. *Soft Matter*, 5(17):3174, 2009. ISSN 1744-683X, 1744-6848. doi: 10.1039/b901587f.

[22] Kai Simons and Mathias J. Gerl. Revitalizing membrane rafts: new tools and insights.

Nature Reviews Molecular Cell Biology, 11(10):688–699, October 2010. ISSN 1471-0072, 1471-0080. doi: 10.1038/nrm2977.

[23] Brett W. Rickeard, Michael H. L. Nguyen, Mitchell DiPasquale, Caesar G. Yip, Hamilton Baker, Frederick A. Heberle, Xiaobing Zuo, Elizabeth G. Kelley, Michihiro Nagao, and Drew Marquardt. Transverse lipid organization dictates bending fluctuations in model plasma membranes. *Nanoscale*, page 10.1039.C9NR07977G, 2020. ISSN 2040-3364, 2040-3372. doi: 10.1039/C9NR07977G.

[24] Zheng Yi, Michihiro Nagao, and Dobrin P. Bossev. Effect of charged lidocaine on static and dynamic properties of model bio-membranes. *Biophysical Chemistry*, 160 (1):20–27, January 2012. ISSN 03014622. doi: 10.1016/j.bpc.2011.08.007.

[25] Drew Marquardt, Justin A. Williams, Norbert Kučerka, Jeffrey Atkinson, Stephen R. Wassall, John Katsaras, and Thad A. Harroun. Tocopherol Activity Correlates with Its Location in a Membrane: A New Perspective on the Antioxidant Vitamin E. *Journal of the American Chemical Society*, 135(20):7523–7533, May 2013. ISSN 0002-7863, 1520-5126. doi: 10.1021/ja312665r.

[26] Richard J. Alsop, Laura Toppozini, Drew Marquardt, Norbert Kučerka, Thad A. Harroun, and Maikel C. Rheinstädter. Aspirin inhibits formation of cholesterol rafts in fluid lipid membranes. *Biochimica et Biophysica Acta (BBA) - Biomembranes*, 1848(3):805–812, March 2015. ISSN 00052736. doi: 10.1016/j.bbamem.2014.11.023.

[27] Nawal K. Khadka, Xiaolin Cheng, Chian Sing Ho, John Katsaras, and Jianjun Pan. Interactions of the Anticancer Drug Tamoxifen with Lipid Membranes. *Biophysical Journal*, 108(10):2492–2501, May 2015. ISSN 00063495. doi: 10.1016/j.bpj.2015.04.010.

[28] Ana Catarina Alves, Daniela Ribeiro, Miguel Horta, José L. F. C. Lima, Cláudia Nunes, and Salette Reis. A biophysical approach to daunorubicin interaction with model membranes: relevance for the drug's biological activity. *Journal of The Royal Society Interface*, 14(133):20170408, August 2017. ISSN 1742-5689, 1742-5662. doi: 10.1098/rsif.2017.0408.

[29] Marc Eeman and Magali Deleu. From biological membranes to biomimetic model membranes. *Biotechnol. Agron. Soc. Environ.*, page 19, 2010.

[30] Michael H. L. Nguyen, B. W. Rickeard, M. DiPasquale, and D. Marquardt. Asymmetric Model Membranes: Frontiers and Challenges. In *Biomimetic Lipid Membranes: Fundamentals, Applications, and Commercialization*, pages 47–71. Springer, 2019.

[31] Hesham Moussa, Ana Martins, and Ghaleb Husseini. Review on Triggered Liposomal Drug Delivery with a Focus on Ultrasound. *Current Cancer Drug Targets*, 15(4): 282–313, May 2015. ISSN 15680096. doi: 10.2174/1568009615666150311100610.

[32] Drew Marquardt, Barbara Geier, and Georg Pabst. Asymmetric Lipid Membranes: Towards More Realistic Model Systems. *Membranes*, 5(2):180–196, May 2015. ISSN 2077-0375. doi: 10.3390/membranes5020180.

[33] A. Schwartz, H. Sugg, T. W. Ritter, and E. Fernandez-Repollet. Direct determination of cell diameter, surface area, and volume with an electronic volume sensing flow cytometer. *Cytometry*, 3(6):456–458, May 1983. ISSN 0196-4763, 1097-0320. doi: 10.1002/cyto.990030613.

[34] F. Nomura, M. Nagata, T. Inaba, H. Hiramatsu, H. Hotani, and K. Takiguchi. Capabilities of liposomes for topological transformation. *Proceedings of the National Academy of Sciences*, 98(5):2340–2345, February 2001. ISSN 0027-8424, 1091-6490. doi: 10.1073/pnas.041419098.

[35] A. McLachlan, N. Kekre, J. McNulty, and S. Pandey. Pancratistatin: A natural anti-cancer compound that targets mitochondria specifically in cancer cells to induce apoptosis. *Apoptosis*, 10(3):619–630, May 2005. ISSN 1360-8185, 1573-675X. doi: 10.1007/s10495-005-1896-x.

[36] Peter Siedlakowski, Amanda McLachlan-Burgess, Carly Griffin, Sridhar S. Tirumalai, James McNulty, and Siyaram Pandey. Synergy of pancratistatin and tamoxifen on breast cancer cells in inducing apoptosis by targeting mitochondria. *Cancer Biology & Therapy*, 7(3):376–384, March 2008. ISSN 1538-4047, 1555-8576. doi: 10.4161/cbt.7.3.5364.

[37] Carly Griffin, Siyaram Pandey, and James McNulty. Pancratistatin induces apoptosis and autophagy in metastatic prostate cancer cells. *International Journal of Oncology*, 38:1549–1556, March 2011. ISSN 1019-6439, 1791-2423. doi: 10.3892/ijo.2011.977.

[38] Carmen A. Mannella. Structure and dynamics of the mitochondrial inner membrane cristae. *Biochimica et Biophysica Acta (BBA) - Molecular Cell Research*, 1763(5-6): 542–548, May 2006. ISSN 01674889. doi: 10.1016/j.bbamcr.2006.04.006.

[39] Jane Comte, Bernard Maĭsterrena, and Daniéle C. Gautheron. Lipid composition and protein profiles of outer and inner membranes from pig heart mitochondria. Comparison with microsomes. *Biochimica et Biophysica Acta (BBA) - Biomembranes*, 419 (2):271–284, January 1976. ISSN 00052736. doi: 10.1016/0005-2736(76)90353-9.

[40] E Zinser, C D Sperka-Gottlieb, E V Fasch, S D Kohlwein, F Paltauf, and G Daum. Phospholipid synthesis and lipid composition of subcellular membranes in the unicellular eukaryote Saccharomyces cerevisiae. *Journal of Bacteriology*, 173(6):2026–2034, 1991. ISSN 0021-9193, 1098-5530. doi: 10.1128/JB.173.6.2026-2034.1991.

[41] G Daum and J. E. Vance. Import of lipids into mitochondria. *Progress in Lipid Research*, 36(2-3):103–130, 1997. doi: 10.1016/S0163-7827(97)00006-4.

[42] Susanne E. Horvath and Günther Daum. Lipids of mitochondria. *Progress in Lipid Research*, 52(4):590–614, October 2013. ISSN 01637827. doi: 10.1016/j.plipres.2013.07.002.

[43] Xinyuan Li, Pu Fang, Jietang Mai, Eric T Choi, Hong Wang, and Xiao-feng Yang. Targeting mitochondrial reactive oxygen species as novel therapy for inflammatory diseases and cancers. *Journal of Hematology & Oncology*, 6(1):19, 2013. ISSN 1756-8722. doi: 10.1186/1756-8722-6-19.

[44] Xinyuan Li, Pu Fang, William Y. Yang, Kylie Chan, Muriel Lavallee, Keman Xu, Tracy Gao, Hong Wang, and Xiaofeng Yang. Mitochondrial ROS, uncoupled from ATP synthesis, determine endothelial activation for both physiological recruitment of patrolling cells and pathological recruitment of inflammatory cells. *Canadian Journal of Physiology and Pharmacology*, 95(3):247–252, March 2017. ISSN 0008-4212, 1205-7541. doi: 10.1139/cjpp-2016-0515.

[45] Toren Finkel. Signal Transduction by Mitochondrial Oxidants. *Journal of Biological Chemistry*, 287(7):4434–4440, February 2012. ISSN 0021-9258, 1083-351X. doi: 10.1074/jbc.R111.271999.

[46] S. Maynard, S. H. Schurman, C. Harboe, N. C. de Souza-Pinto, and V. A. Bohr. Base excision repair of oxidative DNA damage and association with cancer and aging. *Carcinogenesis*, 30(1):2–10, September 2008. ISSN 0143-3334, 1460-2180. doi: 10.1093/carcin/bgn250.

[47] Jerry B. Lingrel and Theresa Kentzweiler. Na+, K+ - ATPase. *The Journal of Biological Chemistry*, 269(31):19659–19662, 1994.

[48] Paul D. Boyer. The ATP Synthase—A Splendid Molecular Machine. *Annual Review of Biochemistry*, 66(1):717–749, June 1997. ISSN 0066-4154, 1545-4509. doi: 10.1146/annurev.biochem.66.1.717.

[49] Kelvin Cain, Shawn B. Bratton, and Gerald M. Cohen. The Apaf-1 apoptosome: a large caspase-activating complex. *Biochimie*, 84(2-3):203–214, February 2002. ISSN 03009084. doi: 10.1016/S0300-9084(02)01376-7.

[50] José C. Fernández-Checa. Redox regulation and signaling lipids in mitochondrial apoptosis. *Biochemical and Biophysical Research Communications*, 304(3):471–479, May 2003. ISSN 0006291X. doi: 10.1016/S0006-291X(03)00619-3.

[51] M. R. Duchen. Roles of Mitochondria in Health and Disease. *Diabetes*, 53(Supplement 1):S96–S102, February 2004. ISSN 0012-1797, 1939-327X. doi: 10.2337/diabetes.53.2007.S96.

[52] Ljubava D. Zorova, Vasily A. Popkov, Egor Y. Plotnikov, Denis N. Silachev, Irina B. Pevzner, Stanislovas S. Jankauskas, Valentina A. Babenko, Savva D. Zorov, Anastasia V. Balakireva, Magdalena Juhaszova, Steven J. Sollott, and Dmitry B. Zorov. Mitochondrial membrane potential. *Analytical Biochemistry*, 552:50–59, July 2018. ISSN 00032697. doi: 10.1016/j.ab.2017.07.009.

[53] Gerrit van Meer, Dennis R. Voelker, and Gerald W. Feigenson. Membrane lipids: where they are and how they behave. *Nature Reviews Molecular Cell Biology*, 9(2):112–124, February 2008. ISSN 1471-0072, 1471-0080. doi: 10.1038/nrm2330.

[54] Manfred Fobker, Reinhard Voss, Holger Reinecke, Christina Crone, Gerd Assmann, and Michael Walter. Accumulation of cardiolipin and lysocardiolipin in fibroblasts from Tangier disease subjects. *FEBS Letters*, 500(3):157–162, July 2001. ISSN 00145793. doi: 10.1016/S0014-5793(01)02578-9.

[55] Michael Schlame, Richard I Kelley, Annette Feigenbaum, Jeffrey A Towbin, Paul M Heerdt, Thomas Schieble, Ronald J.A Wanders, Salvatore DiMauro, and Thomas J.J Blanck. Phospholipid abnormalities in children with Barth syndrome. *Journal of the American College of Cardiology*, 42(11):1994–1999, December 2003. ISSN 07351097. doi: 10.1016/j.jacc.2003.06.015.

[56] Adam J. Chicco and Genevieve C. Sparagna. Role of cardiolipin alterations in mitochondrial dysfunction and disease. *American Journal of Physiology-Cell Physiology*, 292(1):C33–C44, January 2007. ISSN 0363-6143, 1522-1563. doi: 10.1152/ajpcell.00243.2006.

[57] Jean LeCocq and Clinton E. Ballou. On the Structure of Cardiolipin. *Biochemistry*, 3(7):976–980, July 1964. ISSN 0006-2960, 1520-4995. doi: 10.1021/bi00895a023.

[58] Morris Kates, Jing-Yi Syz, David Gosser, and Thomas H. Haines. pH-dissociation characteristics of cardiolipin and its 2-deoxy analogue. *Lipids*, 28(10):877–882, October 1993. ISSN 0024-4201, 1558-9307. doi: 10.1007/BF02537494.

[59] Thomas H Haines and Norbert A Dencher. Cardiolipin: a proton trap for oxidative phosphorylation. *FEBS Letters*, 528(1-3):35–39, September 2002. ISSN 00145793. doi: 10.1016/S0014-5793(02)03292-1.

[60] M. Ott, J. D. Robertson, V. Gogvadze, B. Zhivotovsky, and S. Orrenius. Cytochrome c release from mitochondria proceeds by a two-step process. *Proceedings of the National Academy of Sciences*, 99(3):1259–1263, February 2002. ISSN 0027-8424, 1091-6490. doi: 10.1073/pnas.241655498.

[61] J. B. McMillin and William Dowhan. Cardiolipin and apoptosis. *Biochimica et Biophysica Acta*, 1585:97–107, 2002.

[62] G. Cevc and Derek Marsh. *Phospholipid bilayers: physical principles and models.* Wiley, 1987.

[63] Nikita Ikon and Robert O. Ryan. Cardiolipin and mitochondrial cristae organization. *Biochimica et Biophysica Acta (BBA) - Biomembranes*, 1859(6):1156–1163, June 2017. ISSN 00052736. doi: 10.1016/j.bbamem.2017.03.013.

[64] E. Mileykovskaya and W. Dowhan. Visualization of Phospholipid Domains in Escherichia coli by Using the Cardiolipin-Specific Fluorescent Dye 10-N-Nonyl Acridine Orange. *Journal of Bacteriology*, 182(4):1172–1175, February 2000. ISSN 0021-9193. doi: 10.1128/JB.182.4.1172-1175.2000.

[65] Kerwyn Casey Huang, Ranjan Mukhopadhyay, and Ned S Wingreen. A Curvature-Mediated Mechanism for Localization of Lipids to Bacterial Poles. *PLoS Computational Biology*, 2(11):8, 2006.

[66] R. N. A. H. Lewis and R. N. McElhaney. The physicochemical properties of cardiolipin bilayers and cardiolipin-containing lipid membranes. *Biochimica et Biophysica Acta*, page 11, 2009.

[67] Ruthven N.A.H. Lewis, Dagmar Zweytick, Georg Pabst, Karl Lohner, and Ronald N. McElhaney. Calorimetric, X-Ray Diffraction, and Spectroscopic Studies of the Thermotropic Phase Behavior and Organization of Tetramyristoyl Cardiolipin Membranes. *Biophysical Journal*, 92(9):3166–3177, May 2007. ISSN 00063495. doi: 10.1529/biophysj.106.094003.

[68] R. W. Ruddon. *Cancer biology.* Oxford University Press, 2007.

[69] Richard Doll and Richard Peto. The Causes of Cancer: Quantitative Estimates of Avoidable Risks of Cancer in the United States Today. 66:117, 1981.

[70] World Health Organization. Cancer, 2018. URL `https://www.who.int/news-room/fact-sheets/detail/cancer`.

[71] Canadian Cancer Society. Cancer statistics at a glance - Canadian Cancer Society, 2020. URL `https://www.cancer.ca/en/cancer-information/cancer-101/cancer-statistics-at-a-glance`.

[72] E Alirol and J C Martinou. Mitochondria and cancer: is there a morphological connection? *Oncogene*, 25(34):4706–4716, August 2006. ISSN 0950-9232, 1476-5594. doi: 10.1038/sj.onc.1209600.

[73] O. Warburg. On the Origin of Cancer Cells. *Science*, 123(3191):309–314, February 1956. ISSN 0036-8075, 1095-9203. doi: 10.1126/science.123.3191.309.

[74] Maarten W.N. Nijsten and Gooitzen M. van Dam. Hypothesis: Using the Warburg effect against cancer by reducing glucose and providing lactate. *Medical Hypotheses*, 73(1):48–51, July 2009. ISSN 03069877. doi: 10.1016/j.mehy.2009.01.041.

[75] Ralph J Deberardinis. Is cancer a disease of abnormal cellular metabolism? New angles on an old idea. *Genetics in Medicine*, 10(11):767–777, November 2008. ISSN 1098-3600, 1530-0366. doi: 10.1097/GIM.0b013e31818b0d9b.

[76] Josephine S. Modica-Napolitano and Keshav Singh. Mitochondria as targets for detection and treatment of cancer. *Expert Reviews in Molecular Medicine*, 4(9):1–19, April 2002. ISSN 1462-3994. doi: 10.1017/S1462399402004453.

[77] Jakub Rohlena, Lan-feng Dong, and Jiri Neuzil. Targeting the Mitochondrial Electron Transport Chain Complexes for the Induction of Apoptosis and Cancer Treatment. *Current Pharmaceutical Biotechnology*, 14(3):377–389, February 2013. ISSN 13892010. doi: 10.2174/1389201011314030011.

[78] Michelle Potter, Emma Newport, and Karl J. Morten. The Warburg effect: 80 years on. *Biochemical Society Transactions*, 44(5):1499–1505, October 2016. ISSN 0300-5127, 1470-8752. doi: 10.1042/BST20160094.

[79] Xiao Dong Xu, Shi Xiu Shao, Hai Ping Jiang, Yan Wei Cao, Yong Hua Wang, Xue Cheng Yang, You Lin Wang, Xin Sheng Wang, and Hai Tao Niu. Warburg Effect or Reverse Warburg Effect? A Review of Cancer Metabolism. *Oncology Research and Treatment*, 38(3):117–122, 2015. ISSN 2296-5270, 2296-5262. doi: 10.1159/000375435.

[80] B. P. Lieberman, K. Ploessl, L. Wang, W. Qu, Z. Zha, D. R. Wise, L. A. Chodosh, G. Belka, C. B. Thompson, and H. F. Kung. PET Imaging of Glutaminolysis in Tumors by 18F-(2S,4R)4-Fluoroglutamine. *Journal of Nuclear Medicine*, 52(12):1947–1955, December 2011. ISSN 0161-5505. doi: 10.2967/jnumed.111.093815.

[81] S. Weinhouse, O. Warburg, D. Burk, and A. L. Schade. On Respiratory Impairment in Cancer Cells. *Science*, 124(3215):267–272, August 1956. ISSN 0036-8075, 1095-9203. doi: 10.1126/science.124.3215.267.

[82] Young Seok Ju, Ludmil B Alexandrov, Moritz Gerstung, Inigo Martincorena, Serena Nik-Zainal, Manasa Ramakrishna, Helen R Davies, Elli Papaemmanuil, Gunes Gundem, Adam Shlien, Niccolo Bolli, Sam Behjati, Patrick S Tarpey, Jyoti Nangalia, Charles E Massie, Adam P Butler, Jon W Teague, George S Vassiliou, Anthony R Green, Ming-Qing Du, Ashwin Unnikrishnan, John E Pimanda, Bin Tean Teh, Nikhil Munshi, Mel Greaves, Paresh Vyas, Adel K El-Naggar, Tom Santarius, V Peter Collins, Richard Grundy, Jack A Taylor, D Neil Hayes, David Malkin, ICGC Breast Cancer Group, ICGC Chronic Myeloid Disorders Group, ICGC Prostate Cancer Group, Christopher S Foster, Anne Y Warren, Hayley C Whitaker, Daniel Brewer, Rosalind Eeles, Colin Cooper, David Neal, Tapio Visakorpi, William B Isaacs, G Steven Bova, Adrienne M Flanagan, P Andrew Futreal, Andy G Lynch, Patrick F Chinnery, Ultan McDermott, Michael R Stratton, and Peter J Campbell. Origins and functional consequences of somatic mitochondrial DNA mutations in human cancer. *eLife*, 3:e02935, October 2014. ISSN 2050-084X. doi: 10.7554/eLife.02935.

[83] Caroline Jose, Nadège Bellance, and Rodrigue Rossignol. Choosing between glycolysis and oxidative phosphorylation: A tumor's dilemma? *Biochimica et Biophysica Acta (BBA) - Bioenergetics*, 1807(6):552–561, June 2011. ISSN 00052728. doi: 10.1016/j.bbabio.2010.10.012.

[84] Rafael Moreno-Sánchez, Sara Rodríguez-Enríquez, Alvaro Marín-Hernández, and Emma Saavedra. Energy metabolism in tumor cells: Glycolytic and mitochondrial metabolism of tumor cells. *FEBS Journal*, 274(6):1393–1418, March 2007. ISSN 1742464X. doi: 10.1111/j.1742-4658.2007.05686.x.

[85] M Martin, B Beauvoit, P J Voisin, P Canioni, B Guerin, and M Rigoulet. Energetic and Morphological Plasticity of C6 Glioma Cells Grown on 3-D Support; Effect of Transient Glutamine Deprivation. *Journal of Bioenergetics and Biomembranes*, 30 (6):14, 1998.

[86] Emilie Obre and Rodrigue Rossignol. Emerging concepts in bioenergetics and cancer research: Metabolic flexibility, coupling, symbiosis, switch, oxidative tumors, metabolic remodeling, signaling and bioenergetic therapy. *The International Jour-*

nal of Biochemistry & Cell Biology, 59:167–181, February 2015. ISSN 13572725. doi: 10.1016/j.biocel.2014.12.008.

[87] Christopher Nguyen and Siyaram Pandey. Exploiting Mitochondrial Vulnerabilities to Trigger Apoptosis Selectively in Cancer Cells. *Cancers*, 11(7):916, June 2019. ISSN 2072-6694. doi: 10.3390/cancers11070916.

[88] Xin Lin Zu and Michael Guppy. Cancer metabolism: facts, fantasy, and fiction. *Biochemical and Biophysical Research Communications*, 313(3):459–465, January 2004. ISSN 0006291X. doi: 10.1016/j.bbrc.2003.11.136.

[89] Jorge Fernandez-de Cossio-Diaz and Alexei Vazquez. Limits of aerobic metabolism in cancer cells. *Scientific Reports*, 7(1):13488, December 2017. ISSN 2045-2322. doi: 10.1038/s41598-017-14071-y.

[90] Andrea Viale, Piergiorgio Pettazzoni, Costas A. Lyssiotis, Haoqiang Ying, Nora Sánchez, Matteo Marchesini, Alessandro Carugo, Tessa Green, Sahil Seth, Virginia Giuliani, Maria Kost-Alimova, Florian Muller, Simona Colla, Luigi Nezi, Giannicola Genovese, Angela K. Deem, Avnish Kapoor, Wantong Yao, Emanuela Brunetto, Ya'an Kang, Min Yuan, John M. Asara, Y. Alan Wang, Timothy P. Heffernan, Alec C. Kimmelman, Huamin Wang, Jason B. Fleming, Lewis C. Cantley, Ronald A. DePinho, and Giulio F. Draetta. Oncogene ablation-resistant pancreatic cancer cells depend on mitochondrial function. *Nature*, 514(7524):628–632, October 2014. ISSN 0028-0836, 1476-4687. doi: 10.1038/nature13611.

[91] Andrea Viale, Denise Corti, and Giulio F. Draetta. Tumors and Mitochondrial Respiration: A Neglected Connection. *Cancer Research*, 75(18):3687–3691, September 2015. ISSN 0008-5472, 1538-7445. doi: 10.1158/0008-5472.CAN-15-0491.

[92] Rakesh K. Jain, Lance L. Munn, and Dai Fukumura. Dissecting tumour pathophysiology using intravital microscopy. *Nature Reviews Cancer*, 2(4):266–276, April 2002. ISSN 1474-175X, 1474-1768. doi: 10.1038/nrc778.

[93] D. R. Green. The Pathophysiology of Mitochondrial Cell Death. *Science*, 305(5684): 626–629, July 2004. ISSN 0036-8075, 1095-9203. doi: 10.1126/science.1099320.

[94] Simone Fulda, Lorenzo Galluzzi, and Guido Kroemer. Targeting mitochondria for cancer therapy. *Nature Reviews Drug Discovery*, 9(6):447–464, June 2010. ISSN 1474-1776, 1474-1784. doi: 10.1038/nrd3137.

[95] Sonia C Dolfi, Leo Li-Ying Chan, Jean Qiu, Philip M Tedeschi, Joseph R Bertino, Kim M Hirshfield, Zoltán N Oltvai, and Alexei Vazquez. The metabolic demands of cancer cells are coupled to their size and protein synthesis rates. *Cancer & Metabolism*, 1(1):20, 2013. ISSN 2049-3002. doi: 10.1186/2049-3002-1-20.

[96] Antonio Evidente and Alexander Kornienko. Anticancer evaluation of structurally diverse Amaryllidaceae alkaloids and their synthetic derivatives. *Phytochemistry Reviews*, 8(2):449–459, June 2009. ISSN 1568-7767, 1572-980X. doi: 10.1007/s11101-008-9119-z.

[97] George R Pettit, Venkatswamy Gaddamidi, Gordon M Cragg, Delbert L Herald, and Yoneo Sagawa. Isolation and Structure of Pancratistatinl. *Journal of the Chemical Society, Chemical Communications*, pages 1693–1694, 1984.

[98] George R Pettit, Noeleen Melody, and Delbert L Herald. Antineoplastic Agents. 511. Direct Phosphorylation of Phenpanstatin and Pancratistatin. *Antineoplastic Agents*, 67:6, 2004.

[99] Natasha Kekre, Carly Griffin, James McNulty, and Siyaram Pandey. Pancratistatin causes early activation of caspase-3 and the flipping of phosphatidyl serine followed by rapid apoptosis specifically in human lymphoma cells. *Cancer Chemotherapy and Pharmacology*, 56(1):29–38, July 2005. ISSN 0344-5704, 1432-0843. doi: 10.1007/s00280-004-0941-8.

[100] Sudipa June Chatterjee, James McNulty, and Siyaram Pandey. Sensitization of human melanoma cells by tamoxifen to apoptosis induction by pancratistatin, a nongenotoxic natural compound:. *Melanoma Research*, 21(1):1–11, February 2011. ISSN 0960-8931. doi: 10.1097/CMR.0b013e328337abff.

[101] Carly Griffin, Caroline Hamm, James McNulty, and Siyaram Pandey. Pancratistatin induces apoptosis in clinical leukemia samples with minimal effect on non-cancerous peripheral blood mononuclear cells. *Cancer Cell International*, 10(6):7, 2010.

[102] C. Griffin, A. Karnik, J. McNulty, and S. Pandey. Pancratistatin Selectively Targets Cancer Cell Mitochondria and Reduces Growth of Human Colon Tumor Xenografts. *Molecular Cancer Therapeutics*, 10(1):57–68, January 2011. ISSN 1535-7163, 1538-8514. doi: 10.1158/1535-7163.MCT-10-0735.

[103] Dmitri I Svergun and Michel H J Koch. Small-angle scattering studies of biological macromolecules in solution. *Reports on Progress in Physics*, 66(10):1735–1782, October 2003. ISSN 0034-4885, 1361-6633. doi: 10.1088/0034-4885/66/10/R05.

[104] Michael R. Brzustowicz and Axel T. Brunger. X-ray scattering from unilamellar lipid vesicles. *Journal of Applied Crystallography*, 38(1):126–131, February 2005. ISSN 0021-8898. doi: 10.1107/S0021889804029206.

[105] J. Fitter, T. Gutberlet, and J. Katsaras, editors. *Neutron scattering in biology: techniques and applications*. Biological and medical physics, biomedical engineering. Springer, Berlin ; New York, 2006. ISBN 978-3-540-29108-4. OCLC: ocm63514223.

[106] G. Pabst, N. Kučerka, M.-P. Nieh, M.C. Rheinstädter, and J. Katsaras. Applications of neutron and X-ray scattering to the study of biologically relevant model membranes. *Chemistry and Physics of Lipids*, 163(6):460–479, June 2010. ISSN 00093084. doi: 10.1016/j.chemphyslip.2010.03.010.

[107] Georg Pabst, Norbert Kucerka, M.-P. Nieh, and John Katsaras. *Liposomes, Lipid Bilayers and Model Membranes: From Basic Research to Application*. CRC Press, 2014.

[108] W. Ruland. Small-angle scattering of two-phase systems: determination and significance of systematic deviations from Porod's law. *Journal of Applied Crystallography*, 4(1):70–73, February 1971. ISSN 0021-8898. doi: 10.1107/S0021889871006265.

[109] Cláudia Nunes, Gerald Brezesinski, José L. F. C. Lima, Salette Reis, and Marlene Lúcio. Synchrotron SAXS and WAXS Study of the Interactions of NSAIDs with Lipid Membranes. *The Journal of Physical Chemistry B*, 115(24):8024–8032, June 2011. ISSN 1520-6106, 1520-5207. doi: 10.1021/jp2025158.

[110] Mitsuhiro Hirai, Hiroki Iwase, Tomohiro Hayakawa, Masaharu Koizumi, and Hiroshi Takahashi. Determination of Asymmetric Structure of Ganglioside-DPPC Mixed Vesi-

cle Using SANS, SAXS, and DLS. *Biophysical Journal*, 85(3):1600–1610, September 2003. ISSN 00063495. doi: 10.1016/S0006-3495(03)74591-3.

[111] Jianjun Pan, Xiaolin Cheng, Luca Monticelli, Frederick A. Heberle, Norbert Kučerka, D. Peter Tieleman, and John Katsaras. The molecular structure of a phosphatidylserine bilayer determined by scattering and molecular dynamics simulations. *Soft Matter*, 10(21):3716, 2014. ISSN 1744-683X, 1744-6848. doi: 10.1039/c4sm00066h.

[112] Frederick A. Heberle, Drew Marquardt, Milka Doktorova, Barbara Geier, Robert F. Standaert, Peter Heftberger, Benjamin Kollmitzer, Jonathan D. Nickels, Robert A. Dick, Gerald W. Feigenson, John Katsaras, Erwin London, and Georg Pabst. Subnanometer Structure of an Asymmetric Model Membrane: Interleaflet Coupling Influences Domain Properties. *Langmuir*, 32(20):5195–5200, May 2016. ISSN 0743-7463, 1520-5827. doi: 10.1021/acs.langmuir.5b04562.

[113] M. Belička, F. Devínsky, and P. Balgavý. Neutrons in studies of phospholipid bilayers and bilayer–drug interaction. II. Small-angle scattering. *Acta Facultatis Pharmaceuticae Universitatis Comenianae*, 61(2):12–20, December 2014. ISSN 1338-6786. doi: 10.2478/afpuc-2014-0011.

[114] Elizabeth G. Kelley, Paul D. Butler, and Michihiro Nagao. Collective dynamics in model biological membranes measured bu nuetron spin echo. In *Characterization of Biological Membranes: Structure and Dynamics*, pages 131–176. Walter de Gruyter, Berlin, Boston, 2019.

[115] Svetlana Rajkumar Maurya, Deepti Chaturvedi, and Radhakrishnan Mahalakshmi. Modulating lipid dynamics and membrane fluidity to drive rapid folding of a transmembrane barrel. *Scientific Reports*, 3(1):1989, December 2013. ISSN 2045-2322. doi: 10.1038/srep01989.

[116] Michael Chvanov. Metabolic Control of Elastic Properties of the Inner Mitochondrial Membrane. *The Journal of Physical Chemistry B*, 110(45):22903–22909, November 2006. ISSN 1520-6106, 1520-5207. doi: 10.1021/jp0638181.

[117] J. Liu, M. Kaksonen, D. G. Drubin, and G. Oster. Endocytic vesicle scission by lipid

phase boundary forces. *Proceedings of the National Academy of Sciences*, 103(27): 10277–10282, July 2006. ISSN 0027-8424, 1091-6490. doi: 10.1073/pnas.0601045103.

[118] Jeanne C. Stachowiak, Frances M. Brodsky, and Elizabeth A. Miller. A cost–benefit analysis of the physical mechanisms of membrane curvature. *Nature Cell Biology*, 15 (9):1019–1027, September 2013. ISSN 1465-7392, 1476-4679. doi: 10.1038/ncb2832.

[119] Anne Pierres, Anne-Marie Benoliel, Dominique Touchard, and Pierre Bongrand. How Cells Tiptoe on Adhesive Surfaces before Sticking. *Biophysical Journal*, 94(10):4114–4122, May 2008. ISSN 00063495. doi: 10.1529/biophysj.107.125278.

[120] Arikta Biswas, Amal Alex, and Bidisha Sinha. Mapping Cell Membrane Fluctuations Reveals Their Active Regulation and Transient Heterogeneities. *Biophysical Journal*, 113(8):1768–1781, October 2017. ISSN 00063495. doi: 10.1016/j.bpj.2017.08.041.

[121] Simone Braig, B U Sebastian Schmidt, Katharina Stoiber, Chris Händel, Till Möhn, Oliver Werz, Rolf Müller, Stefan Zahler, Andreas Koeberle, Josef A Käs, and Angelika M Vollmar. Pharmacological targeting of membrane rigidity: implications on cancer cell migration and invasion. *New Journal of Physics*, 17(8):083007, August 2015. ISSN 1367-2630. doi: 10.1088/1367-2630/17/8/083007.

[122] Chris Händel, B U Sebastian Schmidt, Jürgen Schiller, Undine Dietrich, Till Möhn, Tobias R Kießling, Steve Pawlizak, Anatol W Fritsch, Lars-Christian Horn, Susanne Briest, Michael Höckel, Mareike Zink, and Josef A Käs. Cell membrane softening in human breast and cervical cancer cells. *New Journal of Physics*, 17(8):083008, August 2015. ISSN 1367-2630. doi: 10.1088/1367-2630/17/8/083008.

[123] Beate-Annette Brüning, Sylvain Prévost, Ralf Stehle, Roland Steitz, Peter Falus, Bela Farago, and Thomas Hellweg. Bilayer undulation dynamics in unilamellar phospholipid vesicles: Effect of temperature, cholesterol and trehalose. *Biochimica et Biophysica Acta (BBA) - Biomembranes*, 1838(10):2412–2419, October 2014. ISSN 00052736. doi: 10.1016/j.bbamem.2014.06.006.

[124] V. K. Sharma, M. Nagao, D. K. Rai, and E. Mamontov. Membrane softening by nonsteroidal anti-inflammatory drugs investigated by neutron spin echo. *Physical*

Chemistry Chemical Physics, 21(36):20211–20218, 2019. ISSN 1463-9076, 1463-9084. doi: 10.1039/C9CP03767E.

[125] B. R. Brooks, C. L. Brooks, A. D. Mackerell, L. Nilsson, R. J. Petrella, B. Roux, Y. Won, G. Archontis, C. Bartels, S. Boresch, A. Caflisch, L. Caves, Q. Cui, A. R. Dinner, M. Feig, S. Fischer, J. Gao, M. Hodoscek, W. Im, K. Kuczera, T. Lazaridis, J. Ma, V. Ovchinnikov, E. Paci, R. W. Pastor, C. B. Post, J. Z. Pu, M. Schaefer, B. Tidor, R. M. Venable, H. L. Woodcock, X. Wu, W. Yang, D. M. York, and M. Karplus. CHARMM: The biomolecular simulation program. *Journal of Computational Chemistry*, 30(10):1545–1614, July 2009. ISSN 01928651, 1096987X. doi: 10.1002/jcc.21287.

[126] Jeffery B. Klauda, Richard M. Venable, J. Alfredo Freites, Joseph W. O'Connor, Douglas J. Tobias, Carlos Mondragon-Ramirez, Igor Vorobyov, Alexander D. MacKerell, and Richard W. Pastor. Update of the CHARMM All-Atom Additive Force Field for Lipids: Validation on Six Lipid Types. *The Journal of Physical Chemistry B*, 114 (23):7830–7843, June 2010. ISSN 1520-6106, 1520-5207. doi: 10.1021/jp101759q.

[127] Sunhwan Jo, Taehoon Kim, and Wonpil Im. Automated Builder and Database of Protein/Membrane Complexes for Molecular Dynamics Simulations. *PLoS ONE*, 2 (9):e880, September 2007. ISSN 1932-6203. doi: 10.1371/journal.pone.0000880.

[128] Sunhwan Jo, Taehoon Kim, Vidyashankara G. Iyer, and Wonpil Im. CHARMM-GUI: A web-based graphical user interface for CHARMM. *Journal of Computational Chemistry*, 29(11):1859–1865, August 2008. ISSN 01928651. doi: 10.1002/jcc.20945.

[129] Sunhwan Jo, Joseph B. Lim, Jeffery B. Klauda, and Wonpil Im. CHARMM-GUI Membrane Builder for Mixed Bilayers and Its Application to Yeast Membranes. *Biophysical Journal*, 97(1):50–58, July 2009. ISSN 00063495. doi: 10.1016/j.bpj.2009.04.013.

[130] Emilia L. Wu, Xi Cheng, Sunhwan Jo, Huan Rui, Kevin C. Song, Eder M. Dávila-Contreras, Yifei Qi, Jumin Lee, Viviana Monje-Galvan, Richard M. Venable, Jeffery B. Klauda, and Wonpil Im. CHARMM-GUI *Membrane Builder* toward realistic biological membrane simulations. *Journal of Computational Chemistry*, 35(27):1997–2004, October 2014. ISSN 01928651. doi: 10.1002/jcc.23702.

[131] Jumin Lee, Xi Cheng, Jason M. Swails, Min Sun Yeom, Peter K. Eastman, Justin A. Lemkul, Shuai Wei, Joshua Buckner, Jong Cheol Jeong, Yifei Qi, Sunhwan Jo, Vijay S. Pande, David A. Case, Charles L. Brooks, Alexander D. MacKerell, Jeffery B. Klauda, and Wonpil Im. CHARMM-GUI Input Generator for NAMD, GROMACS, AMBER, OpenMM, and CHARMM/OpenMM Simulations Using the CHARMM36 Additive Force Field. *Journal of Chemical Theory and Computation*, 12(1):405–413, January 2016. ISSN 1549-9618, 1549-9626. doi: 10.1021/acs.jctc.5b00935.

[132] Martin Dahlberg. Polymorphic Phase Behavior of Cardiolipin Derivatives Studied by Coarse-Grained Molecular Dynamics. *The Journal of Physical Chemistry B*, 111(25): 7194–7200, June 2007. ISSN 1520-6106, 1520-5207. doi: 10.1021/jp071954f.

[133] Martin Dahlberg and Arnold Maliniak. Molecular Dynamics Simulations of Cardiolipin Bilayers. *The Journal of Physical Chemistry B*, 112(37):11655–11663, September 2008. ISSN 1520-6106, 1520-5207. doi: 10.1021/jp803414g.

[134] Tomasz Róg, Hector Martinez-Seara, Nana Munck, Matej Orešič, Mikko Karttunen, and Ilpo Vattulainen. Role of Cardiolipins in the Inner Mitochondrial Membrane: Insight Gained through Atom-Scale Simulations. *The Journal of Physical Chemistry B*, 113(11):3413–3422, March 2009. ISSN 1520-6106, 1520-5207. doi: 10.1021/jp8077369.

[135] Daniel Aguayo, Fernando D. González-Nilo, and Christophe Chipot. Insight into the Properties of Cardiolipin Containing Bilayers from Molecular Dynamics Simulations, Using a Hybrid All-Atom/United-Atom Force Field. *Journal of Chemical Theory and Computation*, 8(5):1765–1773, May 2012. ISSN 1549-9618, 1549-9626. doi: 10.1021/ct200849k.

[136] Kevin J. Boyd, Nathan N. Alder, and Eric R. May. Molecular Dynamics Analysis of Cardiolipin and Monolysocardiolipin on Bilayer Properties. *Biophysical Journal*, 114 (9):2116–2127, May 2018. ISSN 00063495. doi: 10.1016/j.bpj.2018.04.001.

[137] Richard M. Venable, Frank L.H. Brown, and Richard W. Pastor. Mechanical properties of lipid bilayers from molecular dynamics simulation. *Chemistry and Physics of Lipids*, 192:60–74, November 2015. ISSN 00093084. doi: 10.1016/j.chemphyslip.2015.07.014.

[138] M. Doktorova, D. Harries, and G. Khelashvili. Determination of bending rigidity and tilt modulus of lipid membranes from real-space fluctuation analysis of molecular dynamics simulations. *Physical Chemistry Chemical Physics*, 19(25):16806–16818, 2017. ISSN 1463-9076, 1463-9084. doi: 10.1039/C7CP01921A.

[139] M. Doktorova, M.V. LeVine, G. Khelashvili, and H. Weinstein. A new computational method for membrane compressibility: Bilayer mechanical thickness revisited. *Biophysical Journal*, 116(3):487–502, 2019. doi: 10.1101/360792.

[140] Ranjan Mukhopadhyay, Kerwyn Casey Huang, and Ned S. Wingreen. Lipid Localization in Bacterial Cells through Curvature-Mediated Microphase Separation. *Biophysical Journal*, 95(3):1034–1049, August 2008. ISSN 00063495. doi: 10.1529/biophysj.107.126920.

[141] C. Arnarez, S. J. Marrink, and X. Periole. Identification of cardiolipin binding sites on cytochrome c oxidase at the entrance of proton channels. *Scientific Reports*, 3(1): 1263, December 2013. ISSN 2045-2322. doi: 10.1038/srep01263.

[142] Thomas Lemmin, Christophe Bovigny, Diane Lançon, and Matteo Dal Peraro. Cardiolipin Models for Molecular Simulations of Bacterial and Mitochondrial Membranes. *Journal of Chemical Theory and Computation*, 9(1):670–678, January 2013. ISSN 1549-9618, 1549-9626. doi: 10.1021/ct300590v.

[143] Semen Yesylevskyy, Timothée Rivel, and Christophe Ramseyer. Curvature increases permeability of the plasma membrane for ions, water and the anti-cancer drugs cisplatin and gemcitabine. preprint, Biophysics, April 2019.

[144] Sumit Garg, Francisco Castro-Roman, Lionel Porcar, Paul Butler, Pedro Jesus Bautista, Natalie Krzyzanowski, and Ursula Perez-Salas. Cholesterol solubility limit in lipid membranes probed by small angle neutron scattering and MD simulations. *Soft Matter*, 10(46):9313–9317, 2014. ISSN 1744-683X, 1744-6848. doi: 10.1039/C4SM01219D.

[145] Drew Marquardt, Norbert Kučerka, Stephen R. Wassall, Thad A. Harroun, and John Katsaras. Cholesterol's location in lipid bilayers. *Chemistry and Physics of Lipids*, 199:17–25, September 2016. ISSN 00093084. doi: 10.1016/j.chemphyslip.2016.04.001.

[146] Norbert Kučerka, Bryan W. Holland, Chris G. Gray, Bruno Tomberli, and John Katsaras. Scattering Density Profile Model of POPG Bilayers As Determined by Molecular Dynamics Simulations and Small-Angle Neutron and X-ray Scattering Experiments. *The Journal of Physical Chemistry B*, 116(1):232–239, January 2012. ISSN 1520-6106, 1520-5207. doi: 10.1021/jp208920h.

[147] Michael Schlame and Dörte Otten. Analysis of cardiolipin molecular species by high-performance liquid chromatography of its derivative 1,3-bisphosphatidyl-2-benzoyl-sn-glycerol dimethyl ester. *Analytical Biochemistry*, 195(2):290–295, June 1991. ISSN 00032697. doi: 10.1016/0003-2697(91)90332-N.

[148] Michael Schlame, Mindong Ren, Yang Xu, Miriam L. Greenberg, and Ivan Haller. Molecular symmetry in mitochondrial cardiolipins. *Chemistry and Physics of Lipids*, 138(1-2):38–49, December 2005. ISSN 00093084. doi: 10.1016/j.chemphyslip.2005.08.002.

[149] Madhuri Manpadi and Alexander Kornienko. Total Syntheses of Pancratistatin. A Review. *Organic Preparations and Procedures International*, 40(2):107–161, April 2008. ISSN 0030-4948, 1945-5453. doi: 10.1080/00304940809458083.

[150] Zak E. Hughes, Alan E. Mark, and Ricardo L. Mancera. Molecular Dynamics Simulations of the Interactions of DMSO with DPPC and DOPC Phospholipid Membranes. *The Journal of Physical Chemistry B*, 116(39):11911–11923, October 2012. ISSN 1520-6106, 1520-5207. doi: 10.1021/jp3035538.

[151] C. J. Glinka, J. G. Barker, B. Hammouda, S. Krueger, J. J. Moyer, and W. J. Orts. The 30 m Small-Angle Neutron Scattering Instruments at the National Institute of Standards and Technology. *Journal of Applied Crystallography*, 31(3):430–445, June 1998. ISSN 00218898. doi: 10.1107/S0021889897017020.

[152] Steven R. Kline. Reduction and analysis of SANS and USANS data using IGOR Pro. *Journal of Applied Crystallography*, 39(6):895–900, December 2006. ISSN 0021-8898. doi: 10.1107/S0021889806035059.

[153] Aislyn Lewis-Laurent, Frederick A. Heberle, and Drew Marquardt. Vesicle Viewer, 2020. URL `https://www.vesicleviewer.dmarquardt.ca/`.

[154] N. Rosov, S. Rathgeber, and M. Monkenbusch. Neutron Spin Echo Spectroscopy at the NIST Center for Neutron Research. In Peggy Cebe, Benjamin S. Hsiao, and David J. Lohse, editors, *Scattering from Polymers*, volume 739, pages 103–116. American Chemical Society, Washington, DC, July 1999. ISBN 978-0-8412-3644-8 978-0-8412-1737-9. doi: 10.1021/bk-2000-0739.ch007. Series Title: ACS Symposium Series.

[155] Richard Tumanjong Azuah, Larry R. Kneller, Yiming Qiu, Philip L. W. Tregenna-Piggott, Craig M. Brown, John R. D. Copley, and Robert M. Dimeo. DAVE: A Comprehensive Software Suite for the Reduction, Visualization, and Analysis of Low Energy Neutron Spectroscopic Data. *Journal of Research of the National Institute of Standards and Technology*, 114(6):341, November 2009. ISSN 1044677X. doi: 10.6028/jres.114.025.

[156] H.J.C. Berendsen, D. van der Spoel, and R. van Drunen. GROMACS: A message-passing parallel molecular dynamics implementation. *Computer Physics Communications*, 91(1-3):43–56, September 1995. ISSN 00104655. doi: 10.1016/0010-4655(95)00042-E.

[157] H. J. C. Berendsen, J. P. M. Postma, W. F. van Gunsteren, A. DiNola, and J. R. Haak. Molecular dynamics with coupling to an external bath. *The Journal of Chemical Physics*, 81(8):3684–3690, October 1984. ISSN 0021-9606, 1089-7690. doi: 10.1063/1.448118.

[158] Giovanni Bussi, Davide Donadio, and Michele Parrinello. Canonical sampling through velocity rescaling. *The Journal of Chemical Physics*, 126(1):014101, January 2007. ISSN 0021-9606, 1089-7690. doi: 10.1063/1.2408420.

[159] M. Parrinello and A. Rahman. Polymorphic transitions in single crystals: A new molecular dynamics method. *Journal of Applied Physics*, 52(12):7182–7190, December 1981. ISSN 0021-8979, 1089-7550. doi: 10.1063/1.328693. URL `http://aip.scitation.org/doi/10.1063/1.328693`.

[160] William Humphrey, Andrew Dalke, and Klaus Schulten. VMD: Visual Molecular Dynamics. *Journal of Molecular Graphics*, 14:33–38, 1996.

[161] Frederick A. Heberle, Jianjun Pan, Robert F. Standaert, Paul Drazba, Norbert

Kučerka, and John Katsaras. Model-based approaches for the determination of lipid bilayer structure from small-angle neutron and X-ray scattering data. *European Biophysics Journal*, 41(10):875–890, October 2012. ISSN 0175-7571, 1432-1017. doi: 10.1007/s00249-012-0817-5.

[162] Norbert Kučerka, Frederick Heberle, Jianjun Pan, and John Katsaras. Structural Significance of Lipid Diversity as Studied by Small Angle Neutron and X-ray Scattering. *Membranes*, 5(3):454–472, September 2015. ISSN 2077-0375. doi: 10.3390/membranes5030454.

[163] Norbert Kučerka, John F. Nagle, Jonathan N. Sachs, Scott E. Feller, Jeremy Pencer, Andrew Jackson, and John Katsaras. Lipid Bilayer Structure Determined by the Simultaneous Analysis of Neutron and X-Ray Scattering Data. *Biophysical Journal*, 95(5):2356–2367, September 2008. ISSN 00063495. doi: 10.1529/biophysj.108.132662.

[164] John F. Nagle and Stephanie Tristram-Nagle. Structure of lipid bilayers. *Biochimica et Biophysica Acta (BBA) - Reviews on Biomembranes*, 1469(3):159–195, November 2000. ISSN 03044157. doi: 10.1016/S0304-4157(00)00016-2.

[165] Paul A. Hyslop, Benoit Morel, and Richard D. Sauerheber. Organization and interaction of cholesterol and phosphatidylcholine in model bilayer membranes. *Biochemistry*, 29(4):1025–1038, January 1990. ISSN 0006-2960, 1520-4995. doi: 10.1021/bi00456a027.

[166] A. G. Zilman and R. Granek. Undulations and Dynamic Structure Factor of Membranes. *Physical Review Letters*, 77(23):4788–4791, December 1996. ISSN 0031-9007, 1079-7114. doi: 10.1103/PhysRevLett.77.4788.

[167] Ingo Hoffmann, Raphael Michel, Melissa Sharp, Olaf Holderer, Marie-Sousai Appavou, Frank Polzer, Bela Farago, and Michael Gradzielski. Softening of phospholipid membranes by the adhesion of silica nanoparticles – as seen by neutron spin-echo (NSE). *Nanoscale*, 6(12):6945–6952, 2014. ISSN 2040-3364, 2040-3372. doi: 10.1039/C4NR00774C.

[168] U Seifert and S. A Langer. Viscous Modes of Fluid Bilayer Membranes. *Europhysics*

Letters (EPL), 23(1):71–76, July 1993. ISSN 0295-5075, 1286-4854. doi: 10.1209/0295-5075/23/1/012.

[169] Max C. Watson and Frank L.H. Brown. Interpreting Membrane Scattering Experiments at the Mesoscale: The Contribution of Dissipation within the Bilayer. *Biophysical Journal*, 98(6):L9–L11, March 2010. ISSN 00063495. doi: 10.1016/j.bpj.2009.11.026.

[170] Michihiro Nagao, Elizabeth G. Kelley, Rana Ashkar, Robert Bradbury, and Paul D. Butler. Probing Elastic and Viscous Properties of Phospholipid Bilayers Using Neutron Spin Echo Spectroscopy. *The Journal of Physical Chemistry Letters*, 8(19): 4679–4684, October 2017. ISSN 1948-7185. doi: 10.1021/acs.jpclett.7b01830.

[171] Norbert Kučerka, Stephanie Tristram-Nagle, and John F. Nagle. Structure of Fully Hydrated Fluid Phase Lipid Bilayers with Monounsaturated Chains. *Journal of Membrane Biology*, 208(3):193–202, January 2006. ISSN 0022-2631, 1432-1424. doi: 10.1007/s00232-005-7006-8.

[172] Laura R. Arriaga, Iván López-Montero, Francisco Monroy, Guillermo Orts-Gil, Bela Farago, and Thomas Hellweg. Stiffening Effect of Cholesterol on Disordered Lipid Phases: A Combined Neutron Spin Echo + Dynamic Light Scattering Analysis of the Bending Elasticity of Large Unilamellar Vesicles. *Biophysical Journal*, 96(9):3629–3637, May 2009. ISSN 00063495. doi: 10.1016/j.bpj.2009.01.045.

[173] Alexander L. Boscia, Bradley W. Treece, Dariush Mohammadyani, Judith Klein-Seetharaman, Anthony R. Braun, Tsjerk A. Wassenaar, Beate Klösgen, and Stephanie Tristram-Nagle. X-ray structure, thermodynamics, elastic properties and MD simulations of cardiolipin/dimyristoylphosphatidylcholine mixed membranes. *Chemistry and Physics of Lipids*, 178:1–10, February 2014. ISSN 00093084. doi: 10.1016/j.chemphyslip.2013.12.010.

[174] Òscar Domènech, Lorena Redondo, Laura Picas, Antoni Morros, M. Teresa Montero, and Jordi Hernández-Borrell. Atomic force microscopy characterization of supported planar bilayers that mimic the mitochondrial inner membrane. *Journal of Molecular Recognition*, 20(6):546–553, November 2007. ISSN 09523499, 10991352. doi: 10.1002/jmr.849.

[175] S. Lupi, A. Perla, P. Maselli, F. Bordi, and S. Sennato. Infrared spectra of phosphatidylethanolamine–cardiolipin binary system. *Colloids and Surfaces B: Biointerfaces*, 64(1):56–64, June 2008. ISSN 09277765. doi: 10.1016/j.colsurfb.2008.01.007.

[176] Òscar Domènech, Antoni Morros, Miquel E. Cabañas, M. Teresa Montero, and Jordi Hernández-Borrell. Thermal response of domains in cardiolipin content bilayers. *Ultramicroscopy*, 107(10-11):943–947, October 2007. ISSN 03043991. doi: 10.1016/j.ultramic.2007.04.009.

[177] S. Sennato, F. Bordi, C. Cametti, C. Coluzza, A. Desideri, and S. Rufini. Evidence of Domain Formation in CardiolipinGlycerophospholipid Mixed Monolayers. A Thermodynamic and AFM Study. *The Journal of Physical Chemistry B*, 109(33):15950–15957, August 2005. ISSN 1520-6106, 1520-5207. doi: 10.1021/jp051893q.

[178] Kouji Matsumoto, Jin Kusaka, Ayako Nishibori, and Hiroshi Hara. Lipid domains in bacterial membranes. *Molecular Microbiology*, 61(5):1110–1117, September 2006. ISSN 0950-382X, 1365-2958. doi: 10.1111/j.1365-2958.2006.05317.x.

[179] Pentti Somerharju, Jorma A Virtanen, and Kwan Hon Cheng. Lateral organisation of membrane lipids The superlattice view. *Biochimica et Biophysica Acta*, 1440:17, 1999.

[180] Erick J. Dufourc. Sterols and membrane dynamics. *Journal of Chemical Biology*, 1(1-4):63–77, November 2008. ISSN 1864-6158, 1864-6166. doi: 10.1007/s12154-008-0010-6.

[181] Amadeu K. Sum, Roland Faller, and Juan J. de Pablo. Molecular Simulation Study of Phospholipid Bilayers and Insights of the Interactions with Disaccharides. *Biophysical Journal*, 85(5):2830–2844, November 2003. ISSN 00063495. doi: 10.1016/S0006-3495(03)74706-7.

[182] Jeffrey Barry, Michelle Fritz, Jeffrey R. Brender, Pieter E. S. Smith, Dong-Kuk Lee, and Ayyalusamy Ramamoorthy. Determining the Effects of Lipophilic Drugs on Membrane Structure by Solid-State NMR Spectroscopy: The Case of the Antioxidant Curcumin. *Journal of the American Chemical Society*, 131(12):4490–4498, April 2009. ISSN 0002-7863, 1520-5126. doi: 10.1021/ja809217u.

[183] Louic S. Vermeer, Bert L. de Groot, Valérie Réat, Alain Milon, and Jerzy Czaplicki. Acyl chain order parameter profiles in phospholipid bilayers: computation from molecular dynamics simulations and comparison with 2H NMR experiments. *European Biophysics Journal*, 36(8):919–931, November 2007. ISSN 0175-7571, 1432-1017. doi: 10.1007/s00249-007-0192-9.

[184] Tiago Mendes Ferreira, Filipe Coreta-Gomes, O. H. Samuli Ollila, Maria João Moreno, Winchil L. C. Vaz, and Daniel Topgaard. Cholesterol and POPC segmental order parameters in lipid membranes: solid state ^{1} H– ^{13} C NMR and MD simulation studies. *Phys. Chem. Chem. Phys.*, 15(6):1976–1989, 2013. ISSN 1463-9076, 1463-9084. doi: 10.1039/C2CP42738A.

[185] Kristyna Pluhackova, Sonja A. Kirsch, Jing Han, Liping Sun, Zhenyan Jiang, Tobias Unruh, and Rainer A. Böckmann. A Critical Comparison of Biomembrane Force Fields: Structure and Dynamics of Model DMPC, POPC, and POPE Bilayers. *The Journal of Physical Chemistry B*, 120(16):3888–3903, April 2016. ISSN 1520-6106, 1520-5207. doi: 10.1021/acs.jpcb.6b01870.

[186] Kunal R. Pandit and Jeffery B. Klauda. Membrane models of E. coli containing cyclic moieties in the aliphatic lipid chain. *Biochimica et Biophysica Acta (BBA) - Biomembranes*, 1818(5):1205–1210, May 2012. ISSN 00052736. doi: 10.1016/j.bbamem.2012.01.009.

[187] Shani Ben-Zichri, Sofiya Kolusheva, Michael Danilenko, Saniya Ossikbayeva, William J. Stabbert, Juan L. Poggio, David E. Stein, Zulfiya Orynbayeva, and Raz Jelinek. Cardiolipin mediates curcumin interactions with mitochondrial membranes. *Biochimica et Biophysica Acta (BBA) - Biomembranes*, 1861(1):75–82, January 2019. ISSN 00052736. doi: 10.1016/j.bbamem.2018.10.016.

[188] W. Caetano, M. Ferreira, M. Tabak, M.I. Mosquera Sanchez, O.N. Oliveira, P. Krüger, M. Schalke, and M. Lösche. Cooperativity of phospholipid reorganization upon interaction of dipyridamole with surface monolayers on water. *Biophysical Chemistry*, 91 (1):21–35, June 2001. ISSN 03014622. doi: 10.1016/S0301-4622(01)00145-4.

[189] André C. Machado and Luciano Caseli. Interaction of nitrofurantoin with lipid langmuir monolayers as cellular membrane models distinguished with tensiometry and in-

frared spectroscopy. *Colloids and Surfaces B: Biointerfaces*, 188:110794, April 2020. ISSN 09277765. doi: 10.1016/j.colsurfb.2020.110794.

[190] Luiz Fernando Grosso Salis, Guilherme Nuñez Jaroque, Jhon Fernando Berrío Escobar, Cristiano Giordani, Alejandro Martinez Martinez, Diana Margarita Márquez Fernández, Francesco Castelli, Maria Grazia Sarpietro, and Luciano Caseli. Interaction of 3,4,6-trimyristoyl-uridine derivative as potential anticancer drug with phospholipids of tumorigenic and non-tumorigenic cells. *Applied Surface Science*, 426: 77–86, December 2017. ISSN 01694332. doi: 10.1016/j.apsusc.2017.07.094.

[191] Wei-Chin Hung, Ming-Tao Lee, Fang-Yu Chen, and Huey W. Huang. The Condensing Effect of Cholesterol in Lipid Bilayers. *Biophysical Journal*, 92(11):3960–3967, June 2007. ISSN 00063495. doi: 10.1529/biophysj.106.099234.

[192] Barmak Mostofian, Quentin R. Johnson, Jeremy C. Smith, and Xiaolin Cheng. Carotenoids promote lateral packing and condensation of lipid membranes. *Physical Chemistry Chemical Physics*, 22(21):12281–12293, 2020. ISSN 1463-9076, 1463-9084. doi: 10.1039/D0CP01031F.

[193] Kevin J. Boyd, Nathan N. Alder, and Eric R. May. Buckling Under Pressure: Curvature-Based Lipid Segregation and Stability Modulation in Cardiolipin-Containing Bilayers. *Langmuir*, 33(27):6937–6946, July 2017. ISSN 0743-7463, 1520-5827. doi: 10.1021/acs.langmuir.7b01185.

[194] Mitchell DiPasquale, Michael H.L. Nguyen, Brett W. Rickeard, Nicole Cesca, Christopher Tannous, Stuart R. Castillo, John Katsaras, Elizabeth G. Kelley, Frederick A. Heberle, and Drew Marquardt. The antioxidant vitamin E as a membrane raft modulator: Tocopherols do not abolish lipid domains. *Biochimica et Biophysica Acta (BBA) - Biomembranes*, 1862(8):183189, August 2020. ISSN 00052736. doi: 10.1016/j.bbamem.2020.183189.

[195] Fumitaka Kawai, Momoko Shoda, Rie Harashima, Yoshito Sadaie, Hiroshi Hara, and Kouji Matsumoto. Cardiolipin Domains in Bacillus subtilis Marburg Membranes. *Journal of Bacteriology*, 186(5):1475–1483, March 2004. ISSN 0021-9193, 1098-5530. doi: 10.1128/JB.186.5.1475-1483.2004.

[196] Jonathan D. Nickels, Xiaolin Cheng, Barmak Mostofian, Christopher Stanley, Benjamin Lindner, Frederick A. Heberle, Stefania Perticaroli, Mikhail Feygenson, Takeshi Egami, Robert F. Standaert, Jeremy C. Smith, Dean A. A. Myles, Michael Ohl, and John Katsaras. Mechanical Properties of Nanoscopic Lipid Domains. *Journal of the American Chemical Society*, 137(50):15772–15780, December 2015. ISSN 0002-7863, 1520-5126. doi: 10.1021/jacs.5b08894.

[197] Marjatta Rytomaa and Pekka Mustonen. Reversible, Nonionic, and pH-dependent Association of Cytochrome c with Cardiolipin-Phosphatidylcholine Liposomes. *Journal of Biological Chemistry*, 267(31):6, 1992.

[198] Marjatta Rytomaa and Paavo K. J. Kinnunen. Evidence for Two Distinct Acidic Phospholipid-bindinSgites in Cytochrome c. *Journal of Biological Chemistry*, 269(3):5, 1994.

[199] Michael Schlame, Diego Rua, and Miriam L Greenberg. The biosynthesis and functional role of cardiolipin. *Progress in Lipid Research*, 39(3):257–288, May 2000. ISSN 01637827. doi: 10.1016/S0163-7827(00)00005-9.

[200] Neal C. Robinson. Functional binding of cardiolipin to cytochromec oxidase. *Journal of Bioenergetics and Biomembranes*, 25(2):153–163, April 1993. ISSN 0145-479X, 1573-6881. doi: 10.1007/BF00762857.

[201] Mitchell Fry and David E. Green. Cardiolipin Requirement for Electron Transferin Complex I and IT1 of the Mitochondrial Respiratory Chain. *The Journal of Biological Chemistry*, 256(4):7, 1981.

[202] Mei Zhang, Eugenia Mileykovskaya, and William Dowhan. Gluing the Respiratory Chain Together: CARDIOLIPIN IS REQUIRED FOR SUPERCOMPLEX FORMATION IN THE INNER MITOCHONDRIAL MEMBRANE. *Journal of Biological Chemistry*, 277(46):43553–43556, November 2002. ISSN 0021-9258, 1083-351X. doi: 10.1074/jbc.C200551200.

[203] François Gonzalvez and Eyal Gottlieb. Cardiolipin: Setting the beat of apoptosis. *Apoptosis*, 12(5):877–885, May 2007. ISSN 1360-8185, 1573-675X.

doi: 10.1007/s10495-007-0718-8. URL `http://link.springer.com/10.1007/s10495-007-0718-8`.

[204] Darin B Ostrander, Genevieve C Sparagna, Andrew A Amoscato, Jeanie B McMillin, and William Dowhan. Decreased Cardiolipin Synthesis Corresponds with Cytochrome c Release in Palmitate-induced Cardiomyocyte Apoptosis. page 8, 2001.

[205] Raquel F. Epand, Malgorzata Tokarska-Schlattner, Uwe Schlattner, Theo Wallimann, and Richard M. Epand. Cardiolipin Clusters and Membrane Domain Formation Induced by Mitochondrial Proteins. *Journal of Molecular Biology*, 365(4):968–980, January 2007. ISSN 00222836. doi: 10.1016/j.jmb.2006.10.028.

[206] Erta Kalanxhi and Carmichael J. A. Wallace. Cytochrome c impaled: investigation of the extended lipid anchorage of a soluble protein to mitochondrial membrane models. *Biochemical Journal*, 407(2):179–187, October 2007. ISSN 0264-6021, 1470-8728. doi: 10.1042/BJ20070459.

[207] T. Heimburg and D. Marsh. Protein surface-distribution and protein-protein interactions in the binding of peripheral proteins to charged lipid membranes. *Biophysical Journal*, 68(2):536–546, February 1995. ISSN 00063495. doi: 10.1016/S0006-3495(95)80215-8.

[208] S-Y Choi, F Gonzalvez, G M Jenkins, C Slomianny, D Chretien, D Arnoult, P X Petit, and M A Frohman. Cardiolipin deficiency releases cytochrome c from the inner mitochondrial membrane and accelerates stimuli-elicited apoptosis. *Cell Death & Differentiation*, 14(3):597–606, March 2007. ISSN 1350-9047, 1476-5403. doi: 10.1038/sj.cdd.4402020.

[209] J. M. Berthiaume and K. B. Wallace. Adriamycin-induced oxidative mitochondrial cardiotoxicity. *Cell Biology and Toxicology*, 23(1):15–25, January 2007. ISSN 0742-2091, 1573-6822. doi: 10.1007/s10565-006-0140-y.

[210] Pattie S Green and Christiaan Leeuwenburgh. Mitochondrial dysfunction is an early indicator of doxorubicin-induced apoptosis. *Biochimica et Biophysica Acta (BBA) - Molecular Basis of Disease*, 1588(1):94–101, October 2002. ISSN 09254439. doi: 10.1016/S0925-4439(02)00144-8.

[211] W.P Tsang, Sophia P.Y Chau, S.K Kong, K.P Fung, and T.T Kwok. Reactive oxygen species mediate doxorubicin induced p53-independent apoptosis. *Life Sciences*, 73(16):2047–2058, September 2003. ISSN 00243205. doi: 10.1016/S0024-3205(03)00566-6.

[212] Guang-Wu Wang, Jon B Klein, and Y James Kang. Metallothionein Inhibits Doxorubicin-Induced Mitochondrial Cytochrome c Release and Caspase-3 Activation in Cardiomyocytes. *The Journal of Pharmacology and Experimental Therapeutics*, 298(2):8, 2001.

[213] Waldemar Priebe and Roman Perez-Soler. Design and tumor targeting of anthracyclines able to overcome multidrug resistance: A double-advantage approach. *Pharmacology & Therapeutics*, 60(2):215–234, January 1993. ISSN 01637258. doi: 10.1016/0163-7258(93)90007-Z.

Vita Auctoris

NAME: Brett W. Rickeard

PLACE OF BIRTH: Leamington, Ontario, Canada

YEAR OF BIRTH: 1996

EDUCATION: Bachelor of Forensic Science with Honours
University of Windsor
Windsor, ON, 2018